



UNIVERSITÀ
DEGLI STUDI
DI PADOVA



DIPARTIMENTO
DI INGEGNERIA
DELL'INFORMAZIONE

MASTER THESIS IN ICT FOR INTERNET AND MULTIMEDIA

X-ray Space Technology Transfer for Improved Mammography Screening

MASTER CANDIDATE

Francesco Nardo

Student ID 2022451

DATE

05 Sep. 2023

SUPERVISOR

Prof. Maria Elena Valcher

University of Padova

CO-SUPERVISOR

Prof. Desiree Della Monica Ferreira

Prof. Irfan Kuvvetli

Technical University of Denmark

ACADEMIC YEAR
2022 / 2023

To my four grandparents, parents, and to my brother Giovanni,
who have always supported me from far away.

To my supervisors and advisers, for their availability and kindness

To my dearest friends, Alex, Maciej, Sole, Nicola, Aldo, Pietro,
Giovanni, Sebastian, Giacomo, Gabriel, Alessia, Sara, Lorenzo.

To Emiliano, Alban and Paul, my lovely roommates.

To Paul and all my Ferroperm colleagues.

To the University of Padova for providing me with my education.

To the many people, professors and classmates I met in the past three years.

Abstract

Breast imaging using monochromatic X-rays promises lower doses and better image quality relative to conventional approaches.

Currently, the broad-energy spectrum emitted by an x-ray tube is degrading performance due to beam hardening, i.e., low energy X-rays are predominantly absorbed by the tissue, increasing dose, while high energy X-rays pass through the tissue unattenuated, decreasing image contrast.

It has been suggested that the use of coated mirrors capable of mono-chromatic x-ray hard spectra has the capability of reducing ionizing radiation exposure while also improving image quality during x-ray medical screening procedures. This research study is centered around screening for breast cancer using Digital Mammography (DM) techniques.

We present a simplified prototype system developed at DTU Space and implemented to validate proposed designs. The experimental setup consists of a source up to 40 keV, a high resolution roto-translation mechanical support and an advanced high resolution (55 micron), energy-sensitive Si detector with quantum efficiency (20% @22 keV).

For testing, phantom objects will be used as samples, allowing for a real-world realistic assessment of the use of space technology for breast screening. In this work, experimental measurements of absorbed dose reduction and contrast-to-noise ratio are reported.

Contents

List of Figures	xi
List of Tables	xvii
Glossary	xix
Acronyms	xxi
1 Introduction	1
1.1 Motivation	1
1.2 Simulations Tools	2
1.2.1 PIXet Pro	3
1.2.2 MATLAB	3
1.2.3 IDL	3
1.2.4 IMD	4
1.2.5 Gwyddion	4
1.2.6 SolidWorks	4
1.2.7 Kinesis	4
1.3 Involved Facilities	5
1.3.1 MultiLab	5
1.3.2 Finn Christensen X-ray Reflectometer	6
1.3.3 Detector Laboratory	7
1.3.4 Nanolab	8
1.3.5 Skylab	10
1.4 Thesis Overview	10
2 Methods, Techniques and Related Works	11
2.1 Digital Mammography	11

CONTENTS

2.1.1	Radiation Source	12
2.1.2	Compressed Breast	14
2.1.3	X-ray Detector	16
2.2	Coating Deposition Technique	20
2.2.1	Roughness and Diffuseness	20
2.2.2	Magnetron Sputtering Deposition	20
2.3	Characterization Techniques	22
2.3.1	Effective Dose	22
2.3.2	Mean Glandular Dose	23
2.3.3	Image Quality Metrics	24
2.3.4	X-ray Reflectivity	25
2.3.5	Atomic Force Microscopy	27
3	Optical Module Design	31
3.1	Space Telescopes Heritage	32
3.1.1	Variable Spacing and Variable Length	33
3.1.2	Coating Material Selection	35
3.1.3	Effective Area	37
3.1.4	Multi-layer Structures	37
3.2	Geometrical Parameters Optimization	39
3.2.1	Mirrors Length	39
3.2.2	Focal Length	39
3.2.3	Shells' Spacing	41
3.3	Coating Parameters Optimization	42
3.3.1	Thickness and Gamma	43
3.3.2	Number of Repetitions	45
3.4	Proposed Optical Module Design	46
4	Manufacturing and Assembly	51
4.1	Substrate Cleaning	51
4.1.1	Cleaning procedure	52
4.1.2	Scanning Probe Microscope	53
4.1.3	Levelling	54
4.1.4	Grain Mask	54
4.1.5	Statistical Analysis	56
4.2	Magnetron Sputtering Coating	57

4.2.1	Ring Speed Calibration	57
4.2.2	Coating Deposition	58
4.3	Coating Characterization	62
4.3.1	X-Ray Reflectivity Fitting Procedure	62
4.3.2	X-Ray Reflectivity Results	63
4.4	Sample Preparation	67
4.4.1	Phantom Bio-sample using Equine Tissue	68
4.4.2	Phantom Bio-sample using Swine Tissue	69
4.5	Assembly of the Experimental Setup	72
4.5.1	Mini-X2 X-ray Tube	74
4.5.2	Supports and Holders	76
5	Results and Discussions	79
5.1	Experimental Setup Calibration	79
5.1.1	Characterization of Beam Divergence	80
5.1.2	Mirror Alignment Procedure	81
5.1.3	Reflectivity Curve from Mirror	85
5.2	Monochromator Performances	87
5.2.1	Interpretation of Results	89
5.3	Mammograms	91
5.3.1	Projections	92
5.3.2	Regions of Interest	94
5.3.3	Poly-chromatic to Mono-chromatic Comparison	95
6	Conclusions	97
	References	101
	Acknowledgments	109
A	Appendix	111
A.1	Matlab	111
A.2	IDL	112

List of Figures

1.1	DTU Space Multilab.	6
1.2	DTU Space FCXR experimental setup, building 328. Work-bench for optical measurements and characterization. The setup measures the reflectivity of a coated sample and is operated via a remote computer. The monochromator is made of germanium instead of aluminium. Source [15].	7
1.3	Detector Laboratory at DTU Space.	8
1.4	AFM Icon-2 Positioned in the basement of Nanolab, building 346-904. Credits: DTU Nanolab internal.	9
2.1	X-ray tube geometry: cathode, electron beam, absorption and emission cone by rotating anode. Source [16]	12
2.2	The angular distribution of the x-ray intensity emitted by a $3\mu\text{m}$ thick Tungsten target for a combination of target angle between 12 and 35° . Source [17]	13
2.3	The emission x-ray spectra at 50, 80, and 100 kV constant potential. The photo peaks at 17.4 and 19.6 keV are due to the presence of molybdenum in the Tungsten target. All the three spectra are normalized to unit area. Source [18].	14
2.4	Commercially available Siemens MAMMOMAT. DM machine with needle to perform CEDM. Credit: Siemens.	16
2.5	Computed Quantum Efficiency (Q.E.) of a $500\mu\text{m}$ thick Silicon detector in the energy range 0-60 keV.	18
2.6	Surface/Interface width is the sum of contributes from roughness and diffuseness. Source [10].	21

LIST OF FIGURES

2.7 Magnetron sputtering diagram. (I) high vacuum minimizes contaminants, (II) ions are attracted to the target, (III) target atoms are bombarded, (IV) sputtered atoms travel towards the substrate, (V) sputtered atoms are deposited to substrate surface forming a thin film. Source: [29]. 21

2.8 A schematic diagram of the Differential Evolution algorithm over one generation. Source [10]. 27

2.9 Atomic Force Microscopy (AFM) PeakForce Tapping working principles. A) Tip approaching. B) Negative force due to molecular attraction. C) Max force. D) Negative force due to molecular adhesion. E) Tip disengaged. Credit: Bruker. 29

3.1 Schematic of Wolter type-I optic design. Source [42]. 32

3.2 Linear approximation of the Wolter type-I geometry with projected lengths and heights. Image adapted from [43]. 34

3.3 Comparison of various bi-layer material combinations. Each coating consists of 100 layers, specifically optimized for the grazing angle of its shell. 39

3.4 Breast MRI clinical bed-table can be tuned to host the Digital Mammography (DM) machine. The setup has (right to left): x-ray tube (orange), poli-chromatic and diverging light, optical module (red), monochromatic and collimated light (cyan), breast (white) and detector (purple). Image adapted from [50]. 40

3.5 Variable spacing between shells (outermost to innermost) and relative grazing angle. 41

3.6 Shell n.10, coated with 100 repeated W/Si bi-layers, optimization space of effective area in cm^2 at 22 keV. 43

3.7 Shell n.10, with 100 repeated W/Si bi-layers, effective area at 22 keV profile as function of thickness and gamma (black) with corresponding Gaussian fits (red) of the highest peak. 44

3.8 Total effective area as function of energy calculated for different repetition numbers. 45

3.9 Effective area at 22 keV (linear scale) as function of the repetition number. 46

3.10 The dimensions of the proposed Wolter Type-I design for the optical module. 47

3.11	Top-view of the parabolic (secondary) mirror projected area (yellow) onto the breast sample (pink) and detector plate (blue). . . .	48
4.1	The cleaning setup inside DTU Multilab. Three separate bathtubs: hot soap water, deionized water and ethanol.	53
4.2	The cleaned substrate, surrounded by anti-static dust-free paper, dimensions: 70 mm x 10 mm x 0.78 mm.	53
4.3	Atomic Force Microscopy (AFM) 500x500nm to determine substrate roughness prior to coating.	55
4.4	Atomic Force Microscopy (AFM) 500x500 nm ² to determine substrate roughness prior to coating. Region of interest marked using the segmentation algorithm.	55
4.5	Ring rate calibration according to hyperbolic law compared with linear law. The dotted lines represent the 95% prediction error bounds.	58
4.6	Starting position for the coating run. Pre-sputtering of Silicon active. The mounting points for the three samples and the magnetrons are visible as well as 30° lines.	59
4.7	Pressure logbook for the Magnetron sputtering run.	60
4.8	Logbook for the Magnetron sputtering run.	61
4.9	X-ray Reflectivity (XRR) data fitting from Interactive Data Language (IDL)/IMD using three different models and comparison with the theoretical model from the design phase.	64
4.10	The simulated reflectivity of mirrors (ds03 /-07 /-09 /-11) at 22 KeV is shown with the first Bragg peak angle marked, and it is compared to the simulation from the design (engineering) phase.	66
4.11	The CIRS Model 015 Mammographic Accreditation Phantom. Source [53].	67
4.12	Equine bio-lumps provided by the 3D-imaging center, DTU Physics.	68
4.13	Bio-sample: Swine belly with sodium chloride grains.	70
4.14	Bio-sample composition: swine fat, muscle and NaCl grains to be tested for Linear Absorption Coefficient (LAC) determination.	70
4.15	The setup consists in: (i) X-ray source, (ii) two slits, (iii) a multi-layer mirror mounted on a rotational stage, (iv) the sample and (v) the detector are mounted on a moving cart rail.	73

LIST OF FIGURES

4.16	Amptek Mini-X2 X-ray tube and a table containing its specifications. Source: [58].	75
4.17	Emission spectrum from the Amptek Mini-X2 X-ray tube.	75
4.18	Tailor-made and 3D-printed Computer-aided Design (CAD) models designed in SolidWorks.	77
5.1	Beam footprint on the probe detector positioned at 465 mm from the exit of the second slit, beam incidence normal to detector surface.	80
5.2	Graphical representation of the beam reflected by the mirror. The beam footprint on the mirror is shifted because of mis-alignment, and beam divergence is present. The grazing angle is 0.516°	82
5.3	Graphical representation of the alignment process whereas half of the beam is stopped by the Mirror.	82
5.4	The setup calibration curves for mirror alignment.	84
5.5	Precise calibration of mirror <i>ds0307</i> via comparison of the experimental X-ray Reflectivity (XRR) measurements with the theoretical one from Figure 4.10	86
5.6	Comparison between 10 seconds exposure of direct and monochromated beam spectra with Full Width at Half Maximum (FWHM) of the last shown.	87
5.7	Predicted spectrum of the monochromatic beam in the integration time is 40.1 second over-plotted the measured spectra.	88
5.8	Comparison between direct beam spectra to show proportionality between integration time and photon counts.	89
5.9	10 second exposure radiograms of the beam with the detector moving in different positions along the Y-axis.	90
5.10	Comparison of the acquired radiogram mosaicking the 10 seconds projections of the bio-sample.	91
5.11	Projection from the 10 seconds direct beam imaging of the bio-sample.	93
5.12	Mosaic of all the projections from Figure 5.11. Left: raw absorption radiogram of 10 second direct beam exposure. Right: related absorption spectra without quantum efficiency applied.	93
5.13	Region of interest on the acquired radiogram mosaicking for data analysis.	94

5.14 Comparison in terms of Contrast to Noise Ratio (CNR), Signal to Noise Ratio (SNR), effective dose, Mean Glandular Dose (MGD) and Figure of Merit (FOM) between two different radiograms. With a 10 second exposure of poly-chromatic (direct) or mono-chromatic (reflected) x-ray beams. 95

List of Tables

1.1	Main Features of DTU Space Multilab	6
2.1	Results of the Compressed Breast Size Study. Source [19].	14
2.2	Optimal (higher SNR with lower radiation dose) x-ray energy as function of the breast dimensions. Source [20].	15
2.3	Recommended radiation weighting factors. Adapted from [32].	23
2.4	Comparison between the three AFM modes available for topography studies. PeakForce Tapping was selected. Credit: Bruker.	28
3.1	Properties of different metals at 22 keV.	36
3.2	Optical properties of different low density materials at 22 keV.	38
3.3	Independent and Optimization parameters for the coating recipe.	42
3.4	Optimal radius (spacing), calculated grazing angle, calculated projected area, optimal thickness, gamma, calculated reflectivity, and calculated effective areas (at 22 keV) per each shell in the optical module with a Wolter Type-I geometry where each shell is coated with 50 specific W/Si bi-layers.	49
4.1	Statistical roughness from AFM data analysis.	56
4.2	Properties of the selected shell mirrors' and required ring speed ω for their coatings.	59
4.3	The XRR parameters for the theoretical model, together with the one fitted via the simple, intermediate and complex models. Thickness and roughness are in Angstrom, gamma is adimensional.	65
4.4	Tabulated Linear Absorption Coefficient (LAC) cm^{-1} values of studied bio-sample compared to actual breast tissue properties at 20 keV. Adapted from [55].	71

Glossary

FCXR DTU Space Finn Christensen X-ray Reflectometer Laboratory, located in Building 328. xi, 6, 7, 72

mammogram A mammogram, or radiogram, often referred to as projection image, is an X-ray image of a particular sample, i.e. a breast. If multiple projections are acquired while the sample rotates, it is possible to reconstruct the sample via Digital Breast Tomosynthesis.. 1, 3, 15, 19, 22, 79, 91–94, 96

Multilab DTU Space Multi Layer Coating Laboratory, located in Building 328. xi, xiii, xvii, 5, 6, 36, 53

Nanolab DTU Nanolab is the National Centre (Denmark) for Nano Fabrication and Characterization, located in Building 347. xi, 8, 9

XCOM National Institute of Standards and Technology (NIST) X-Ray and Gamma-Ray Attenuation Coefficients and Cross Sections Database . This web program is used to calculate photon cross sections for scattering, photoelectric absorption and pair production, as well as total attenuation coefficients, in any element, compound or mixture, at energies from 1 keV to 100 GeV.. 18, 71

Acronyms

AFM Atomic Force Microscopy. xi–xiii, xvii, 4, 9, 27–29, 53–56, 66, 98

CAD Computer-aided Design. xiv, 4, 77

CAT Computer Aided Tomography. 1

CNR Contrast to Noise Ratio. xv, 3, 15, 25, 69, 79, 94–96, 99

DBT Digital Breast Tomosynthesis. 1, 16, 19

DC Direct Current. 5, 74

DM Digital Mammography. xii, 1, 2, 10, 11, 15, 32, 40, 41, 75, 97

FFC Flat Field Correction. 19, 91, 92, 99

FOM Figure of Merit. xv, 25, 26, 63, 95, 96, 99

FWHM Full Width at Half Maximum. xiv, 10, 66, 79, 80, 87, 88, 99

ICRP International Commission on Radiological Protection. 22, 23

IDL Interactive Data Language. xiii, 3, 26, 37, 43, 45, 64, 112

LAC Linear Absorption Coefficient. xiii, xvii, 69–71, 99

MGD Mean Glandular Dose. xv, 23–25, 79, 95, 96, 99

MRI Magnetic Resonance Imaging. 1, 2, 40

NIST National Institute of Standards and Technology. xix, 18, 67

Acronyms

PET-G Polyethylene Terephthalate Glycol. 10

PLA Polylactic Acid. 10, 86

Q.E. Quantum Efficiency. xi, 17, 18, 93

RMS Root Mean Square. 56

ROI Region of Interest. 24, 25, 94

SDD Silicon Drift Detector. 75

SI International System of Units. 22

SNR Signal to Noise Ratio. xv, 25, 79, 94–96, 99

SPM Scanning Probe Microscopy. 4, 52, 54

SPO Single Pore Optic. 35

USB Universal Serial Bus. 74

XRR X-ray Reflectivity. xiii, xiv, xvii, 4, 6, 7, 25, 26, 57, 61–66, 85, 86, 98

1

Introduction

1.1 MOTIVATION

Besides skin cancer, breast cancer is the most common cancer in women in the world [1]. Unfortunately, it has a much higher mortality rate and an estimated 685,000 women died from breast cancer in 2020 worldwide, corresponding to 16% or 1 in every 6 cancer deaths in women [2]. Thankfully, breast cancer is also the most commonly diagnosed cancer type (more than lung cancer), accounting for 1 in 8 cancer diagnoses (both sex). In 2020, there were about 2.3 million new cases of breast cancer globally.

Different studies, [3] have demonstrated the importance of an early detection and sub-types identification of breast cancer in order to effectively initiate a treatment (chemotherapy, surgery etc.).

Nowadays, two techniques are mainly used in breast screening: Digital Mammography (DM), also known as mammograms, and Magnetic Resonance Imaging (MRI). The former is the process of using high energy X-rays (usually 30 keV but up to 50 keV) absorption contrast to capture a digital image. Mammography may be 2D or 3D, in which case is called Digital Breast Tomosynthesis (DBT), and it is based on the collection of multiple projection and the use of the Computer Aided Tomography (CAT) reconstruction method [4]. The latter is based on dedicated magnetic coils and radio-waves to image the breasts. Unlike mammograms, breast MRI requires a contrast dye injected into the tissue prior to the

1.2. SIMULATIONS TOOLS

exam [5].

Although both of these techniques are currently used to identify breast cancer, there are some distinct advantages, and disadvantages in both. In particular, the spatial resolution of an image from breast MRI is 10 to 100 times better than a simple mammogram. Conversely, a mammogram exam is more affordable (cost-wise), reliable (less false-positive) and available (DM machines are now the de-facto standard for breast screening with multiple manufacturers worldwide).

However, due to risk associated to radiation dose in human tissues, guidelines [6], such as the one approved by the NCCN¹ Breast Cancer Screening and Diagnosis Panel, specifies a recommended time interval between medical exams. The recommended frequency of these exams depends on factors such as the patient's age and genetic predisposition. Typically, this interval falls within the range of every 1-3 years. However, in more than one specific category, screening frequencies of every few (6) months are required.

Therefore, **the purpose of this thesis is to investigate the possibility of reducing ionizing radiation exposure while also improving image quality during x-ray medical screening procedures.** In order to do so, space technology such as the one involved in the Athena X-ray telescope [7] can be transferred into the design of an optical component for mammogram machines.

1.2 SIMULATIONS TOOLS

This paragraph presents an overview of various software programs, libraries, coding languages, and simulation tools, emphasizing their functionalities and contributions to the research. These tools were employed to analyze data, conduct complex calculations, simulate scenarios, and process data throughout the study.

For a detailed understanding of each program, code, or algorithm used to optimize, simulate, and visualize the results presented in this report, please refer to Appendix A. In the appendix, the functionality and implementation details of each tool will be thoroughly explained.

¹National Comprehensive Cancer Network.

1.2.1 PIXET PRO

PIXet PRO, developed by Advacam, is a software tool specifically designed for advanced image analysis and processing in the field of X-ray imaging [8].

The software offers seamless integration with Advacam's X-ray detectors and imaging systems, allowing for direct acquisition and real-time processing of X-ray projection images. PIXet PRO provides advanced analysis capabilities, including image feature extraction and spectra imaging. These two features are particularly useful to generate quantitative data to be further analysed in MATLAB.

1.2.2 MATLAB

MATrix LABoratory (MATLAB) is a high-level programming language and development environment. Developed by MathWorks, MATLAB provides an integrated development environment (IDE) and a rich toolbox for numerical computation, algorithm development and data visualization.

MATLAB will be the primary tool utilized for data analysis, particularly for calculating key metrics such as the Contrast to Noise Ratio (CNR) and dosimetry from the collected X-ray mammograms. Additionally, MATLAB will be employed to generate plots and visualize data obtained from other software, ensuring consistency and uniformity in the report.

1.2.3 IDL

Interactive Data Language (IDL) is a programming language specifically designed for data analysis and visualization. Developed by Research Systems Inc. (now Harris Geospatial Solutions), IDL has been widely adopted in various scientific fields, including astronomy, geology, climate research, and remote sensing [9].

It has a command-line interface, where commands and expressions can be executed or evaluated in real-time. However, via scripting, it is possible to implement more complex programs and routines. In particular, it also integrates with other popular programming libraries, such as IMD. This interoperability makes it easy to take advantage of specialized algorithms for optimization of the coating. The simulations from IMD, which are part of the optimization process, are processed using IDL. In particular version 8.7.3 of the software was licensed.

1.2. SIMULATIONS TOOLS

1.2.4 IMD

IMD² is a computer program for modelling optical properties (reflectance, transmittance, absorptance, phase shifts and electric-field intensities) of multi-layer films, i.e., films consisting of any number of layers of any thickness [10].

In particular, in this report, IMD will be used to model both single-layer or multiple bi-layer coating profiles and to perform data fitting of X-ray Reflectivity (XRR) measurements.

1.2.5 GWYDDION

Gwyddion is a modular program for Scanning Probe Microscopy (SPM) data visualization and analysis. Primarily it is intended for the analysis of height fields obtained by scanning probe microscopy techniques (such as AFM) [11]. Regarding data processing, it provides instrument tilt or non-planarity compensation and basic statistical functions and quantities (roughness parameters) that will be used in the report.

1.2.6 SOLIDWORKS

SolidWorks is a Computer-aided Design (CAD) software widely used in various industries for 3D modeling, simulation, and product design. In addition to its modeling capabilities, SolidWorks offers simulation and analysis tools. Users can apply various physical properties and constraints to their models, perform stress analysis, motion simulation, and fluid dynamics analysis, among others [12].

Developed by Dassault Systèmes, SolidWorks offers a comprehensive suite of tools to model and create custom and tailor-made components for the experimental setup, visualize their Assembly and visualize the prototype functionalities before 3D printing.

1.2.7 KINESIS

Kinesis is a software platform developed by Thorlabs, a leading manufacturer of precision scientific instruments and photonics products. It is designed specif-

²IMD user manual is available at: <http://www.rxollc.com/idl/>.

ically for controlling and operating Thorlabs' range of motion control systems. With Kinesis, multiple motorized stages, actuators, and other motion devices can be controlled within a complex experimental setup. This enables precise positioning and alignment of components, ensuring accuracy during setup calibration. Furthermore, Python can be used to develop automation scripts and custom user interfaces tailored to specific experimental requirements [13].

Kinesis was used to control the rotation and the two translation stages of the experimental setup. Both continuous and relative coordinated motion, with specific velocity and acceleration profiles, have been used in custom sequences, to perform alignment, calibration and experimental measurements. Step precision and jog freedom were also controlled to ensure position errors below 0.1%.

1.3 INVOLVED FACILITIES

Considering the scale of the project and the manufacturing and assembly challenges involved in creating a prototype, several laboratories were involved throughout the project's development. This paragraph provides a summary of the diverse facilities that were utilized or collaborated with.

1.3.1 MULTILAB

DTU Space Multilab, abbreviation of: Multi Layer Coating Laboratory, is a coating facility located at DTU Space (Building 328) and it contains a custom built Direct Current (DC) magnetron sputtering chamber, Figure 1.1. This is a flagship facility for research and development as well as production of flight-ready thin film coatings for space applications. The current system includes four magnetrons (Onix-1520IDC), produced by Angstrom sciences³, installed inside the chamber. However, for the coating runs conducted in this project, only two of the magnetrons were utilized. Technical features are summarized in Table 1.1.

³Website: <https://www.angstromsciences.com/sputtering-magnetron>.

1.3. INVOLVED FACILITIES



Figure 1.1: DTU Space Multilab.

Available magnetron ports	4
Mirror plate coverage area	0.79 m ²
Drum radius	0.475 m
Target-Sample distance range	60-250 m
Sputtering direction from centre	Outwards
Target Material area	194 cm ²
In-situ plasma treatment	No
Maximum single substrate area (L×W)	500 × 300 mm ²

Table 1.1: Main Features of DTU Space Multilab

1.3.2 FINN CHRISTENSEN X-RAY REFLECTOMETER

X-ray Reflectivity (XRR) characterization can be used to qualify deposited coatings, yielding information about film thickness, roughness, film morphology, density, etc. Single-energy reflectometers are compact and easy to operate, making them ideal for immediate and follow-up characterization of manufactured x-ray mirrors [14].

In particular, the Finn Christensen X-ray Reflectometer (FCXR) facility, performs XRR measurements at 8.048 keV. At higher energies, the characterization of films composed of multi-layer coatings or single layer coatings of high atomic number

(high-Z) materials offers valuable insights. However, assessing the quality of a low atomic number (low-Z) overcoat on a dense film becomes progressively challenging due to the reduced reflectance of low-Z materials and the dominant signal from the high-density layer beneath.

The XRR reflectometer spans a length of 2059 mm, extending from the X-ray generator to the detector, as shown in Figure 1.2. X-rays are generated using a copper rotating anode, which emits a continuous Bremsstrahlung spectrum. To select the desired wavelength, a monochromator composed of two asymmetrically cut germanium crystals is employed, specifically designed to transmit Cu k-alpha radiation at 8.048 keV. Photon detection and spectra acquisition is achieved using an energy-sensitive detector, or a similar device. Before reaching the sample (mirror), the X-ray beam can be tailored into various dimensions by adjustable slits, ranging from $0.1 \times 0.1 \text{ mm}^2$ to $5 \times 5 \text{ mm}^2$. The setup is capable of accommodating samples with dimensions of up to 200 mm in length and 300 mm in height [15].

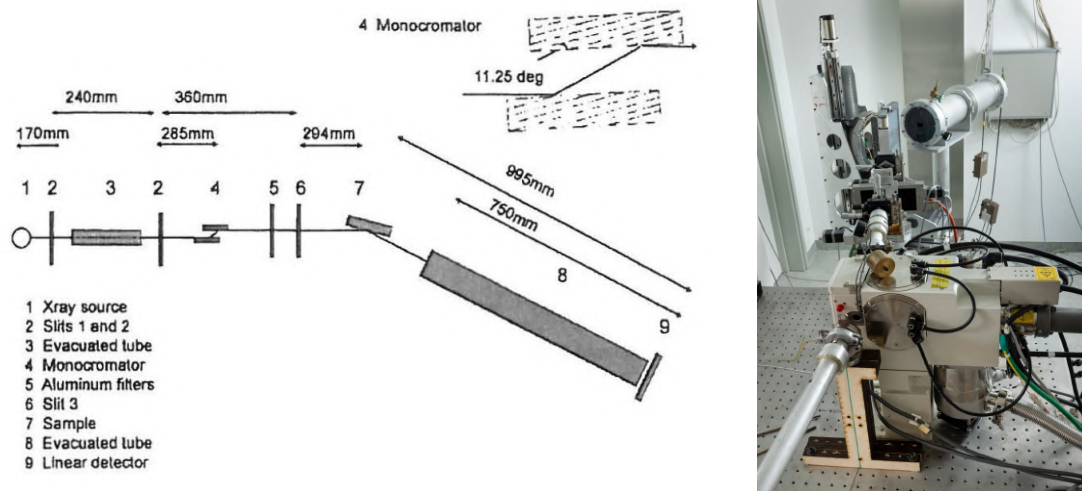


Figure 1.2: DTU Space FCXR experimental setup, building 328. Work-bench for optical measurements and characterization. The setup measures the reflectivity of a coated sample and is operated via a remote computer. The monochromator is made of germanium instead of aluminium. Source [15].

1.3.3 DETECTOR LABORATORY

The detector group at DTU Space operates a well-equipped laboratory facility dedicated to detectors. The laboratory is maintained as a cleanroom environment with a cleanliness level of Class 100,000 (ISO 8), Figure 1.3. The facility

1.3. INVOLVED FACILITIES



Figure 1.3: Detector Laboratory at DTU Space.

offers a diverse range of radiation sources spanning from a few keV to MeV. Additionally, it is equipped with state-of-the-art signal processing and data acquisition systems. Motorized XYZ tables are also available for precise characterization and testing of detectors and readout electronics.

Within this cleanroom environment, the construction of the prototype and the experimental setup for conducting radiology on bio-samples has been completed. The successful implementation was facilitated by the presence of optical tables and the availability of motorized stages, which played crucial roles in assembling the necessary equipment and achieving precise movements and positioning. Furthermore, the laboratory is equipped with specialized tools to measure, shield, and safely operate within an environment that involves ionizing radiation.

1.3.4 NANOLAB

DTU Nanolab serves as the National Centre for Nano Fabrication and Characterization in Denmark. It operates and maintains a wide range of advanced processing equipment within a 1350 m² cleanroom facility, certified under ISO-9001 and classified as class 10-100. This cleanroom provides a controlled environment essential for precision fabrication and characterization processes. However, in addition to the cleanroom facilities, DTU Nanolab also houses an ad-

vanced characterization unit located in the basement of the building. This unit grants users access to various scanning electron microscopes, dual-beam microscopes, transmission electron microscopes, and Atomic Force Microscopy (AFM) instruments.

For AFM measurements, DTU Nanolab possesses two Bruker AFM Dimension Icon-Pt instruments⁴ as the one shown in Figure 1.4.



Figure 1.4: AFM Icon-2 Positioned in the basement of Nanolab, building 346-904. Credits: DTU Nanolab internal.

AFM is a scanning probe microscope that utilizes a sharp probe to scan surfaces in tapping mode. This scanning process generates topographic plots of the surface with a lateral resolution of approximately 1 nm and a vertical resolution of less than 1 Å, making it highly suitable for angstrom-scale roughness measurements of the mirrors that are part of the prototype optical module. Although the AFM characterization is not performed within a cleanroom environment, precautionary measures are taken. The samples are blown with a nitrogen gun and handled with gloves to minimize contamination risks.

⁴Full specs available at <https://www.bruker.com/en/products-and-solutions/microscopes/materials-afm/dimension-icon-afm.html>.

1.4. THESIS OVERVIEW

1.3.5 SKYLAB

DTU Skylab 3D Printing Workshop is a collaborative space dedicated to 3D printing techniques. It offers a range of cutting-edge 3D printers, including filament-based printers, resin-based printers, and even advanced multi-material and metal 3D printers. In particular, for this project, both the Prusa i3mk3 and the UltiMaker S3 Extended 3D printers were utilized. The majority of the (structural) components manufactured for this work were 3D printed using Polylactic Acid (PLA) or Polyethylene Terephthalate Glycol (PET-G) filaments.

1.4 THESIS OVERVIEW

This chapter provided an overview of the study's purpose, simulation tools, and research facility involved.

In the upcoming Chapter 2, we will delve into the working principles of a conventional Digital Mammography (DM) setup. Additionally, we will explore related works focusing on reducing radiation dose and improving image quality through mono-chromating radiation. Theoretical explanations of production and characterization techniques used in this report will also be presented.

Moving on to Chapter 3, we will discuss the design process of the optical module. Utilizing space technology transfer, the optical module is adapted from past and current telescope designs, considering both geometrical relations and coating recipes. A summary table, or prototype guide of the engineered design will be provided at the end of this section.

Chapter 4 will cover the manufacturing of the prototype optical module and the assembly of an experimental setup for x-ray imaging validation. Technical challenges encountered during this process will be described, and data-analysis will be interwoven throughout the chapter to clarify certain design choices.

In Chapter 5, we will evaluate the optical module's performance, particularly in terms of reflectivity and Full Width at Half Maximum (FWHM). We will also compare and analyze poly- and mono-chromatic mammograms. The setup alignment and calibration process will be discussed in detail.

Finally, in Chapter 6, we will summarize the main achievements and results of this work.

2

Methods, Techniques and Related Works

This chapter contains a summary of the relevant work conducted in the field of monochromatic radiation for mammography applications. It encompasses a comprehensive overview of experimental techniques, theoretical knowledge, and research findings that will be utilized throughout the report.

2.1 DIGITAL MAMMOGRAPHY

Before investigating possible solutions or techniques to reduce ionizing radiation exposure during mammograms screenings, it is essential to briefly explain how a conventional Digital Mammography machine works. Its main components are:

- **Source:** an X-ray tube generates x-ray radiation
- **Sample:** a compression paddle is used to flatten and spread the breast tissue, ensuring uniformity during image acquisition
- **Optical module:** it is not part of a conventional DM machine, it has function of monochromator and collimator.
- **Image Detector:** in DM it is typically a digital flat-panel detector or a charge-coupled device sensor while previously it used to be photographic x-ray plates.

The optical module, which is not typically found in conventional DM machines, plays a significant role in this study. The primary objective of this report is to

2.1. DIGITAL MAMMOGRAPHY

engineer the optical module, investigate its optimization parameters, and characterize its performance. Usually, the mono-chromator, or more precisely the band-pass functionality, is performed by K-edge absorption filters such as aluminium filters.

Moreover, a compression plate is traditionally included to allow both large and small breasts to be imaged in various exposures, including horizontal exposures. The breast is centered on the subject table between the table and the plate to reduce involuntary motion artifacts. However, in our experimental setup, a phantom sample is utilized instead of a human breast. Therefore, the inclusion of a compression plate is not necessary.

2.1.1 RADIATION SOURCE

The X-ray tube consists of an electron beam impinging onto an anode (usually Tungsten) which is both rotating and water cooled to resist the thermal load [16]. The electrons are accelerated from the cathode under a voltage potential and the radiation is emitted from the anode after electrons have travelled the depth of x-ray production (x) as depicted in Figure 2.1. The inclination of the anode in respect to the optical axis is called target angle (θ) and is usually between 12-35°.

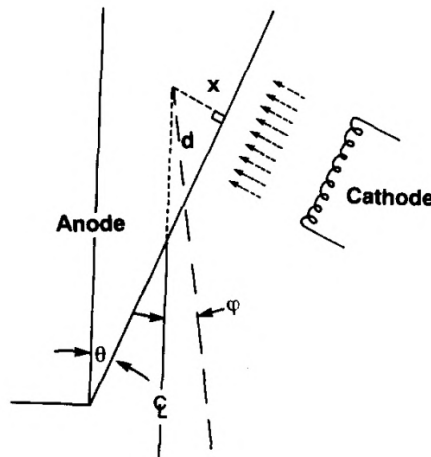


Figure 2.1: X-ray tube geometry: cathode, electron beam, absorption and emission cone by rotating anode. Source [16]

After emission, the x-ray photons travel a path of length d through the target and photon absorption generates a phenomenon called heel-effect [17], i.e. the

flux is not uniform in all the directions but it depends on the emission angle as represented in Figure 2.2. To mitigate such effect, a lead shield with a fixed aperture (window) is placed on the optical (emission) axis in order to block the most external (less bright) part of the photon beam.

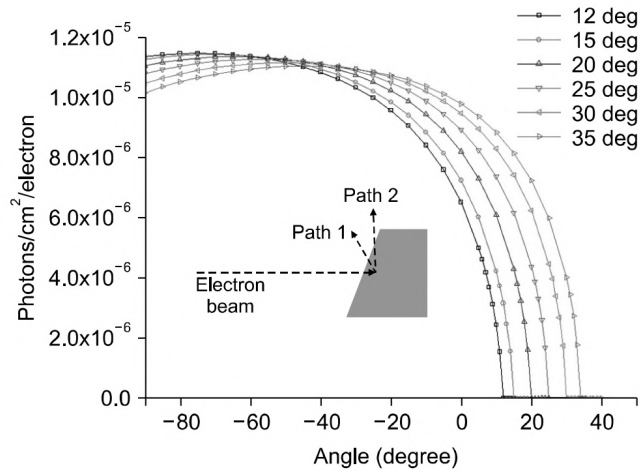


Figure 2.2: The angular distribution of the x-ray intensity emitted by a $3\mu\text{m}$ thick Tungsten target for a combination of target angle between 12 and 35° . Source [17]

Two different emission mechanisms contribute to the overall emission spectra: the Bremsstrahlung and the photoelectric effect [18]. The first has a continuous spectrum shape and consists in a radiation emitted due to the deceleration (braking) of the electrons during collision. The second emits spectral lines corresponding to the allowed absorption/emission energies between atomic conduction bands.

Specifically, the x-ray tube used in the experimental setup is the Mini-X2 tube manufactured by Amptek which will be presented in Paragraph 4.5.1.

Figure 2.3 illustrates an example of the emitted spectrum. Since the electrons are accelerated in a 50 kV potential, the maximum energy of emitted photons can reach 50 keV.

2.1. DIGITAL MAMMOGRAPHY

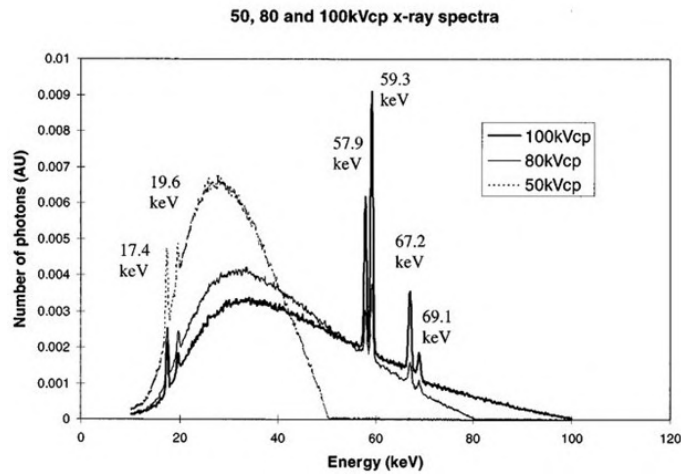


Figure 2.3: The emission x-ray spectra at 50, 80, and 100 kV constant potential. The photo peaks at 17.4 and 19.6 keV are due to the presence of molybdenum in the Tungsten target. All the three spectra are normalized to unit area. Source [18].

2.1.2 COMPRESSED BREAST

According to a survey [19] on the English female population collected by the NHS¹, the average breast dimensions and proportions, under the pressure of the compression plate, are reported in Table 2.1.

	Age (years)	Thickness (cm)	Width (cm)	Breadth (cm)
Mean	48.5	5.2	18	8.1
Standard deviation	9.1	1.1	2.4	2.1
Maximum value	82	8.6	25	17.4
Minimum value	31	2.5	12	1.4

Table 2.1: Results of the Compressed Breast Size Study. Source [19].

A number of authors [20], have calculated, using signal-to-noise criteria, the optimal x-ray energies for mammography to minimize radiation dose. These calculations are based on the use of K-edge filters of various materials (palladium, rhodium, germanium, molybdenum, aluminium etc.) and thicknesses. Using only these filters, the optimum energy lies above the characteristic lines of molybdenum except for thin breasts, Table 2.2.

¹National Health Service.

Optimum energy (keV)	16	19	21	23
Energy band (keV)	14–18	17–21	19–23	21–25
Breast thickness (cm)	2	4	6	8

Table 2.2: Optimal (higher SNR with lower radiation dose) x-ray energy as function of the breast dimensions. Source [20].

Soft X-rays (below 5 keV) cause more damage than hard X-rays due to the high absorption cross sections of C, N and O K-shells, the main organic matter constituents. It is well recognized that the extent of the radiation damage depends on different factors, such as X-ray wavelength, exposure dose, sample preparation and environment [21]. Consequently, photon energies below 5 keV make little contribution to the image because of their poor tissue penetration. In other words, the absorption contrast (difference in the absorption coefficients of different cells) and consequently the image quality do not benefit from soft X-rays which conversely radiation dose is very harmful to human tissues.

Traditionally, all the commercially available mammograms machine are operated using k-edge absorption of chosen alloy-filters [22] to filter out radiation below 15keV and above 40keV, however, what if we were able to engineer an ideal monochromatic filter?

Studies involving the optimization of the energy for monochromatic DM have suggested that the optimal energy to maximize the Contrast to Noise Ratio (CNR) while minimizing the radiological risks, quantified by the dose, is comprehended in the range 22-35 keV with a peak at 28 keV [23].

DM machine providers such as Siemens² have already started working on prototypes, Figure 2.4, implementing titanium filters [24].

Additionally, as we will present in Paragraph 4.5.1, the maximum brilliance for a Silver x-ray tube operated with a 40 kV potential is found to be at 22 keV!

To conclude, the scope of this research is to design a 22 keV monochromator. For such energy, we achieved the highest flux from the source, and the best image quality (CNR) for the lowest dose of effective radiation. This concept is not orig-

²Siemens Healthineers AG is a German medical device company. More about the MAMMOMAT system at: <https://www.siemens-healthineers.com/en-us/mammography/biopsy-systems/breast-biopsy>.

2.1. DIGITAL MAMMOGRAPHY



Figure 2.4: Commercially available Siemens MAMMOMAT. DM machine with needle to perform CEDM. Credit: Siemens.

inal, and related works include a proposal to use a multi-layer coated scanning mirror as a mono-chromator [25, 26].

2.1.3 X-RAY DETECTOR

Given the average breast size in Table 2.1, current mammograms machines have a detector plate of large dimensions, i.e. 24×30cm with a pixel resolution of 85 μm [22]. Usually the adopted detector is based on an amorphous selenium (a-Se) layer for direct conversion from x-rays to electron-hole pairs. The detector is not energy sensitive.

In addition to the requirements for digital mammography, detectors for Digital Breast Tomosynthesis (DBT) need to achieve additional capabilities. These include faster reading time (the x-ray exposures actually cover 46° in 20s), to keep the total acquisition time of all projections to a minimum, with minimal ghosting and lag, which has been shown to introduce image artifacts, and minimal reduction in detective quantum efficiency.

The optical module will be discussed in detail in the following sections, its main roles are two: to collimate the diverging beam (angular divergence ϕ between $12\text{-}16^\circ$) from Figure 2.1 and to monochromate the spectrum from Figure 2.3.

In particular, as stated before, collimation is important because of the magnification effect of the diverging beam on the detector plate, thus lowering the image resolution. In the same way, mono-chromating improves the absorption contrast (i.e. image quality) while reducing unnecessary exposure to ionizing radiation.

QUANTUM EFFICIENCY

Every detector operates with a given Quantum Efficiency (Q.E.). The fundamental mechanism for imaging is the absorption of photons passing through the plate medium, which follows an exponential law, the Beer's law:

$$I(x) = I_0 e^{-\mu x} \quad (2.1)$$

Where I_0 is the incident photon flux in $\text{cm}^{-2}\text{s}^{-1}$. $I(x)$ is the flux at depth x (in cm) in the absorber. μ is the linear attenuation coefficient in cm^{-1} . The Q.E. of the material in a given detector plate is simply the fraction of absorbed photons as a function of the energy i.e.

$$qe(E) = 1 - e^{-\mu(E) \cdot x} = e^{-\sigma(E) \cdot \rho \cdot x} \quad (2.2)$$

Whereas μ , the absorption coefficient, is the product between the cross section σ (cm^2/g) and the material density ($\rho = 2.32 \text{ g/cm}^3$ for Silicon), while x is the maximum distance travelled in the detector. The detector involved in this research has a thickness of $500\mu\text{m}$, Paragraph 4.5.

The linear attenuation coefficient depends on the energy of the photons together with the material properties of propagation medium. It is a sum of contributions from individual interaction processes:

1. **Photoelectric absorption:** interaction between a photon and an absorber atom. The photon completely disappears, and, in its place, an energetic photoelectron is ejected by the atom from one of its bound shells.
2. **Scattering:** interaction between incident gamma-ray photon and an electron in the absorbing material. The energy is divided between the two, dependently on the scattering angle. It can either be coherent (Rayleigh) or incoherent (Compton).
3. **Pair production:** incidence gamma-ray photon completely disappears and in its place an electron positron pair is created. Minimum gamma-ray energy of 1.022 MeV is required.

In Equation (2.1), the cross section is the probability of the interactions between photons and matter. Therefore, there are four possible interactions (Rayleigh and Compton are both scattering possibilities):

$$\sigma(E) = \sigma_{pa}(E) + \sigma_{coh}(E) + \sigma_{inc}(E) + \sigma_{pp}(E)$$

2.1. DIGITAL MAMMOGRAPHY

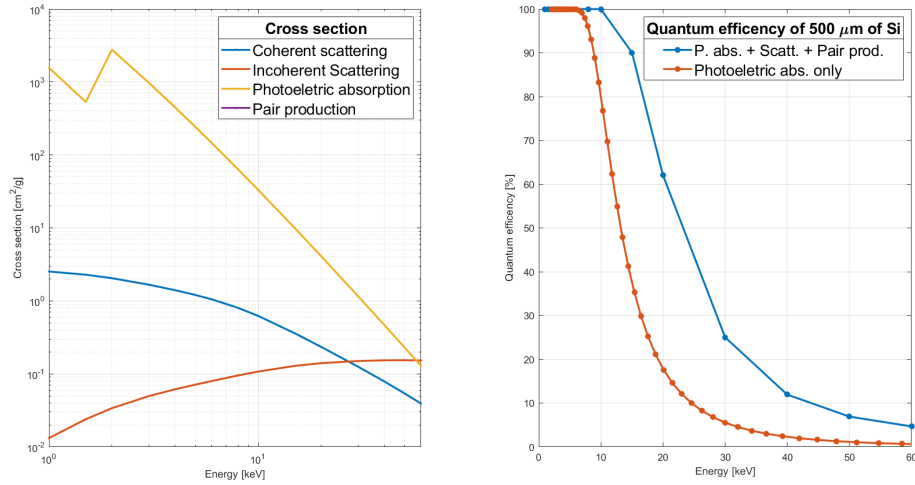


Figure 2.5: Computed Quantum Efficiency (Q.E.) of a 500 μm thick Silicon detector in the energy range 0-60 keV.

The National Institute of Standards and Technology (NIST) provides XCOM, i.e. a X and Gamma-Ray Attenuation Coefficients and Cross Sections Database [27] for all the periodic table elements plus the most common compounds.

In Figure 2.5, we report the quantum efficiency as function of the incoming photon energy. Note that the pair production contribution is null, since the impinging photons are below the 1.022 MeV required threshold.

For absorption dose calculation, the recorded photons count (I_{det}) must be corrected for efficiency loss (Q.E.) due to transmission of high energy photons through the detector substrate. Given the Q.E. from Equation (2.2) and represented in Figure 2.5, the true photon intensity (I^*) is:

$$I^*(E) = \frac{I_{det}(E)}{qe(E)}$$

Indeed, it is crucial to note that in the detector, the signal (counts) generated is solely due to photoelectric absorption. Other scattering events, such as Compton scattering or Rayleigh scattering, do not contribute to the signal measured by the detector and are not taken into account when estimating the quantum efficiency. Consequently, when computing the Q.E. to find the original intensity of the incident X-rays, only the cross-section contribution from photoelectric absorption is considered, Figure 2.5.

CONVENTIONAL FLAT FIELD CORRECTION

In X-ray imaging, the acquired projection images generally suffer from fixed-pattern noise, which is one of the limiting factors of image quality [28].

Projection images without a bio-sample are acquired with and without the X-ray beam turned on, which are referred to as flat fields and dark fields. It is common practice to normalize the acquired projection data with averaged flat fields taken prior to the scan. The flat fields include the non-uniform sensitivity of the detector pixels, as well as the in-homogeneities of the incident X-ray beam.

Usually, source instabilities, in particular from synchrotron X-ray tomography, introduce time-depending fluctuations in flat fields. Luckily, given the stability of the x-ray tube source and the averaging over a large integration time, the flat field is assumed to be stationary.

The correction used for this purpose is referred to as Flat Field Correction (FFC). To execute this technique, the following images are required:

- **Dark field:** the dark field D , often referred to as the offset field, is an image which is captured by the detector without X-ray illumination. The signal detected in the absence of X-rays from the X-ray source includes both the true dark current (which is proportional to the exposure time), and the digitization offset, which is independent of exposure time. Usually, the exposure time for the acquisition of dark field images is equal to that of the projection images.
- **Flat field:** the flat field F , often referred to as the background, is acquired with X-ray illumination, but without the presence of the sample. It is used to measure and correct for in-homogeneities in the X-ray beam intensity profile and detector response.
- **Projection image:** the projection image M often referred to as mammo-gram, is acquired with X-ray illumination and the sample is positioned in the field of view of the detector. If multiple images M_i are acquired while the sample rotates, usually in regular angular intervals, it is possible to reconstruct the sample via Digital Breast Tomosynthesis (DBT).

Therefore, based on the acquired flat and dark fields, before processing, the measured projection images with bio-sample are normalized as:

$$N_i = \frac{M_i - D}{F_i - D} \quad (2.3)$$

2.2 COATING DEPOSITION TECHNIQUE

In the field of coating, various deposition techniques are employed, including Physical Vapor Deposition (PVD) and Chemical Vapor Deposition (CVD). However, in this work, our primary focus is on magnetron sputtering. In physics, sputtering is a phenomenon in which microscopic particles of a solid material are ejected from its surface, after the material is itself bombarded by energetic particles of a plasma or gas. It is the process involved for the coating deposition.

2.2.1 ROUGHNESS AND DIFFUSENESS

Prior to coating a substrate, it is important to comprehend the properties of its surface. In the context of specular optical functions, like x-ray reflection, the impacts of face roughness and face diffuseness are indistinguishable. Roughness causes light to scatter into non-specular directions, while diffuseness enhances the transmittance of the interface. Nonetheless, both types of imperfections ultimately lead to a reduction in the reflectance of the surface/interface. Consequently, we can introduce a parameter known as the interface width (σ) to characterize these imperfections:

$$\sigma = \sqrt{\sigma_r + \sigma_d} \quad (2.4)$$

Where σ_r represent the surface roughness, i.e. the spatial variability in structure, and σ_d the interface diffuseness, i.e. the spatial variability in homogeneity.

Figure 2.6 provides a visual representation of the physical difference between these two parameters. At the center, the interface profile function ($p(z)$) is plotted. This function can be interpreted as a direct description of the refractive index that each of the two materials possesses. Thus, it describes the transition between the optical constants of medium 1 and medium 2 at the interface.

2.2.2 MAGNETRON SPUTTERING DEPOSITION

In the laboratory, after mounting the samples on a holder, the latter is inserted into a vacuum chamber [29]. Once vacuum is achieved by means of multi-stage turbo-pumps, Argon gas is introduced in the chamber. Thanks to an extremely strong electrical field, Argon is ionized and forms a peculiar purple-glowing

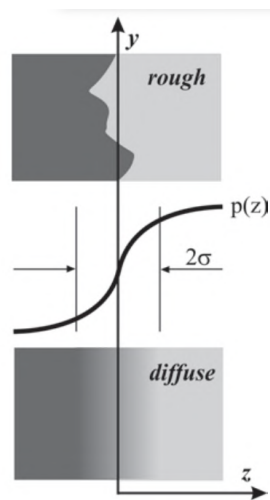


Figure 2.6: Surface/Interface width is the sum of contributes from roughness and diffuseness. Source [10].

plasma cloud on top of the target material. The Argon ions act as projectiles on the target, jolting atoms which are then deposited on the substrate, Figure 2.7.

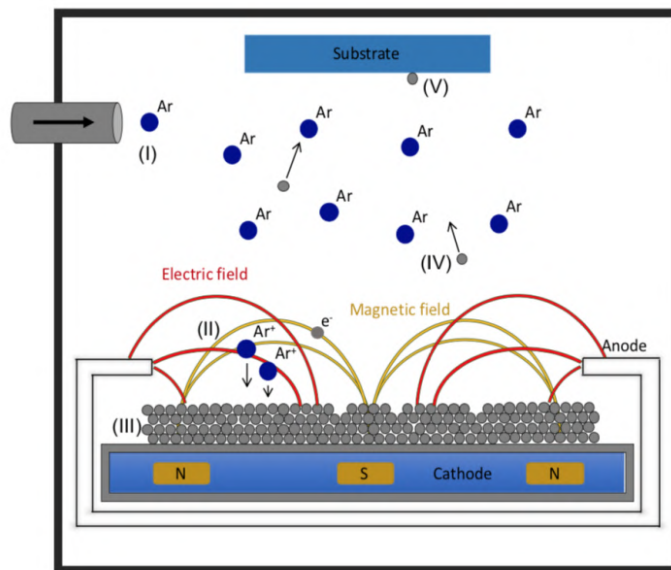


Figure 2.7: Magnetron sputtering diagram. (I) high vacuum minimizes contaminants, (II) ions are attracted to the target, (III) target atoms are bombarded, (IV) sputtered atoms travel towards the substrate, (V) sputtered atoms are deposited to substrate surface forming a thin film. Source: [29].

Currently, the thinner coating resolution achievable using Gold, via the magnetron sputtering technique, is 10\AA with 2.5\AA standard deviation (roughness), i.e. Gold approximate atomic radius size [30, 31].

2.3 CHARACTERIZATION TECHNIQUES

When comparing separate mammograms collected under different conditions, with varying exposures and different machines, several metrics can be utilized to assess radiation dose and image quality.

2.3.1 EFFECTIVE DOSE

The Absorbed dose, D is the fundamental dose quantity given by

$$D = \frac{dE}{dm} = \frac{\int_T D(x, y, z) \rho(x, y, z) dV}{\int_T \rho(x, y, z) dV} [\text{Gy}] \quad (2.5)$$

Where dE is the mean energy imparted to matter of mass dm (infinitesimal) by ionising radiation. The International System of Units (SI) unit for absorbed dose is joule per kilogram (J/kg) and its special name is Gray (Gy) according to the International Commission on Radiological Protection (ICRP) [32].

The absorbed dose is derived from the mean value of the stochastic quantity of energy imparted (E) and does not directly reflect the random fluctuations of the interaction events in tissue. In situations where tissues or organs have non-homogeneous compositions, the absorbed dose can be more precisely defined as the integration over all tissue types (T) whereas absorbed dose D and density ρ are function of location (x, y, z) within the volume V .

While the right hand side of Equation (2.5) is defined at any point in matter, its value is still obtained as an average over a mass element dm . In particular, the process of averaging the absorbed dose is performed over the mass of a specific tissue, organ, or anatomical part, such as muscle, liver, or breast. The accuracy of this mean dose value in representing the absorbed dose across all regions of the anatomical part relies on the homogeneity of the radiation exposure.

The ICRP guidelines provide two weighting factors to enable the calculation of effective radiation from the absorbed one:

1. The radiation weighting factor, denoted by w_R , is specific to the type of radiation being considered. For example, for X-rays (photons), the radiation weighting factor is given in Table 2.3. This factor is used in calculating the

equivalent dose (H_T), which can be applied to the entire body or individual organs.

2. The tissue weighting factor, denoted by w_T , is specific to the type of tissue or organ being irradiated. This factor is combined with the radiation weighting factor (w_R) to calculate the effective dose (H_E) for non-homogeneous tissues exposed to an uniform radiation. Specifically, according to the latest ICRP release [32], w_T has a factor 0.12 for breasts.

Radiation type	Radiation weighting factor, w_R
Photons	1
Electrons and muons	1
Protons and charged pions	2
Alpha particles, fission fragments, heavy ions	20
Neutrons	A continuous function of neutron energy

Table 2.3: Recommended radiation weighting factors. Adapted from [32].

Starting from the absorbed dose which is expressed in Gray, the effective dose can be calculated as:

$$H_E[Sv] = \sum_T w_T \cdot \sum_R w_R \cdot D[Gr] \quad (2.6)$$

Both the radiation and tissue weighting factors are dimensionless. However, for historical reasons, equivalent and effective dose are expressed in Sievert (Sv) instead of Gray to explicit that biological effects have been taken into account. The sum in Equation (2.6) encompasses all types of radiations (R) and tissues (T).

2.3.2 MEAN GLANDULAR DOSE

The effective dose experimentally measures the absorbed radiation by the phantom bio-sample, however it may not fully represent the characteristics of a real breast.

In the context of mammography applications, an alternative simulation approach to the effective dose is recommended, known as the Mean Glandular Dose (MGD). The MGD serves as the primary descriptor of absorbed dose in the breast and it is derived from the emitted spectrum through conversion factors established with Monte-Carlo simulations. Various authors have proposed different conversion factors, taking into consideration factors such as breast thickness, glandularity, x-ray spectra, and beam quality [33].

2.3. CHARACTERIZATION TECHNIQUES

Since the estimation of conversion factors involves Monte-Carlo simulations, MGD represents the dosimetry in a breast model rather than in an actual breast tissue. As a result, the estimation of absorbed radiation is susceptible to errors, irrespective of the used method.

For the monochromatic mammography performed in this work, the MGD was determined using mono-energetic normalized glandular dose coefficients $DgN(E)$, with E representing the x-ray energy in keV, as tabulated by Boone et al. [34]. The calculation takes into account the x-ray tube spectrum and involves summing over all energy bins as shown in Equation (2.7):

$$MGD[mGy] = \sum_E K(E)[mGy] \cdot 0.114[R/mGy] \cdot DgN(E)[mGy/R] \quad (2.7)$$

The formula for the MGD was adapted from [34] to be used with air-kerma K [35] instead of the older unit exposure (conversion factor from Rontgen to milli-Gray). The $DgN(E)$ values were selected according to a compressed breast thickness of 5 cm (the average from Table 2.1), and assuming a 50/50 percent distribution of glandular and adipose tissues. The air-kerma K per energy bin E can be calculated for known photon flux Φ from the x-ray spectrum at the sample position:

$$K(E)[mGy] = E \cdot \Phi(E) \cdot (\mu_{en}/\rho)_{air}(E)$$

Here, $(\mu_{en}/\rho)_{air}(E)$ denotes the mass energy attenuation coefficient of air, tabulated in [36]. The photon flux per energy bin $\Phi(E)$ was calculated using the setup detectors, taking into account the x-ray spectrum, the quantum efficiency and the dimensions of the Silicon plate.

2.3.3 IMAGE QUALITY METRICS

From each radiogram, two Region of Interest (ROI) are of importance in these comparisons: the imaging target (e.g., cancer formation or signal, denoted by s) and the background (denoted by b).

To quantify image noise, the standard deviation of the pixel values within each Region of Interest (ROI) is calculated:

$$\sigma = \text{noise} = \sqrt{\sigma_s^2 + \sigma_b^2}$$

Using the means (μ) of the pixel values within one ROI, different metrics can be employed to assess image quality as described in related works [25, 26]:

Signal to Noise Ratio (SNR): the mean value of the signal divided by the whole image noise

$$SNR = \frac{\text{Signal}}{\text{Noise}} = \frac{\mu_s}{\sigma} \quad (2.8)$$

Contrast to Noise Ratio (CNR): the mean value of the signal subtracted the mean value of background divided by the whole image noise

$$CNR = \frac{\text{Contrast}}{\text{Noise}} = \frac{\mu_s - \mu_b}{\sqrt{\sigma_s^2 + \sigma_b^2}} \quad (2.9)$$

Additionally, according to [26], a Figure of Merit (FOM) function is computed as the ratio of the image quality, expressed through CNR, to the Mean Glandular Dose (*MGD*):

$$FOM = \frac{CNR}{MGD} \quad (2.10)$$

2.3.4 X-RAY REFLECTIVITY

X-ray Reflectivity (XRR) is a non-destructive technique used to investigate the surface and interface structures of thin films and multi-layered materials. It involves shining a beam of X-rays onto a sample at a specific angle of incidence (grazing angle) and measuring the intensity of the reflected X-rays as a function of the scattering angle. By analyzing the variations in the intensity of the reflected X-rays, XRR provides valuable insights into the thickness, density, roughness, and material properties of interfaces between top, intermediate and substrate layers.

As a result of having prior knowledge about the material composition of the coating, this technique has been employed in this study to address an inverse problem. Its purpose is to determine the actual thickness and roughness of the deposited layers via data fitting. The reflectance curve from the coated samples have been measured by means of a collimated monochromatic x-ray beam ($E = 8.048\text{keV}$, i.e. copper alpha line) as a function of different grazing angles between 0 and 4 degrees with a precision of 10 mdeg.

To ensure the safety of human tissues and eyes from the potentially harmful

2.3. CHARACTERIZATION TECHNIQUES

effects of X-rays, the actual measurements are conducted using a remote computer. The process begins with the calibration of the sample's position within the laboratory reference system. Subsequently, an automated script is employed to rotate both the sample and the detector (twice the rotation angle) while recording the number of incident photons at different grazing angles. Reflectivity is then determined by calculating the ratio between the recorded photon count and the maximum number of photons, obtained without the presence of a sample (i.e., accounting for stray light on the detector).

Given the reflectivity curves from an XRR experiment, the inverse problem can be resolved with a genetic evolution algorithm for data-fitting. This is an algorithm that combines Monte-Carlo simulations with a Figure of Merit (FOM) in order to fit the parameters of a given model to specific data.

The evolution usually starts from a population of randomly generated individuals, and is an iterative process, with the population in each iteration called a generation. In each generation, the Figure of Merit of every individual in the population is evaluated; the FOM is usually the value of the objective function in the optimization problem being solved.

The more fit individuals are stochastically selected from the current population, and each individual's value is slightly modified (recombined and possibly randomly mutated, i.e. Monte-Carlo methods) to form a new generation. The new generation contains the best candidates of the previous solutions and is then used in the next iteration of the algorithm.

This process continues until the convergence criteria (perceptual variation of FOM lower than threshold) or maximum number of allowed generation is met.

Genetic algorithms are generally less sensitive to initial parameter values and less likely to get locked at local minima than gradient expansion algorithms. In IMD, the differential evolution algorithm is described by Björck [37]; and it is a somewhat more complicated genetic algorithm (Figure 2.8), with two sets of populations for each generation: the parent population A and the trial population B.

To compare different models the reduced χ^2 statistic is used. In particular, the Levenberg-Marquardt gradient-expansion algorithm computes its value using instrumental weighting; IMD uses the *MPFIT* program written in IDL by

C. Markwardt [38] which is based on *MINPACK-1.22* [39].

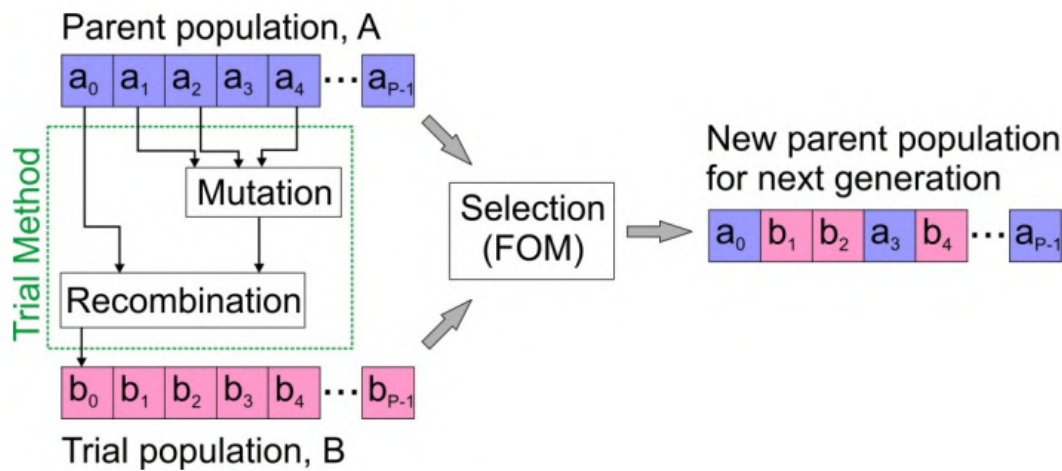


Figure 2.8: A schematic diagram of the Differential Evolution algorithm over one generation. Source [10].

2.3.5 ATOMIC FORCE MICROSCOPY

Atomic Force Microscopy (AFM) is an imaging technique used to investigate the surface topography and physical properties of a wide range of materials at the nano-scale resolution. AFM utilizes a sharp tip to image the surface of a sample. The key components of an AFM system include the probe, scanner, controller, and control software. The AFM probe consists of three parts: the tip, the cantilever, and the substrate. The cantilever typically has a triangular shape and is responsible for the movement of the tip. In AFM, an optical lever is used to generate a feedback signal based on the angular deflection of the cantilever.

The Icon-2 from Bruker offers three operational modes: Contact, Tapping, and PeakForce Tapping. For this study, the PeakForce Tapping mode was utilized, which is a variation of the tapping mode. Further details about the other two modes can be found in the user manual³ but a brief comparison is reported in Table 2.4.

³The manual is not freely available but access to it can be requested to Bruker <https://www.bruker.com/en/products-and-solutions/microscopes/materials-afm/dimension-icon-afm.html> or to Nanolab <https://labmanager.dtu.dk/d4Show.php?id=3590&mach=438>.

2.3. CHARACTERIZATION TECHNIQUES

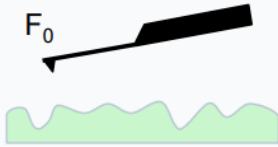
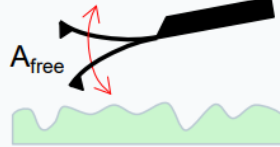

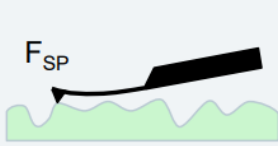
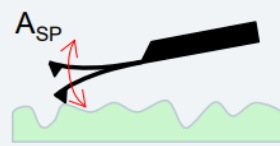

	Contact Mode	Tapping Mode	PeakForce Tapping
First introduced	1986 (original mode)	1992	2009
Tip-sample interaction	Tip scans in constant contact with the sample	Cantilever is oscillated at its resonance, so the tip intermittently contacts or "taps" the sample	Whole probe is ramped sinusoidally, so the tip intermittently contacts or "taps" the sample
Tip oscillation	Not applicable	At cantilever resonance (typ. 10-1000's kHz) with typ. amplitude of 1-10's nm	Below cantilever resonance (typ. <10 kHz) with typical amplitude of 10-100's nm
Imaging feedback	Constant force (cantilever deflection)	Constant tapping amplitude	Constant peak force
Sketch			
Off surface			
On surface			

Table 2.4: Comparison between the three AFM modes available for topography studies. PeakForce Tapping was selected. Credit: Bruker.

In PeakForce Tapping, the tip performs rapid force curves at each pixel in the image. The peak interaction force from these curves is used as the feedback signal for imaging. PeakForce Tapping typically operates at 2 kHz and it is not dependent on the resonance frequency of the cantilever. The working principle of this mode, whose signal is based on the force curve registered by the system is reported in Figure 2.9.

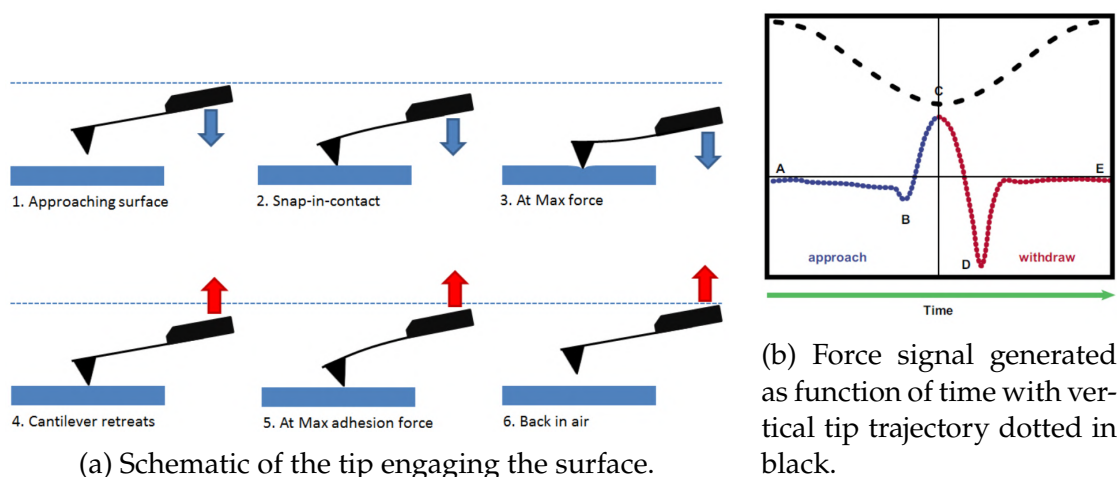


Figure 2.9: AFM PeakForce Tapping working principles. A) Tip approaching. B) Negative force due to molecular attraction. C) Max force. D) Negative force due to molecular adhesion. E) Tip disengaged. Credit: Bruker.

Specifically, PeakForce Tapping has three distinctive advantages over other modes:

1. Direct control of the tip-sample force at low values, that allows for precise control of the tip-sample force, making it possible to achieve very small peak forces (gentle operation and higher resolution). Moreover, the tip only briefly touches the surface during each tapping cycle, minimizing shear forces.
 2. Direct measurement of the force-distance interactions, enabling quantitative nano-mechanical measurements such as elasticity or stickiness in particular by providing force-distance curve at each pixel.
 3. Operation below the resonance frequency of the cantilever, offering simplicity and consistency in particular for imaging in liquid environments
- However, the scan speed is limited by the frequency of PeakForce Tapping, although it is similar to the regular Tapping Mode.

In this study, a new Tap150Al cantilever tip was employed, offering a remarkable vertical resolution of up to 1 angstrom. The expected total coating thickness is at a maximum 0.5 μm . Considering also margins for any potential tilting or non-leveling of the sample, the minimum tip height and maximum structure height is 15 μm , which is compatible with the sample to be examined.

3

Optical Module Design

In this chapter, we present the design of an optical module intended to be included in a conventional mammography setup with the purpose of monochromate and collimate the incoming X-ray beam. The study focuses on two main optimization processes: one concerning the optical geometry of the module and the other related to the coating material and multi-layer design.

Regarding the optical geometry, we investigate various parameters such as the inner and outer radius, focal length, number of concentric rings, height between rings (fixed or variable), length and width of primary and secondary mirrors (fixed or variable), and their shapes. The goal is to explore the optimization space of these parameters and determine the configuration that provides the largest projected area.

On the other hand, the coating optimization process involves determining the best coating recipe to improve the reflectivity of the mirrors. While a simple recipe could consist of a single layer of Iridium on top of a Silicon substrate [40], more complex recipes are introduced in this report. For instance, we consider a multi-layer coating made of Tungsten (W) and Silicon (Si), which has been previously studied by researchers in [30].

Ultimately, the success of this chapter lies in achieving the optimization of the effective area, a parameter which takes into account both the projected area and the reflectivity.

3.1 SPACE TELESCOPES HERITAGE

In 1952, Hans Wolter proposed three different designs for x-ray telescopes that utilize only two (primary and secondary) mirrors [41]. These designs are known as Wolter optics of type I, II, and III. In this report, we have adopted the Wolter type I design.

In the literature, Wolter type I optics are commonly utilized in x-ray space telescopes, employing grazing incidence mirrors that reflect x-rays at very shallow angles. Since the incidence angle is $\approx 90^\circ$, it is more convenient to introduce the grazing angle, i.e. the angle between the incoming ray and the reflection surface (instead of the plane normal), which is usually in the order of few milli-radians (mrad).

Wolter type I optics are preferred in many applications due to their excellent performance and versatility in design. They offer the advantage of having the shorter dimension compared to Wolter type II or type III configurations [42]. This compact design is particularly advantageous for applications in DM machines, where a reduced optical module size can benefit the overall machine encumbrance.

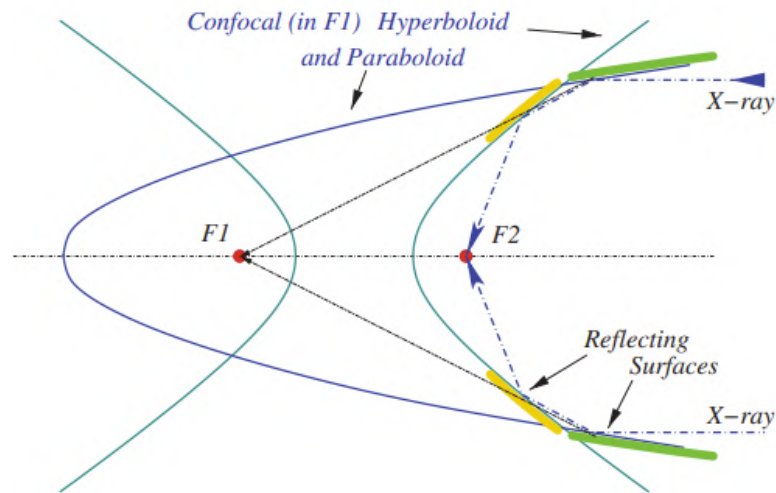


Figure 3.1: Schematic of Wolter type-I optic design. Source [42].

The basic configuration of this design is illustrated in Figure 3.1. A paraboloid and a con-focal and coaxial hyperboloid are respectively the primary and secondary mirrors. X-rays strike the paraboloid with grazing angle (α) and are af-

terwards reflected and strike the hyperbola (with again angle α). The resulting focusing beam forms the image, at the front of the hyperboloid (point F1 in the Figure).

Incidentally, the Wolter-I configuration is often simplified thanks to the conical approximation. Instead of parabolic or hyperbolic, the mirrors are conicals. This simplified design is important because it eases the fabrication of the mirrors and the performance is similar to the original Wolter-I design. Moreover, by nesting several con-focal mirrors, the collecting area of incoming photons can be increased. This concept is an absolute necessity in our case, in an effort to maximize the optical module effective area.

For instance, since the objective of the optical module is to collimate, rather than focusing, the photons in our setup will propagate backwards, i.e. the hyperbolic is the primary mirror and the parabolic the secondary. To do so, the x-ray source must be positioned at the focal point. Anyhow, moving onwards, we will treat the geometry configuration as in a conventional space telescope.

3.1.1 VARIABLE SPACING AND VARIABLE LENGTH

In this section, we will derive the geometric and trigonometric relationships between the design parameters of the Wolter type I optical module. To simplify the problem, we can approximate the hyperbolic and parabolic curvatures using a polynomial or linear interpolation. By doing so, we can reduce the complex geometry represented in Figure 3.1 to a more straightforward configuration shown in Figure 3.2. This simplified configuration will be used in the analysis.

First of all, the relationship between focal length (Z_0), ring (or shell) mean radius (r) and grazing angle (α) is (trigonometry):

$$\tan(4\alpha) = \frac{r}{Z_0} \quad (3.1)$$

As we will discuss later, having a longer mirror in the Wolter geometry provides advantages in terms of aperture, which translates into a larger photon collection area. Therefore, longer mirrors are preferred for better performance. However, it is important to note that there are limitations in the sputtering machine employed at DTU Space (Presented in Sec. 1.3.1), which restricts the maximum allowed length of a curved plate that needs to be coated to 16 cm.

3.1. SPACE TELESCOPES HERITAGE

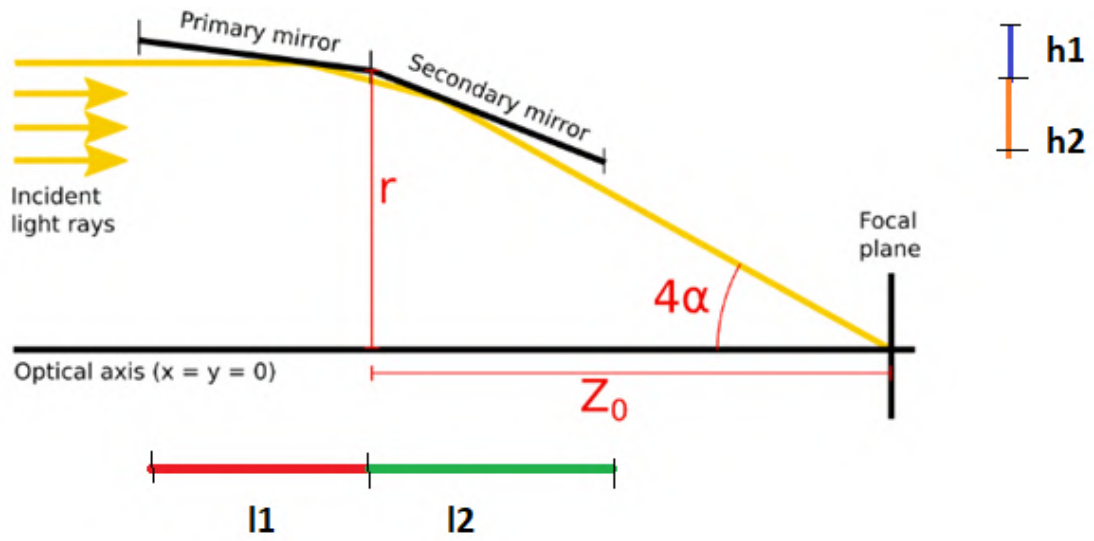


Figure 3.2: Linear approximation of the Wolter type-I geometry with projected lengths and heights. Image adapted from [43].

Regarding the mirror lengths shown in Figure 3.2, we observe that from a trigonometric perspective, they act as the hypotenuses (HP_i) of two triangles with bases l_i and heights h_i , and are of equal length:

$$HP = HP_1 = HP_2 = 16\text{cm} \quad (3.2)$$

The subscript number indicates whether it refers to the primary or secondary mirror. We define the letters l and h as the projected dimensions of the mirrors, on the optical axis and on the detector axis, respectively:

$$\begin{aligned} l_1 &= HP \cdot \cos(\alpha) \\ l_2 &= HP \cdot \cos(3\alpha) \\ h_1 &= HP \cdot \sin(\alpha) \\ h_2 &= HP \cdot \sin(3\alpha) \end{aligned}$$

When considering nesting, since each shell has a different grazing angle, according to formula (3.1), the length of the mirror, i.e., the hypotenuse, remains constant for each shell, while the cathetus (base and height) may vary.

On the optical axis, the total projected dimension (length) occupied by the optical module is:

$$L_{tot} = l_1 + l_2$$

And since it depends on the grazing angle α , the longitudinal length of each shell is variable.

Considering nesting, the space between shells must be as small as possible to improve the projected area. Similar designs for Single Pore Optic (SPO) [44] require a fixed 1 mm thick structure to support the weight of the mirrors themselves.

Additionally, we must consider that mirrors of different rings should not touch each other to avoid shadowing or blocking part of the collected photons. Therefore, a variable space h_1 (height of primary mirror) must be added. The spacing between rings is therefore variable:

$$h = h_1 + 0.1 \text{ cm}$$

Finally, the projected area, which represents the geometrical area capable of interacting (and possibly reflecting) photons, can be calculated as follows:

$$A_p = \pi \cdot ((r + h_1)^2 - (r)^2) \quad (3.3)$$

In conclusion, both the spacing and the horizontal length of the shells in the optical module are variable, thus providing some challenges during assembly and structure design. However, the mirrors lengths are constant, thus making them easier to manufacture.

3.1.2 COATING MATERIAL SELECTION

By carefully designing the optical geometry, including the size and spacing of the mirrors, the focal length, and the grazing angles, we can maximize the projected area of the mirrors, which directly influences the number of photons that can be collected and focused. At the same time, the choice of coating materials and design is essential to enhance the reflectivity of the mirrors, enabling them to efficiently reflect and focus the incident x-rays.

Each material has different optical properties that can be summarized in the refractive index, which to be precise, is a function of the energy. Considering photons at 22 keV the refractive index is a complex number:

$$n = 1 - \delta + i\beta$$

3.1. SPACE TELESCOPES HERITAGE

Where the real part represents the velocity ratio between vacuum and light speed in the medium and the imaginary part represents absorption.

Rather than blindly exploring the performance of various single-layer or multi-layer combinations of materials, we can draw from existing research conducted for space telescopes. In particular, the missions ROSAT [45], XMM Newton [46], Suzaku [47] and eRosita [48], utilise a single layer of Gold coating on top of a Nickel substrate. A newer proposal, such as XRISM [49], proposes Aluminium single layers. However, multi-layer coatings, consisting of two alternating materials of different thicknesses (one high density and one low density), provide higher reflectivity, particularly for higher energies (>10 keV). NuSTAR [30] implements a combination of platinum (Pt) and Silicon Carbide (SiC), later substituted by amorphous Carbon (C). In future mission proposal such as Athena [40], the researchers have implemented a bi-layer coating made of Iridium (Ir) and Boron carbide (B₄C). Additionally, different mirror shells within the optical module may use various recipes, such as in NuSTAR [30], where the outer ones are based on Tungsten (W) as the high density layer.

Based on availability in DTU Multilab and existing heritage, we will focus exclusively on three metals: Nickel Vanadium, Tungsten, and Platinum, as dense materials for the coating. The critical angle, which determines the total reflection condition, depends on the real part of the refractive index. The formula for the critical angle can be derived from Snell’s Law, and it involves the Thomson radius r_0 , the interacting photon wavelength λ and the electron density of the chosen material ρ_e :

$$\alpha_{crit} = \sqrt{2\delta} = \sqrt{2 \frac{r_0 \lambda^2 \rho_e}{2\pi}}$$

By using public databases like CXRO¹, Table 3.1 can be compiled with the relevant critical angle values.

Material	93% Nickel 7% Vanadium (Ni.93V.07)	Tungsten (W)	Platinum (Pt)
Refractive index	1-3.6735E-06 + i9.3416E-08	1- 6.6392E-06 + i4.1465E-07	1 - 7.3092E-06 + i5.6015E-07
Critical Angle [deg]	0.1553	0.209	0.219
Cost per gram [\$]	3	0.01	24

Table 3.1: Properties of different metals at 22 keV.

¹The Center for X-Ray Optics is a multi-disciplined research group within Lawrence Berkeley National Laboratory’s Materials Sciences Division. The database is accessible at: https://henke.lbl.gov/optical_constants/pert_form.html.

3.1.3 EFFECTIVE AREA

Interestingly, the coating recipe can be tailored differently for each shell to maximize the effective area of each mirror. In the Wolter-I structure, where each photon undergoes two reflections, the collecting area depends on the square of the reflectivity (R). Consequently, the effective area (A_{eff}^i) of the i -th ring is defined as:

$$A_{eff}^i(E) = A_p^i(\alpha) \cdot R(E, \alpha)^2$$

Here, A_p^i represents the projected area of the i -th ring as a function of the grazing angle α , and $R(E, \alpha)$ is the reflectivity as a function of energy and grazing angle.

Moving further, the final design will have 58 concentric rings (n), as it will be presented in Paragraph 3.2, so the total effective area (A_{eff}^{tot}), as a function of photon energy, is the sum of the effective area contributions from each ring:

$$A_{eff}^{tot}(E) = \sum_{i=1}^n A_{eff}^i(E) \quad (3.4)$$

Since the primary purpose of the optical module is to monochromate the x-ray beam, it is more relevant to evaluate the effective area at the monochromatic energy of 22 keV. This is achieved by computing the total effective area at that specific energy:

$$A_{eff}(22keV) = \sum_{i=1}^n A_{eff}^i(22keV) \quad (3.5)$$

3.1.4 MULTI-LAYER STRUCTURES

Based on previous studies [45]-[49], the initial coating design may involve a simple single-layer of coating deposited onto the substrate. However, such a coating is designed to work in total reflection condition, with grazing angles below the critical angle, which is not suitable for the monochromatic nature of our optical module.

As an alternative, we directly consider a bi-layer coating, which can be modeled in IMD/IDL. This type of coating consists of alternating layers of high density and low density materials with different thicknesses. The introduction of this structure, according to the Bragg law, offers the advantage of improving

3.1. SPACE TELESCOPES HERITAGE

reflectivity for specific wavelengths due to constructive interference. Additionally, multi-layers composed of identical repeating bi-layers further enhance the mono-chromating capability.

On the other hand, a multi-layer design with layer thickness following a linear, geometric, or exponential law would not be useful for a monochromator, as it would increase reflectance outside the desired peak.

The low density materials considered for testing in this report are Silicon (Si) and Carbon (C). These materials are commonly used in well-known space telescope designs [7], [40], and [30]. Their optical properties at 22 keV are summarized in Table 3.2.

Material	Silicon (Si)	Carbon (C)
Refractive index	1 - 1.000E-06+i3.115E-09	1-9.430E-07+i1.464E-10
Critical Angle [deg]	0.081	0.079

Table 3.2: Optical properties of different low density materials at 22 keV.

Inside each bi-layer, the proportions between different materials thicknesses are: $d_1 = \Gamma \cdot d$ and $d_2 = (1 - \Gamma) \cdot d$, where d is the total thickness of that bi-layer and gamma the bi-layer ratio:

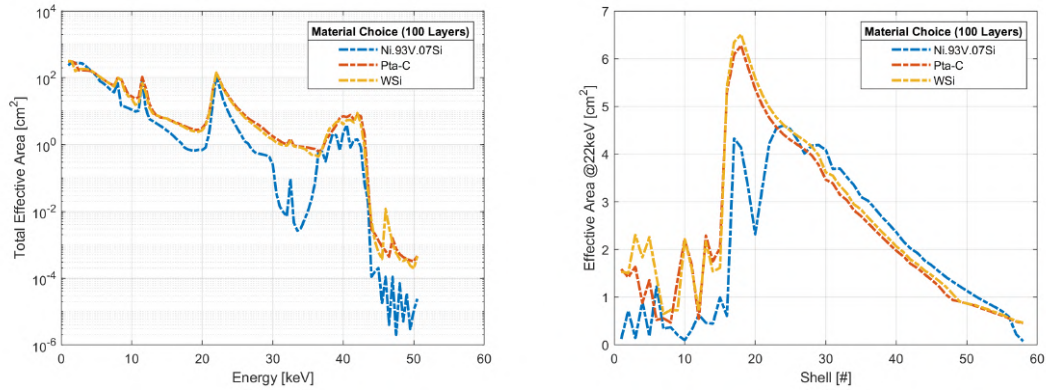
$$\Gamma = \frac{d_1}{d} = \frac{d_1}{(d_1 + d_2)} \in [0.4 - 0.6] \quad (3.6)$$

The value of Γ lies in the range of [0.4 - 0.6], indicating that one material constitutes from 40% to 60% of the bi-layer.

Due to oxidation phenomena from metal surfaces, the low-density, non-metallic layers are placed on top. In the following Paragraph 3.3, we will discuss the optimization process in detail. However, Figure 3.3 already shows the best results obtained from different material combinations.

The optimal solution consists of 100 layers (50 repetitions) of Tungsten and Silicon with constant thicknesses. The lower reflective performance of Tungsten proves to be valuable, as it poorly reflects energies other than the 22 keV peak, thereby increasing the contrast in the screening image. Moreover, at 22 keV, this specific coating recipe yields the largest effective area, amounting to 144.014 cm².

Figure 3.3b illustrates the peak effective area at 22 keV as a function of the contribution from each ring.



(a) Total effective area as function of energy. (b) Effective area at 22 keV as function of shell.

Figure 3.3: Comparison of various bi-layer material combinations. Each coating consists of 100 layers, specifically optimized for the grazing angle of its shell.

3.2 GEOMETRICAL PARAMETERS OPTIMIZATION

Following the previous section, we want to find the optimal focal length, the mean radius (and equivalently the grazing angle) of each shell based on the optimal spacing.

3.2.1 MIRRORS LENGTH

The optimization parameter for the mirrors' length, represented by HP , was initially considered; however, it was eventually fixed at 16 cm, Eq. (3.2), due to in-house manufacturing constraints. Longer mirrors have advantages in terms of projected area and complexity, as they require fewer nested shells. Nonetheless, there are drawbacks to using longer mirrors, such as challenges in achieving coating uniformity, concerns about stress fractures, and limitations in the dimensions of the coating chamber.

3.2.2 FOCAL LENGTH

Considering Equation (3.1), it is advantageous to have a longer focal length since, for a given mean radius, this results in a smaller grazing angle, thereby improving the reflectivity [7]. However, there is an angle, called critical angle, below which total reflection condition applies. Since, the primary objective of the optical module is to monochromate, we aim to avoid such a condition. As men-

3.2. GEOMETRICAL PARAMETERS OPTIMIZATION

tioned, the critical angle depends on the chosen material properties. Consequently, we will explore various material combinations to identify a satisfactory focal length (as long as possible while not too long to avoid total reflection) and then finalize the optimal length choice.

While typical space telescopes have focal lengths up to 20 meters [44], such lengthy free-space propagation is impractical for a general hospital room. Thus, taking into account the considerations mentioned earlier, we have arbitrarily chosen a focal length of 270 cm, resulting in a total length of 300 cm for the DM machine (30 cm to place the patient breast and the compression plate).

This design allows for inclusion or compatibility with the dimensions of a clinical or Magnetic Resonance Imaging (MRI) table setup. For reference, a sketch of this hypothetical machine is depicted in Figure 3.4.

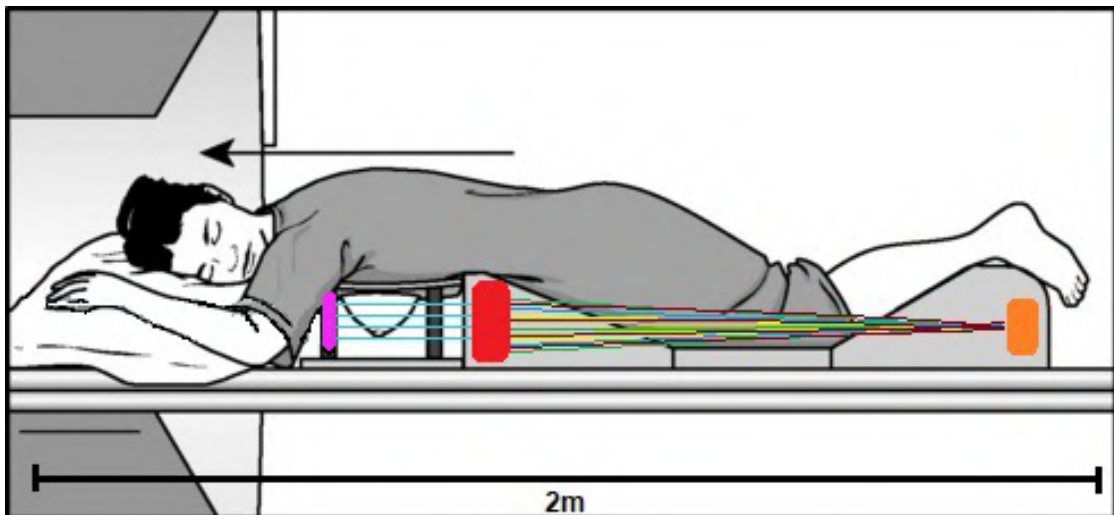


Figure 3.4: Breast MRI clinical bed-table can be tuned to host the DM machine. The setup has (right to left): x-ray tube (orange), polychromatic and diverging light, optical module (red), monochromatic and collimated light (cyan), breast (white) and detector (purple). Image adapted from [50].

It is evident that this optical module is no longer suitable for application in a conventional DM machine. In such machines, the source-to-detector distance is typically only 65 cm (Figure 2.4). Considering a vertical space of 30 cm for the compression plate mechanism, the available focal length would be only 35 cm, which is insufficient to effectively reflect x-rays due to the large grazing angle of such a design.

By re-imagining the entire mammography setup, transitioning from a vertical

orientation (Figure 2.4) to a horizontal one (Figure 3.4), we can better utilize the space beneath the clinical bed. With a 3-meter-long table, we can now accommodate a focal length of 270 cm. However, the introduction of a horizontal setup requires appropriate shielding to prevent the patient from being irradiated during the procedure.

3.2.3 SHELLS' SPACING

The design of the optical module takes into account the need to fully picture an adult woman's breast, which has maximum dimensions of 25 cm wide, 8.6 cm thick, and spans 17.4 cm, see Paragraph 2.1.2. To match the detector area of existing DM machines, which are usually $24 \times 30 \text{ cm}^2$, the outer radius of the optical module is chosen to be 15 cm. The inner shell radius is not constrained, except for manufacturing considerations. When the mirror curvature exceeds 2.5 cm of radius, the coating has problems at adhering to the surface and can present stress cracks, thus diminishing the performance.

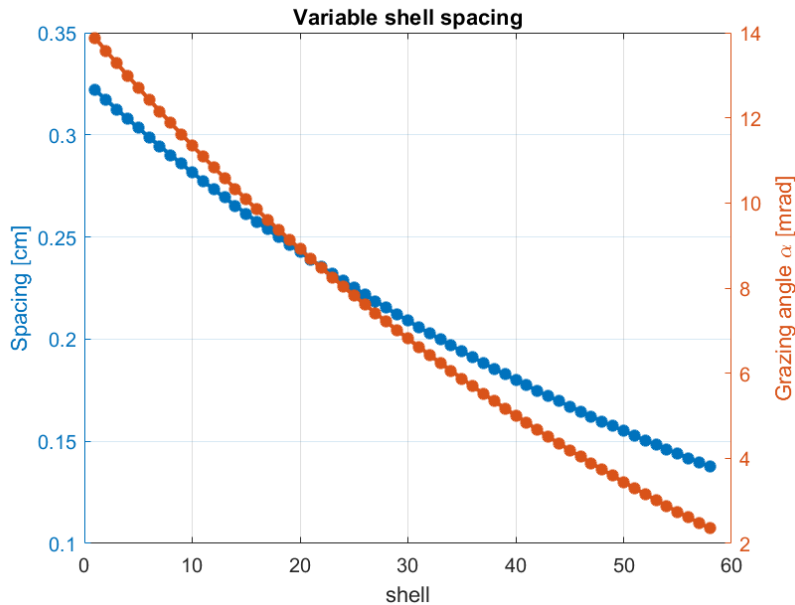


Figure 3.5: Variable spacing between shells (outermost to innermost) and relative grazing angle.

To prevent shadowing or overlapping of successive outer shells, a variable spacing between the shells is employed. The spacing is carefully designed to meet this requirement while simultaneously maximizing the projected area for photon collection. As we progress from the outer radius (15 cm) to the innermost

3.3. COATING PARAMETERS OPTIMIZATION

radius (2.5 cm), the outermost shell is assigned the largest spacing, and the spacing gradually decreases for each subsequent inner shell. The variable spacing as a function of the inverse ring number, (1 is outer-most) is reported in Figure 3.5. On the same graph, the relative grazing angle is also reported, to underline how, in a variable space design, it is not linear.

3.3 COATING PARAMETERS OPTIMIZATION

The main objective of this paragraph is to optimize the number of equal bi-layers, denoted by N_{rep} , along with their specific thickness (d) and coupled Gamma (Γ), which vary depending on the shell number. In this effort, we differentiate between independent and optimization parameters, which include:

Independent:

- **Energy:** the purpose of the optical module is to monochromate the incoming radiation to a 22 keV beam. Considering the available x-ray tube, the emitted radiation spans between 1 and 40 keV.
- **Grazing Angle:** from 13.8746 down to 2.3526 mrad, the grazing angles are fixed by the geometry optimization (Figure 3.5), i.e. 58 reflection measurements.
- **Substrate:** The substrate is always Silica (SiO₂), and for the simulation has indefinite length. In reality, high energy photons could be transmitted through the 0.78 mm silica structure, thus worsening the monochromator performance.
- **Roughness/Diffuseness:** multiple high/low and low/high density interfaces are present in the model. We reasonably assume that the deposition technique (sputtering) leads to an equal roughness on all of them. The standard deviation in the coating surface (roughness) is assumed to be 2.5Å.

Optimization:

- **Gamma:** the ratio of thickness between the high and low density layers. The value of Γ lies in the range of 0.4 to 0.6 .
 - **Thickness:** using Equation (3.6), the thickness of the high and low density layers d_1 and d_2 are coupled via the parameters Γ and d ; their sum (d) must be at least 30Å due to sputtering limitations. We arbitrarily set the upper limit to be 150Å, however, as we will shortly demonstrate, the inner layers, which are thicker than the outer, are never thicker than 145Å.
 - **Number of repetitions:** for each shell, for a given thickness and ratio, a number N_{rep} of repeated identical bi-layers can be stacked one on top of each other.
-
-

Table 3.3: Independent and Optimization parameters for the coating recipe.

3.3.1 THICKNESS AND GAMMA

Referring to Table 3.3, the optimization parameters are three, thus forming a 3-dimensional space. To simplify the analysis, a fixed number of repetitions is supposed, $N_{rep} = 100$ for example. This reduces the parameter space to two dimensions, consisting of d (thickness) and Γ (ratio) values. By simulating reflectance curves over different thicknesses ($d \in [30 - 150]\text{\AA}$) and ratios ($\Gamma \in [0.4 - 0.6]$) with a resolution of 1\AA and 0.02 , respectively, we can represent the optimization space in a more intuitive 2-dimensional fashion (Figure 3.6).

The plot in Figure 3.6 corresponds to shell number 10, displaying two distinct peaks. Outer shells (close to $n = 1$) show more intricate structures within the optimization space, while inner ones (close to $n = 58$) exhibit the total reflectance behavior. In the latter case, for a given threshold thickness, the effective area experiences a sudden increase depending on Γ , eventually reaching a plateau.

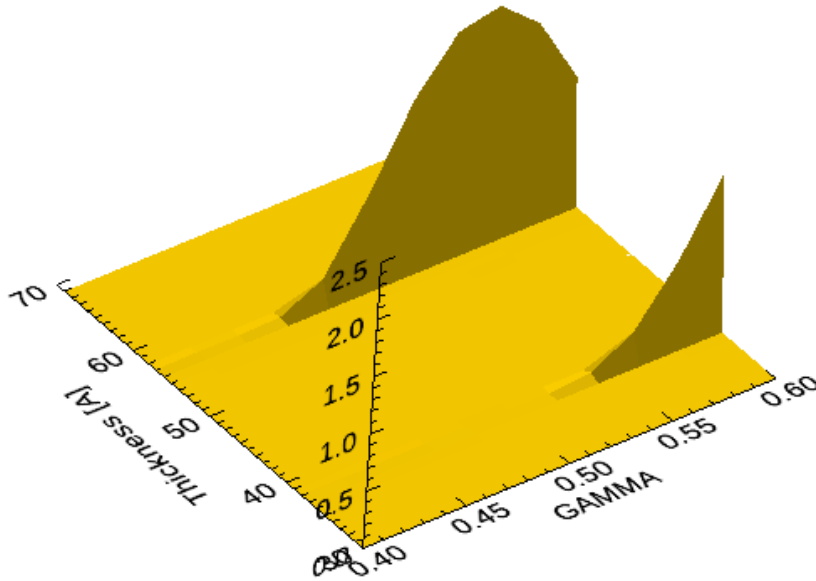


Figure 3.6: Shell n.10, coated with 100 repeated W/Si bi-layers, optimization space of effective area in cm^2 at 22 keV.

To achieve a resolution even lower than 1\AA , the highest peak in Figure 3.6 is fitted with a modified Gaussian curve added to a first degree polynomial interpolation of the plateau (ground). The fitting function implemented in IDL is given by Equation (3.7), where $A_{eff}(p)$ represents the effective area as a function

3.3. COATING PARAMETERS OPTIMIZATION

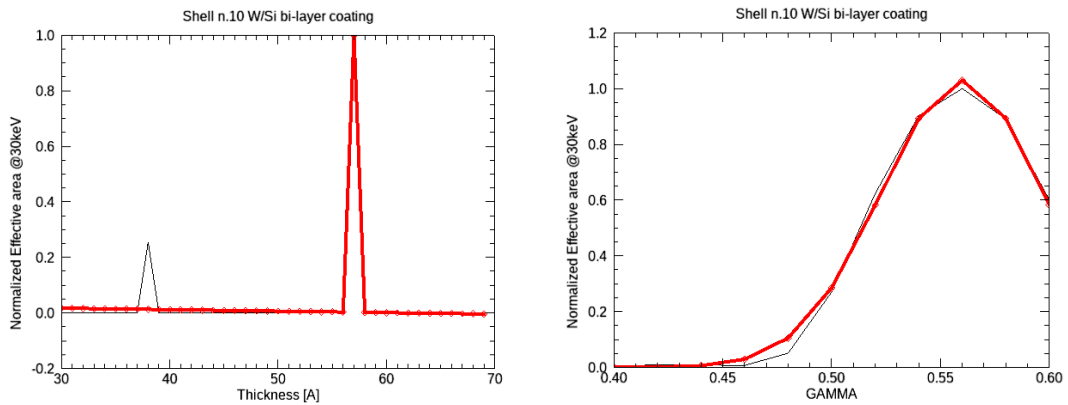
of a parameter p that can either be thickness or Gamma.

$$A_{eff}(p) = A_0 e^{\frac{-z^2}{2}} + A_3 + A_4 E \quad , \quad z = \frac{p - A_1}{A_2} \quad (3.7)$$

Incidentally, achieving such a high level of precision (sub-Angstrom) during real production may be extremely challenging, especially considering that the atomic radius of most materials is typically in the range of 0.3 to 3 Å. As a result, the maximum effective area calculated theoretically may not be fully achievable in practical applications.

As depicted in Figure 3.6, the effective area peak may not necessarily represent the best solution due to the limitations of the resolution. However, by utilizing Equation (3.7), we can fit the two optimization profiles (normalized for the convenience of the algorithm) and accurately determine the values of d and Γ that maximize the reflectivity. In the case of multiple local maxima, the analysis selects the one with the highest amplitude.

Figure 3.7 presents the results of this fitting process. In Figure 3.7a, the effective area profile at 22 keV is shown as a function of thickness (d) for shell n.10 with 100 repeated W/Si bi-layers. The black curve represents the actual optimization profile, while the red curve depicts the corresponding Gaussian fit of the highest peak. Similarly, Figure 3.7b displays the effective area profile at 22 keV as a function of gamma (Γ) for the same shell and bi-layer configuration.



(a) Thickness Optimization Analysis

(b) Gamma Optimization Analysis

Figure 3.7: Shell n.10, with 100 repeated W/Si bi-layers, effective area at 22 keV profile as function of thickness and gamma (black) with corresponding Gaussian fits (red) of the highest peak.

3.3.2 NUMBER OF REPETITIONS

In the previous section, we introduced the optimization process for bi-layer thicknesses and ratios. Now, we utilize an IDL script to iteratively test different repetition numbers. Figure 3.8 shows the total effective area, Eq. (3.4), as a function of both energy and the number of repetitions for a W/Si coating, which was determined to be the best combination from the material analysis (Section 3.1.2). Additionally, the single-layer and the one bi-layer curves are included to highlight the necessity of the bi-layer structure for mono-chromating.

It is important to note that the maximum allowed number of repetitions is set to 300, since exceeding this number is unfeasible due to potential formation of cracks caused by coating stiffness [51].

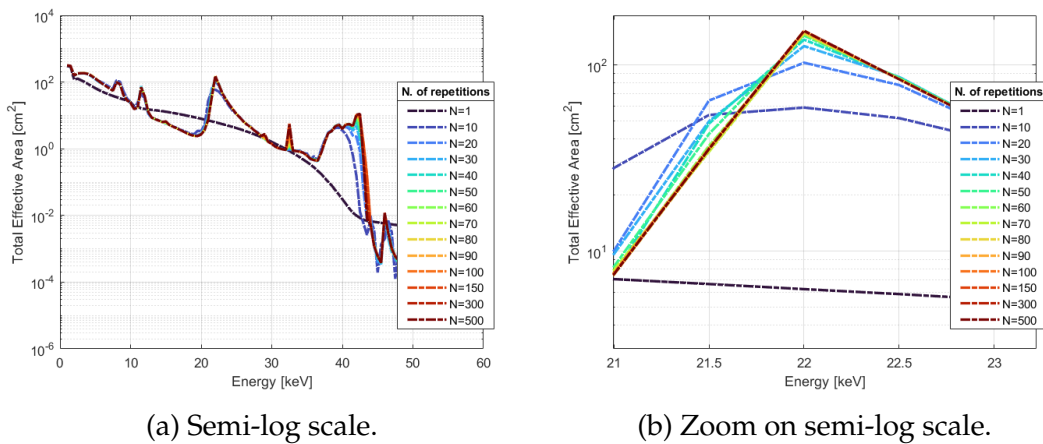


Figure 3.8: Total effective area as function of energy calculated for different repetition numbers.

To determine the optimal number of repetitions, we analyzed the peak effective area values at 22 keV, as depicted in Figure 3.9. This graph clearly shows that after approximately 60 repetitions, the effective area improvement becomes minimal. This behavior has to be attributed to absorption effects. As the number of repetitions increases, the coating become thicker, leading to increased absorption. Consequently, the benefits in reflection achieved by having more bi-layers are counterbalanced by the absorption introduced by the additional layers, as described by the Beer Law, Equation (2.1).

Moreover, in the same Figure, the data was fitted using a rational model with second-order polynomials. This model provides an estimate of the asymptotic

3.4. PROPOSED OPTICAL MODULE DESIGN

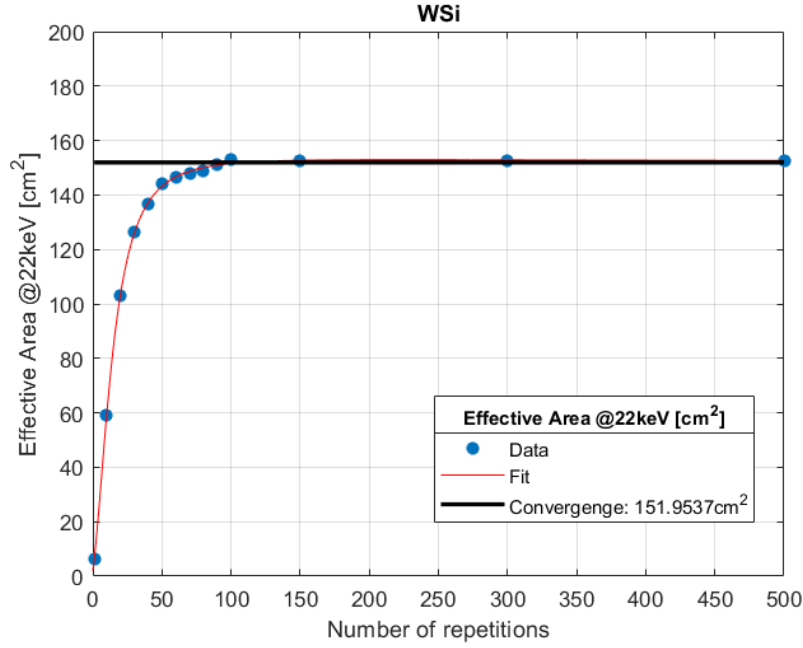


Figure 3.9: Effective area at 22 keV (linear scale) as function of the repetition number.

value, which was determined to be 151.95 cm^2 . Based on this analysis, the optimal number of repetitions appears to lie within the range of 40 to 60, representing the elbow of the curve. We also considered the technical challenges associated with stacking more and more layers on top of each other, particularly in terms of deposition time and vertical uniformity in the coating structure. Thus, a lower number of repetitions is preferred from a manufacturing standpoint.

After careful consideration, we selected $N_{rep} = 50$ as the optimal number of repetitions. With this configuration, the effective area is 144.015 cm^2 , which corresponds to 94.78% of the maximum asymptotic value. This choice balances the trade-off between manufacturing feasibility and achieving a high effective area for the optical module.

3.4 PROPOSED OPTICAL MODULE DESIGN

In Figure 3.10 the final geometrical design of the optics is reported. The axis of the image are in the same scale but one axis has been cutted to give the reader a better understanding of the design. In reality, the system looks much more longer ($Z_0 = 270 \text{ cm}$) than wider ($r_{out} = 15 \text{ cm}$). The x-ray source and the detec-

tor are also present. X-ray propagating close to the optical center ($r < 2.5$ cm) can be blocked using an absorption filter which is not drawn.

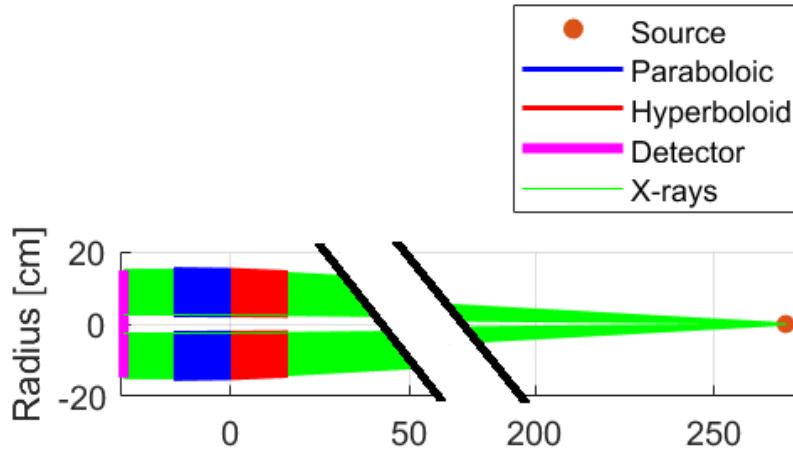


Figure 3.10: The dimensions of the proposed Wolter Type-I design for the optical module.

In Figure 3.11a, we present the top-view of the optical module with breasts pair, where each breast has dimensions of 9 cm wide and 8 cm broad, overlaid on it. It is evident that trying to screen both breasts simultaneously will not be feasible, as they do not entirely fit within the illumination region. This is consistent with conventional mammography, where each breast is imaged separately. Observing the compressed breast shape superimposed on the detector plate, it becomes apparent that the entire rectangular detector surface (24×30 cm²) is not necessary; only a half of it is required.

This concept is explored and visually explained in Figure 3.11b. The half-optic module, is simply the reduction of the original fully circular design into a half-circle optical module. Consequently, the projected area is reduced from 412.47 cm² down to half, i.e. 206.23 cm². So far, all the graphs included in this report, refer to the full-optic design. To obtain information about the half-optic performances, one must divide by 2. As an extra example, the effective area at 22 keV will now be 72 cm² for the half optic.

Table 3.4 summarizes the results obtained from the geometry optimization process, providing the radius, grazing angle, and projected area (A_p) of each shell. The total projected area is 412.47cm²; i.e. 60.02% of the available area (outer cir-

3.4. PROPOSED OPTICAL MODULE DESIGN

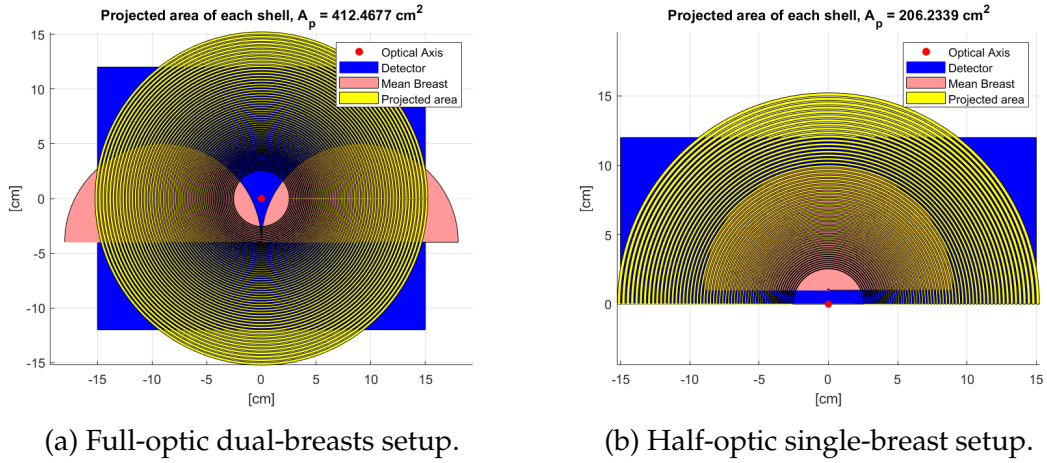


Figure 3.11: Top-view of the parabolic (secondary) mirror projected area (yellow) onto the breast sample (pink) and detector plate (blue).

cle area minus inner circle one). Since it is not possible to further decrease shell spacing, because of shadowing and support structure, to further improve projected area, one must increase the length of each coated plate, in order to reduce the number of rings. However, as stated, this is not possible, as the maximum length of mirrors is 16 cm.

In the same table, the optimal solutions from the coating optimization investigation are reported. These solutions represent the total thickness and the Γ ratio of the bi-layer for each ring. Starting from the innermost shells (n. 58), the optimal thickness gradually decreases until ring n. 16, where the 30\AA coating limitation prevents thinner layers. From this point onwards, towards the outermost shell (n. 1), the algorithm explores the optimization space to find the best effective area at 22 keV. The total thickness of each coating is the thickness of the designed bi-layer multiplied by 50, corresponding to the repetition number. This total thickness ranges from $0.15 \mu\text{m}$ at minimum to $0.725 \mu\text{m}$ at maximum.

The reflectivity and effective area calculations are specifically focused on the energy line of interest (22 keV) and are related to the projected area using Equation (3.5). The performance reduction due to the thickness limit is evident from the effective area plot presented in Figure 3.3b. Using the tabulated optimal values to model a 100 W/Si bi-layer coating, the theoretical effective area curve aligns with the one previously presented in Figure 3.8. At 22 keV, the effective area peaks at 144.015 cm^2 , which corresponds to 34.92% of the projected area.

CHAPTER 3. OPTICAL MODULE DESIGN

Shell [#]	Geometry: Wolter Type I			Coating: W/Si 50 bi-layers (at 22 keV)			
	R [cm]	α [mrad]	A_p [cm ²]	D [Å]	Γ	R [%]	A_{eff} [cm ²]
1	15.00	13.87	21.08	62.0	0.46	26.96	1.532
2	14.68	13.58	20.18	63.8	0.53	27.31	1.505
3	14.36	13.28	19.32	65.0	0.48	34.53	2.304
4	14.05	13.00	18.49	66.7	0.53	31.48	1.832
5	13.74	12.71	17.69	68.0	0.48	35.73	2.258
6	13.44	12.43	16.92	46.4	0.40	29.00	1.423
7	13.14	12.16	16.17	47.9	0.60	20.03	0.649
8	12.84	11.88	15.46	49.0	0.60	21.76	0.732
9	12.55	11.62	14.77	50.0	0.40	22.18	0.727
10	12.27	11.35	14.10	51.0	0.40	39.62	2.214
11	11.99	11.09	13.46	52.0	0.40	34.45	1.598
12	11.71	10.83	12.85	54.0	0.60	23.61	0.716
13	11.44	10.58	12.25	55.0	0.40	42.01	2.163
14	11.17	10.33	11.68	56.0	0.40	36.32	1.541
15	10.90	10.09	11.14	58.0	0.40	38.05	1.612
16	10.64	9.85	10.61	30.0	0.54	71.48	5.420
17	10.38	9.61	10.10	30.0	0.60	79.26	6.346
18	10.13	9.37	9.61	31.0	0.40	82.29	6.510
19	9.88	9.14	9.15	32.0	0.42	81.26	6.039
20	9.63	8.91	8.70	33.0	0.44	80.23	5.597
21	9.39	8.69	8.26	34.0	0.46	79.68	5.246
22	9.15	8.47	7.85	35.0	0.46	79.61	4.974
23	8.91	8.25	7.45	36.0	0.46	80.03	4.771
24	8.68	8.04	7.07	37.0	0.46	80.81	4.614
25	8.45	7.83	6.70	38.0	0.44	81.86	4.489
26	8.23	7.62	6.35	39.0	0.42	83.09	4.382
27	8.01	7.41	6.01	40.0	0.40	84.42	4.283
28	7.79	7.21	5.69	41.0	0.40	85.56	4.163
29	7.57	7.01	5.38	42.0	0.40	85.99	3.976
30	7.36	6.81	5.08	44.0	0.40	84.39	3.618
31	7.15	6.62	4.80	45.0	0.40	86.01	3.547
32	6.95	6.43	4.52	46.0	0.40	85.89	3.337
33	6.74	6.24	4.26	48.0	0.40	86.32	3.176
34	6.54	6.06	4.01	50.0	0.40	85.70	2.948
35	6.35	5.87	3.78	51.0	0.40	86.69	2.838
36	6.15	5.70	3.55	53.0	0.40	86.83	2.675
37	5.96	5.52	3.33	55.0	0.40	86.89	2.515
38	5.77	5.34	3.12	57.0	0.40	87.00	2.365
39	5.59	5.17	2.93	59.0	0.40	87.07	2.219
40	5.40	5.00	2.74	62.0	0.40	86.90	2.068
41	5.22	4.84	2.56	64.0	0.40	87.22	1.947
42	5.05	4.67	2.39	66.0	0.40	86.62	1.792
43	4.87	4.51	2.23	70.0	0.40	87.21	1.693
44	4.70	4.35	2.07	74.0	0.40	86.81	1.561
45	4.53	4.19	1.92	76.0	0.40	87.15	1.462
46	4.36	4.04	1.79	80.0	0.40	86.89	1.348
47	4.20	3.89	1.65	84.0	0.40	86.07	1.224
48	4.04	3.74	1.53	90.0	0.40	83.51	1.065
49	3.88	3.59	1.41	96.0	0.40	80.31	0.909
50	3.72	3.44	1.30	98.0	0.40	81.69	0.866
51	3.56	3.30	1.19	105.0	0.40	84.03	0.841
52	3.41	3.16	1.09	115.0	0.40	85.20	0.792
53	3.26	3.02	1.00	120.0	0.40	86.29	0.742
54	3.11	2.88	0.91	130.0	0.40	87.01	0.688
55	2.97	2.75	0.83	140.0	0.40	87.68	0.634
56	2.82	2.61	0.75	145.0	0.40	87.10	0.567
57	2.68	2.48	0.67	145.0	0.60	85.87	0.497
58	2.54	2.35	0.61	145.0	0.60	87.73	0.466
Total:	412.47 cm ²			144.015 cm ²			

Table 3.4: Optimal radius (spacing), calculated grazing angle, calculated projected area, optimal thickness, gamma, calculated reflectivity, and calculated effective areas (at 22 keV) per each shell in the optical module with a Wolter Type-I geometry where each shell is coated with 50 specific W/Si bi-layers.

4

Manufacturing and Assembly

This chapter focuses on the physical implementation of the proposed optical module by describing the manufacturing process of prototypes. These prototypes consist of flat substrates coated with a specific ring recipe. We chose to prototype three mirrors: one in the outer group, one in the middle, and one in the inner group.

Moreover, the assembly of an experimental setup for x-ray imaging validation will be presented. In particular, this setup is designed to test individual x-ray mirrors of smaller dimensions compared to the full optical module design.

Finally, the technical challenges faced during the manufacturing process will be addressed, and the data-analysis required for making informed design choices will be thoroughly discussed.

4.1 SUBSTRATE CLEANING

In this paragraph, our focus is on characterizing surface roughness, specifically for the bottom substrate, before proceeding with the coating process. Understanding the roughness properties of the substrate is crucial for subsequent steps in the coating procedure and analysis, as introduced in Paragraph 2.2.1.

4.1. SUBSTRATE CLEANING

4.1.1 CLEANING PROCEDURE

In our study, we adapted and simplified the cleaning procedure used for the mirrors of the NuSTAR mission [52]. Specifically, the NuSTAR cleaning process comprised an acidic soap bath and a running deionized (DI) water rinse followed by acetone and ethanol baths, another DI rinse, and finally blow-dried using dry Nitrogen. In our laboratory, we adopted a simplified cleaning procedure based on this approach, making use of similar equipment. The process consists of the following steps:

1. **Ultrasonic Soap Bath:** the substrates undergo a 10-minute hot ultrasound bath in deionized water with added acid detergent at a temperature of 60°C. This step removes dirt and organic contaminants from the sample surface.
2. **Ultrasonic Water Bath:** the substrates undergo a 10-minute ultrasound bath in deionized water to wash out soap residues.
3. **Ethanol Bath:** the substrates are immersed in a 99.9% pure ethanol bath for 5 minutes to further remove any leftover organic or grease contaminants.
4. **Water rinse:** the substrates are rinsed with running deionized water to ensure that all cleaning agents are thoroughly washed away.
5. **Blow-drying:** to prevent water stains and detergent residues, both sides of the substrates are gently dried using a pressurized nitrogen gun, ensuring a uniform drying process. This step is particularly crucial because ethanol evaporates rapidly (within 1 minute).

In Figure 4.1, the cleaning equipment consisting of three different stages is pictured. On the left side, two bathtubs are immersed in two larger ultrasound tanks containing water. This setup allows the ultrasonic waves to propagate effectively to the internal bathtubs. Before starting the cleaning process, an external immersion heater is used to heat up the water in the first bathtub and tank.

The sink, the faucet for DI water rinsing, and the nitrogen gun are positioned on another side of the clean-room and not shown in Figure 4.1. Moreover, the substrates are loaded on a holder that can be moved around with a cart.

Figure 4.2 shows a picture of the cleaned substrate. By, visual inspection alone, it is not possible to distinguish the original from the cleaned substrate. To gain deeper insights into the surface properties (such as roughness) after the cleaning procedure, further analysis using optical or Scanning Probe Microscopy (SPM) is necessary.



Figure 4.1: The cleaning setup inside DTU Multilab. Three separate bathtubs: hot soap water, deionized water and ethanol.

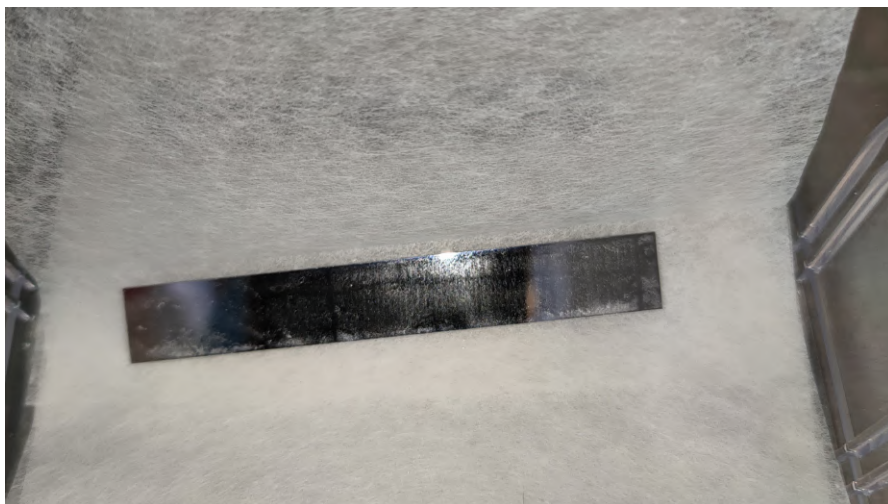


Figure 4.2: The cleaned substrate, surrounded by anti-static dust-free paper, dimensions: 70 mm x 10 mm x 0.78 mm.

4.1.2 SCANNING PROBE MICROSCOPE

After the cleaning process, the effects it had on the surface of the substrate must be investigated. In this regard, Atomic Force Microscopy (AFM) measurements are conducted on a central area of the substrate, which spans $500 \times 500 \text{ nm}^2$.

While it is advisable to measure multiple spots across the sample (left, center, and right) and then average the results, time slot availability with the AFM instrument allowed us to measure only the central spot. Incidentally, the center spot corresponds to the region where the incident beam will be focused during

4.1. SUBSTRATE CLEANING

the subsequent experiments (as shown later in Figure 5.3).

The comparison aims to determine whether the substrate roughness has decreased after the cleaning process. Roughness is critical in measuring any imperfections or irregularities that could deform the subsequently deposited layer. The AFM images of the substrate before and after cleaning are presented in Figure 4.3.

4.1.3 LEVELLING

The data obtained from Scanning Probe Microscopy often come in the form of raw data calculated as vertical distance measured from the top plane of the cantilever. However, these data are not levelled.

The choice of levelling method for SPM data should depend on the system configuration. For systems with independent scanners for each axis, plane levelling should be sufficient. On the other hand, for systems with scanners moving in all three axes (tube scanners), a 2nd order polynomial levelling method should be used [11]. It is important to note that while higher-order levelling methods can be applied to the data, they may suppress real surface features, such as waviness, and alter the statistical functions and quantities evaluated from the surface.

To correct and flat the recorded data, Gwyddion, presented in Paragraph 1.2.5, can be utilized. The correction process involves aligning the rows (corresponding to the cantilever scanning direction) using a 1st-degree polynomial approximation and flattening the base to account for the non-horizontal nature of the surface. Additionally, the zero level is adjusted to the lowest point ensuring only positive height values.

4.1.4 GRAIN MASK

There are several grain-related algorithms implemented in Gwyddion. One common approach is using simple thresholding algorithms, where the user has direct control over the height, slope and curvature threshold criteria.

For data with more complex patterns, segmentation algorithms can be utilized to identify and mark grains or particles more effectively. The segmentation algorithm is particularly useful for identifying local minima (or maxima), as the positions of grains can be seen as local extremes on the surface.

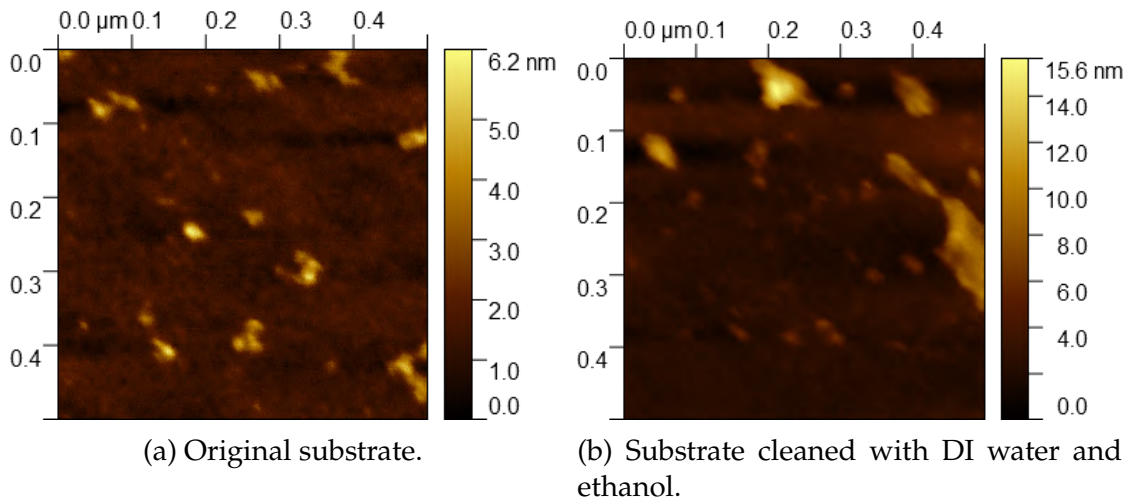


Figure 4.3: Atomic Force Microscopy (AFM) 500x500nm to determine substrate roughness prior to coating.

Generally, the result is an image fully segmented to motifs, each pixel belonging to one or separating two of them. By default, the algorithm marks valleys rather than upward grains, thus being very convenient for AFM as shown in Figure 4.4.

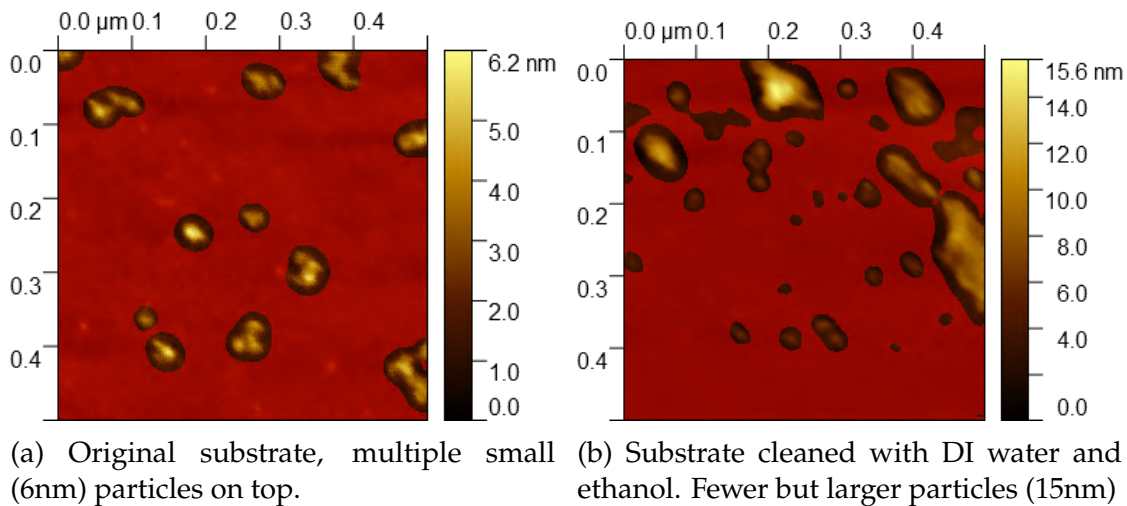


Figure 4.4: Atomic Force Microscopy (AFM) 500x500 nm² to determine substrate roughness prior to coating. Region of interest marked using the segmentation algorithm.

4.1. SUBSTRATE CLEANING

4.1.5 STATISTICAL ANALYSIS

After applying the segmentation algorithm and processing the data, relevant statistical quantities such as the average roughness S_a can be calculated.

The average roughness is similar to the Root Mean Square (RMS) value, but with a difference in the calculation approach. Instead of using the sum of squared differences from the average, S_a is calculated from the sum of absolute values of data differences from the average. The roughness mean represents the mean of all the differences (r_j) of all points (z_j) in the roughness profile from a mean line (\bar{z}) over the evaluation length, and its mean value is zero. The average roughness follow as:

$$r_j = z_j - \bar{z}$$
$$S_a = \frac{1}{N} \sum^N |r_j|$$

The results of the roughness calculations for the surface are reported in Table 4.1, where the analysis is performed on all the image pixels or by excluding large grains. The exclusion of large grains may be necessary in some cases to focus the analysis on the finer details of the surface and avoid bias from larger features.

Substrate	Original	Cleaned
Roughness (entire image)	3.325 Å	10.2 Å
Roughness (grain excluded)	2.354 Å	4.167 Å

Table 4.1: Statistical roughness from AFM data analysis.

The most important observation from the analysis is that the cleaning process did not reduce the surface roughness, and there is a possibility that it may have even increased it due to the introduction of fewer but larger particles, as observed in Figure 4.4. However, due to the limitation of analyzing only one spot, a definitive conclusion cannot be drawn on whether the roughness increased or not. Further analysis involving averaging data from different areas over the sample would provide more reliable results.

Considering that the cleaning did not improve the average roughness, it is preferable to use uncleaned samples for the coating process. For instance, a different cleaning method, such as Plasma ashing may have reduced roughness.

In conclusion, the analysis has highlighted bounds for substrate roughness in future experiments, such as X-ray Reflectivity, where the substrate roughness can be an unknown factor. To ensure reliable results with such technique, a substrate roughness lower than 2 or exceeding 10 Å will not be reasonable.

4.2 MAGNETRON SPUTTERING COATING

Magnetron sputtering deposition was introduced in Paragraph 2.2.2. The purpose of this section is the description of the coating of 6 x-ray mirrors using three different bi-layers profiles and repetitions.

4.2.1 RING SPEED CALIBRATION

Before being able to coating the substrate with the chosen design, there is a need to calibrate the magnetron sputtering machine.

The procedure consists in pre-coating with the chosen materials three samples at three different and arbitrarily speed rings. Incidentally instead of a simple bi-layer, 20 layer repetitions (i.e. 10 bi-layers) are deposited on top of each sample, in order to enhance the Bragg peaks intensity during the XRR data fitting analysis.

In fact, after coating, XRR is performed on the calibration samples to determine the actual thickness of each layer in the bi-layer. Given now the relationship between speed ring and thickness deposited, we can determine the desired ring speed for the coating of the designed X-ray mirror. To do so, the simplest way is use to the proportional relationship formula:

$$\omega_1 : d_1 = \omega_2 : d_2$$

Where ω_i is the ring speed expressed in step/s and d_i the corresponding deposited material thickness in Å. It is important to notice that speed and thickness have inverted proportionality, at high rotation speed the thickness is little, while during a slow rotation, more material is being deposited.

However, since three calibration substrates have been coated, three data points (ω_i, d_i) per material are available. Therefore, instead of the proportion formula, we can use a more general model named *Rat01*, since it is a rational fraction

4.2. MAGNETRON SPUTTERING COATING

where the unknown has degree zero at the numerator and degree one at the denominator.

The required velocity is a function $f(p_1, q_1, x)$ of the desired thickness (x) and two fitting parameters: p_1 for scale and q_1 for offset.

$$f(p_1, q_1, x) = \frac{p_1}{x + q_1} \quad (4.1)$$

In Figure 4.5, the calibration points data fitting is reported along with the position (ring speed) of the desired thicknesses for the X-ray module. For instance, prediction bounds are also included in the results to demonstrate that a linear fit, indicating a proportional relation between the two quantities, is not valid.

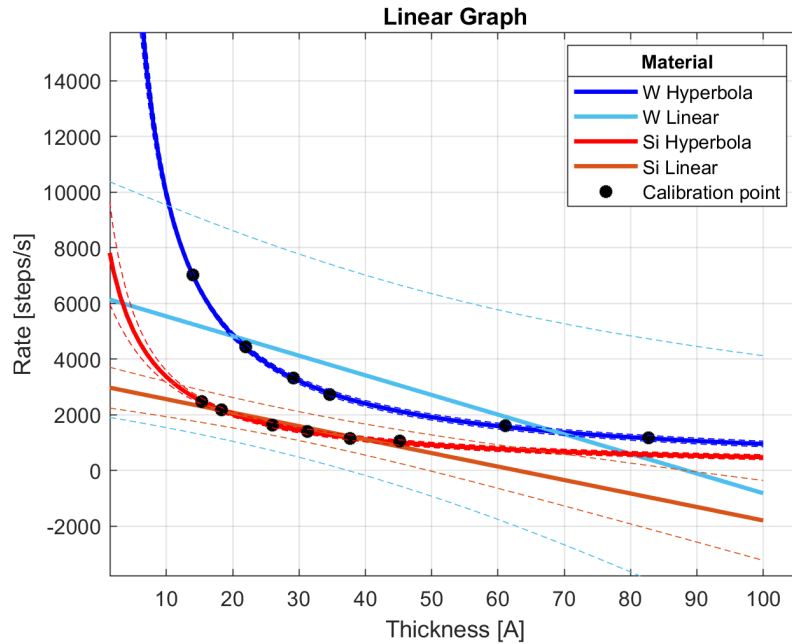


Figure 4.5: Ring rate calibration according to hyperbolic law compared with linear law. The dotted lines represent the 95% prediction error bounds.

4.2.2 COATING DEPOSITION

The bi-layers materials are Silicon (Si) on top of Tungsten (W), to prevent oxidation of Tungsten in the top layer, on top of a Silica (SiO₂) substrate. The repetitions are 50, the minimum allowed bi-layer thickness is 30Å and the maximum is 150Å. The gamma ration varies between 0.4-0.6 and the total thickness of the

coating has range 150-500nm. The chosen rings and their corresponding sputtering parameters are summarized in Table 4.2, and they have been extracted from Table 3.4.

Shell [#]	Angle [°]	D [Å]	Γ	Rep. [#]	D tot. [nm]	D_{Si} [Å]	ω_{Si} [step/s]	D_{Si}	ω_{Si} [step/s]
10	0.6504	51	0.6	50	255	30.6	1397	20.4	4434
17	0.5371	30	0.6	50	150	18	2185	12	7022
43	0.2585	70	0.6	50	350	42	1053	28	3325

Table 4.2: Properties of the selected shell mirrors' and required ring speed ω for their coatings.

The total time to deposit 100 individual layers is 10 hours and 55 minutes.

The positions of the substrates inside the coating chamber are depicted in Figure 4.6. Notably, two samples are mounted for each position, resulting in a total of 6 samples, where pairs of two identical coated mirrors are produced. The identifiers $S30$, $S50$, $S70$ indicate the substrate (S) followed by the desired bi-layer thickness according to Table 4.2.

An entire rotation of the ring (360°) corresponds to 668000 steps, and the sputtering cone from a target is approximately 45° even if the target-substrate 'visibility' is 60° . Therefore, it is more convenient to express the deposited thickness via the ring speed parameter as performed during calibration in Paragraph 4.2.1.

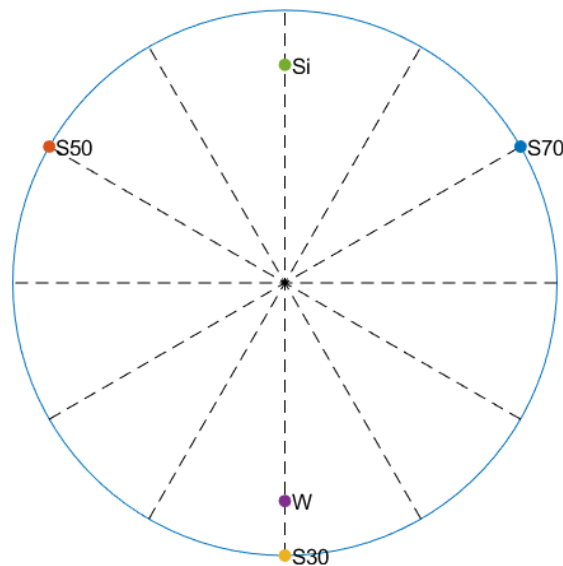


Figure 4.6: Starting position for the coating run. Pre-sputtering of Silicon active. The mounting points for the three samples and the magnetrons are visible as well as 30° lines.

4.2. MAGNETRON SPUTTERING COATING

Standard parameters for the coating run have been already reported in Table 1.1: the power applied to the magnetron is 350W, the target to sample distance is 155mm, and the pressure inside the chamber is 2.8 mTorr. Before starting the pre-sputtering and the actual sputtering, semi-vacuum needs to be achieved in the chamber. Internal pressure as a function of time is reported in Figure 4.7 for the whole duration of the coating run. It has to be noticed that the pump-down has been performed during the night prior the morning of 31 march 2023, the day of the run.

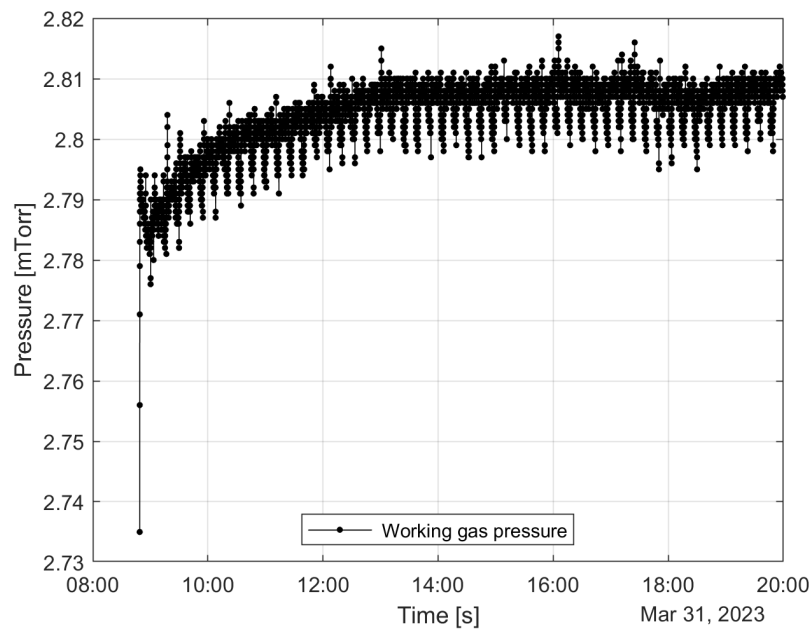


Figure 4.7: Pressure logbook for the Magnetron sputtering run.

The power applied alternatively to each magnetron support is shown in Figure 4.8 altogether with the current ring speed.

The figure shows the pre-sputtering process of Silicon ("Power 4") followed by Tungsten ("Power 3"), each lasting 300 seconds (5 minutes). In between these two processes, the ring was rotated at the fastest available speed (7000 steps/s) by 60° clockwise (with reference to Figure 4.6) to prevent Tungsten pre-sputtering material onto sample S30.

Incidentally, the first layer coating (Tungsten) can begin for all three substrates, starting from S70 (the thicker substrate with the lower ring speed) and progressing towards S30 (the fastest substrate). Before depositing Silicon, the entire ring

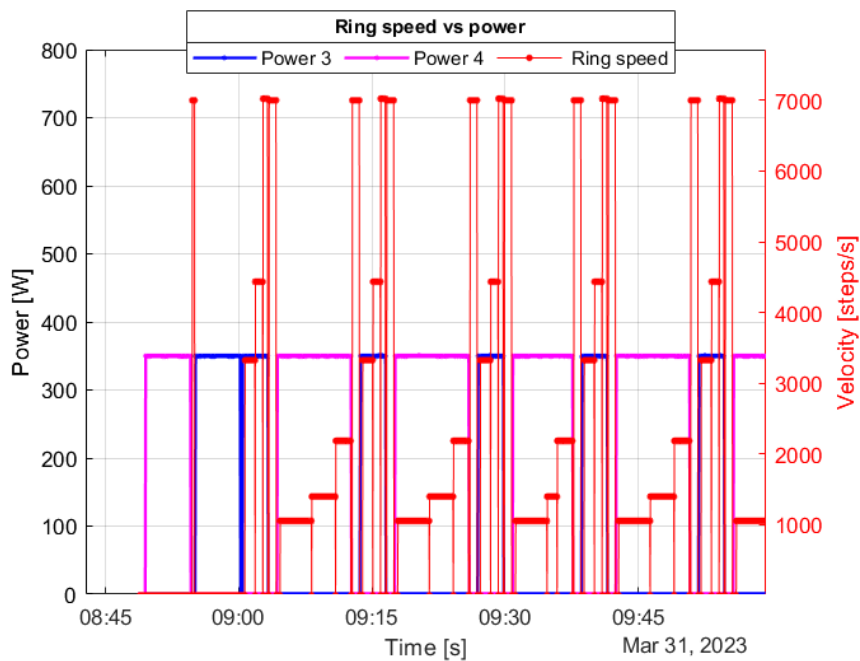


Figure 4.8: Logbook for the Magnetron sputtering run.

must be rotated by 180° , at the fastest available speed, so that *S70* becomes again the first to be coated.

The coating process proceeded smoothly until the third cycle, where the coating of *S50* was only partially carried out due to the ring spinning at the faster rate intended for *S30*. The cause of this change in ring speed is unclear, and it could have resulted from a mechanical failure, such as a bolt scratching the chamber walls, or a software glitch.

Regardless of the nature of the issue, in the next paragraph, we will characterize the as-coated substrates using XRR data-fitting with a complex model to account for the drawback. This will help determine that the coating is still close to the desired one despite the encountered challenges.

4.3 COATING CHARACTERIZATION

The step following the collection of XRR measurements, is data fitting those points using a model for the coating structure. Specifically, three similar models were tested, each of them having a different number of parameters to be fitted as reported in Table 4.3. The main difference between them is the increasing grade of freedom of the third bi-layer from the bottom, i.e. the one involved in the coating drawback. The three structure models are:

1. **Simple Model:** this is the original model, i.e. 50 identical bi-layers, all with same Gamma and thickness and equal roughness between the layers.
2. **Intermediate Model:** this is a of the variation initial model, consisting of 47 uniform bi-layers on top and 3 uniform bi-layers at the bottom. With the exception of the top layer, it is assumed that the roughness between all layers is equal.
3. **Complex Model:** this is a modified version of intermediate model, intended to more accurately depict the software malfunction. The bottom two bi-layers are the same, as are the top 47. However, the fifth and sixth layers from the bottom, which are the high and low index layers of the third bi-layer, are entirely unrelated to the rest of the structure.

4.3.1 X-RAY REFLECTIVITY FITTING PROCEDURE

First, instead of fitting the entire reflectivity curve, only the range 0.2° - 3° is considered. Looking at Figure 4.9, it is clear that for the first few very small grazing angles, the readout should be one, since the sample is below the critical angle, i.e. total reflection condition (100% reflectivity). Therefore, we exempted those points from the fitting. Then, above 3° , systematic errors are not negligible and dominates the measurement, so fitting this region can be actually counterproductive. Moreover, we are less interested in his upper range of grazing angles, since for the optical module prototype, the mirror should be placed in order to maximize reflectance from its first Bragg peak, which happens below 1° for all the three coated samples.

Second, the fitting procedure is not complex, but rather long and time demanding. It is a cycle whose main steps are:

1. We start by imposing some of the fitting parameters as frozen, such as the bottom bi-layers thickness, their roughness and Γ . Therefore only the upper layers' thicknesses represents the population for the genetic evolution. In the paragraph 3.3, we presented the coating parameters to be fitted. It

is reasonable given a parameter, its fitted value should be within a 20% bound on their designed values. If several unsuccessful (not satisfactory) converging attempts follows, the bounds need to be increased.

2. The bounds are constrained again and shrunk around those new converging values.
3. While leaving the multi-layer thicknesses as fitting parameters, a new parameter (Γ or σ for example) is de-frozen. Given now a good fit of one parameter, we return to the first step to determine the next.

At the beginning of each cycle, genetic evolution (Paragraph 2.3.4) fitting is performed. Before starting a new one, it is important to check the FOM, and the reduced chi-square statistic χ^2 (the former should be increasing while the later decreasing towards one) in order to understand if the procedure is converging and to avoid data over-fitting ($\chi^2 < 1$).

Even more important, knowledge of the coating process, can allow us to determine that a 30Å roughness is not a plausible value (too high) for the sputtering technique and that the genetic evolution is only trying to improve the FOM by “washing” out bad fitted peaks.

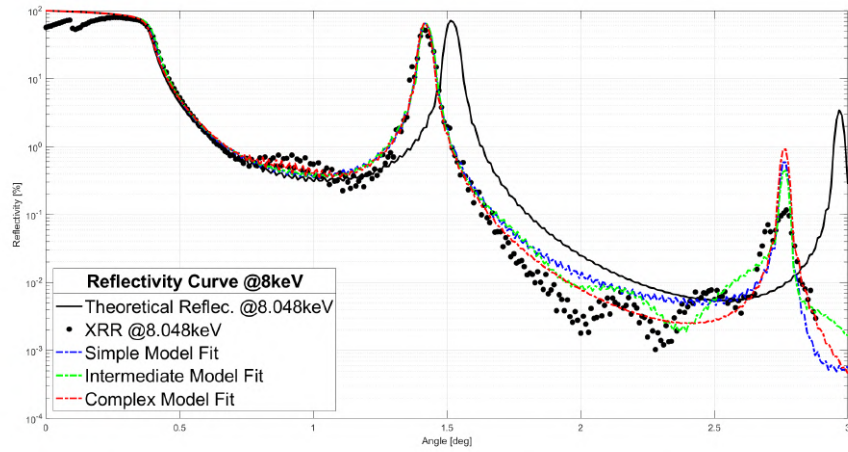
4.3.2 X-RAY REFLECTIVITY RESULTS

The measured XRR data point from the as-coated substrates, together with the theoretical model (from the simulation) and the fitting models are shown in Figure 4.9. The models fitting parameters to plot the reflectivity curves in Figure 4.9 have been reported in Table 4.3 together with statistical metrics for comparing goodness in data fitting.

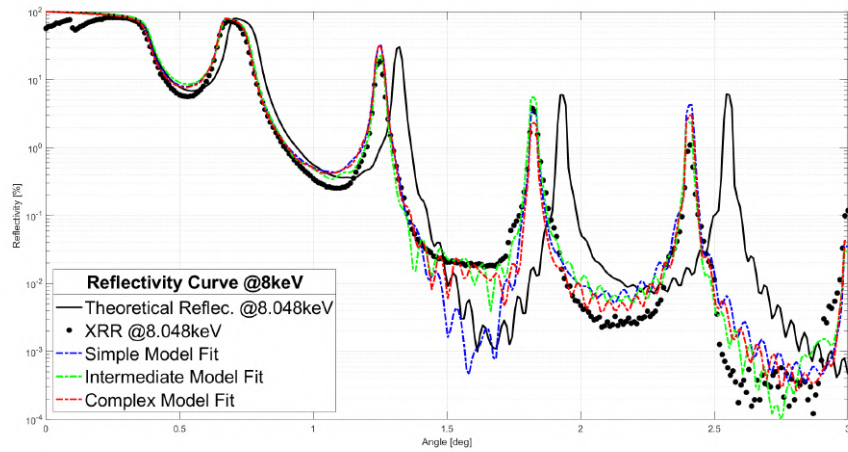
Typically, when the variance of the measurement error is known beforehand, a chi-squared value (χ^2) significantly greater than 1 ($\chi^2 > 1$) indicates a poor fit of the model. Ideally, a chi-squared value close to 1 ($\chi^2 \approx 1$) indicates a satisfactory agreement between observations and estimates, considering the error variance. Conversely, if the chi-squared value is less than 1 ($\chi^2 < 1$), it suggests that the model is over-fitting the data by either improperly fitting noise or overestimating the error variance.

Based on the results (see Table 4.3) it can be concluded that the simple model can describe, even if not with complete accuracy, the actual coating structure. Efforts were made to enhance the fitting precision, aiming to reduce χ^2 , using both the intermediate and the complex models. The latter model, with a higher

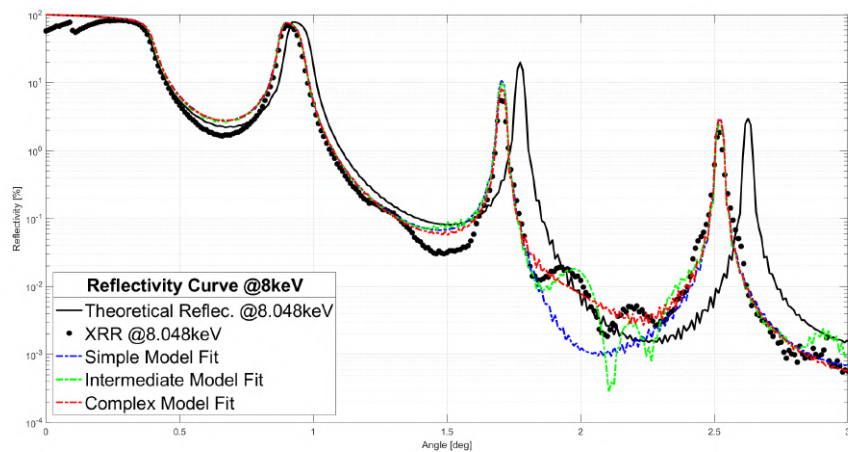
4.3. COATING CHARACTERIZATION



(a) Mirror: ds0307.



(b) Mirror: ds0309.



(c) Mirror: ds0311.

Figure 4.9: X-ray Reflectivity (XRR) data fitting from IDL/IMD using three different models and comparison with the theoretical model from the design phase.

Theoretical Model					Simple Model					
						ds0307	ds0309	ds0311		
					χ^2	999	1539	1025		
Structure			ds0307	ds0309	ds0311	Structure				
Top Layer	σ		2.5	2.5	2.5	Top Layer	σ	26.35	30	19.97
	D		30.00	70.00	50.00		D	32.30	74.28	53.21
	Γ		0.60	0.60	0.60		Γ	0.57	0.61	0.57
Bi-Layer N = 50	Si layer		18.00	42.00	30.00	Bi-Layer N = 50	Si layer	18.34	45.15	30.59
	W layer		12.00	28.00	20.00		W layer	13.96	29.13	22.62
	W/Si σ		2.5	2.5	2.5		W/Si σ	3.94	3.40	3.43
Substrate	σ		2.5	2.5	2.5	Substrate	σ	1.59	19	9.99

Intermediate Model					Complex Model					
						ds0307	ds0309	ds0311		
					χ^2	932.8	989	841		
Structure			ds0307	ds0309	ds0311	Structure				
Top Layer	σ		30	30	25.99	Top Layer	σ	12.43	30	30
	D		32.29	74.40	53.20		D	32.29	74.28	53.22
	Γ		0.60	0.58	0.57		Γ	0.60	0.61	0.57
Bi-Layer N = 47	Si layer		19.37	43.38	30.54	Bi-Layer N = 47	Si layer	19.37	45.61	30.23
	W layer		12.92	31.02	22.66		W layer	12.92	28.67	22.99
	W/Si σ		4.10	3.79	3.60		W/Si σ	4.10	3.85	3.56
Bi-Layer N = 3	D		52.73	59.93	91.78	Free layers	Si layer	33.98	45.13	7.05
	Γ		0.65	0.66	0.69		Si σ	7.75	3.97	6.07
	Si layer		34.01	39.67	62.96		W layer	18.74	14.43	13.41
	W layer		18.72	20.26	28.82		W σ	7.75	3.97	6.07
	W/Si σ		4.10	3.79	3.60		D	52.73	86.27	21.53
Substrate	σ		4.10	3.79	3.60		Γ	0.65	0.48	0.40
						Bi-Layer N = 2	Si layer	34.01	40.98	8.61
							W layer	18.72	45.29	12.92
							W/Si σ	13.16	5.09	4.86
						Substrate	σ	12.85	12.85	12.85

Table 4.3: The XRR parameters for the theoretical model, together with the one fitted via the simple, intermediate and complex models. Thickness and roughness are in Angstrom, gamma is adimensional.

number of parameters, offers a more comprehensive description of the events that occurred during the final coating process. As a result, the complex model will be adopted and utilized for further analysis.

Using the best-fit model from XRR data fitting we now know the structure and composition of the coating. This allows for a further step, i.e. simulating the ex-

4.3. COATING CHARACTERIZATION

pected performance of the mirror at 22 keV rather than 8 keV. Those simulations are reported in Figure 4.10, on a linear scale to highlight the first Bragg peak, for all three mirror samples.

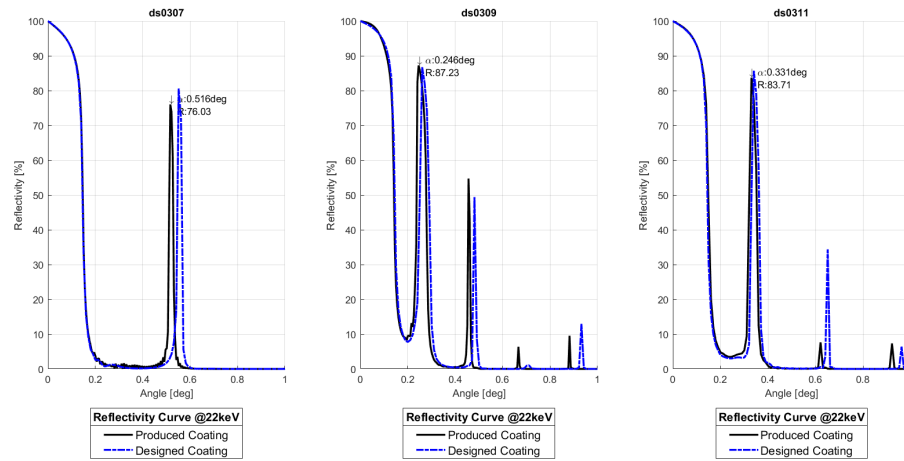


Figure 4.10: The simulated reflectivity of mirrors (ds03 /-07 /-09 /-11) at 22 KeV is shown with the first Bragg peak angle marked, and it is compared to the simulation from the design (engineering) phase.

In the same graph, we present the reflectivity curves that were simulated based on the engineering design. Achieving precise manufacturing of mirrors with accurate grazing angle geometries is crucial for the proposed optical module, given its nested geometry. The importance of accuracy arises from the fact that the narrowest first Bragg peak in Figure 4.10 (ds0307) has a FWHM of approximately 0.02° . Any deviation in the coating structure thickness leads to a corresponding deviation in the grazing angle, making it unsuitable for the proposed Wolter Type-I geometry prototype.

The initial coating design was ambitious, with 50 repetitions, a number uncommon in the literature. Furthermore, the thinnest layer was designed to have a thickness of only 30 \AA , and the manufactured layer's thickness was 32.39 \AA , resulting in a minimal error of 2.39 \AA . This achievement is remarkable, considering that the atomic radius of Tungsten is 2.02 \AA and that of Silicon is 1.46 \AA . Generally, from the XRR data analysis, the largest error in thickness is approximately 4.28 \AA , with a corresponding Gamma error of only 3%. Additionally, the estimated roughness between interfaces is comparable to the experimental measurements obtained from AFM.

It should be noted that the top surface roughness has higher values than realistic, as the fitting algorithm tried to smooth the curve by increasing the roughness to improve the fitting statistics. However, the top roughness limit was fixed at 30 Å, which is a relatively high value for this parameter and does not significantly influence the precision of the thickness or Gamma fitting, but rather enhances the overall χ^2 statistic.

Despite the challenges faced during the manufacturing process and the deviations registered in the coating structure, we can still validate the benefits of monochromatic radiation in mammography applications. From this point onwards, our focus will mainly be on this aspect and its potential advantages.

4.4 SAMPLE PREPARATION

The ideal sample for validating the technology would have been a phantom breast designed for mammography, similar to the one depicted in Figure 4.11. These phantoms are specifically created to mimic the characteristics of real breast tissue and are used for calibration and quality assurance in mammography imaging. They are manufactured by authorized companies approved by National Institute of Standards and Technology (NIST) and must adhere to specific regulations and standards [53].

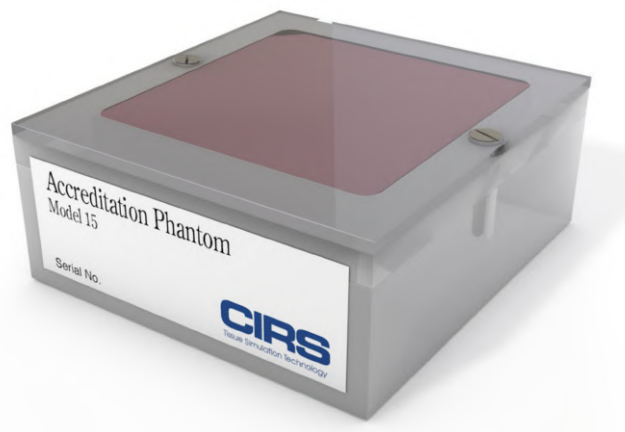


Figure 4.11: The CIRS ¹ Model 015 Mammographic Accreditation Phantom. Source [53].

¹Computerized Imaging Reference Systems (CIRS) is an American company active in the medical field.

4.4. SAMPLE PREPARATION

4.4.1 PHANTOM BIO-SAMPLE USING EQUINE TISSUE

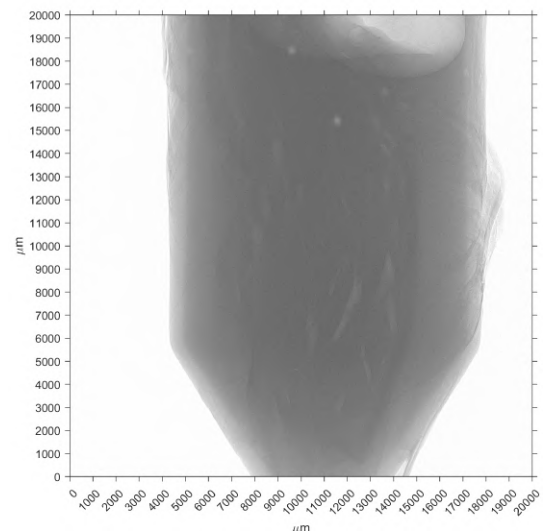
Unfortunately, due to budget limitations, the ideal phantom breast for mammography validation was not available. As an alternative, bio-lumps of animal origin were considered, as obtaining human tissue requires approvals from the Danish Ethical Commission.

Equine tissue samples, such as the one shown in Figure 4.12, were readily available. An X-ray projection of the sample was acquired at the 3D-imaging center, DTU Physics, using a detector with a resolution of 5 microns. However, it became evident that the features of the sample, such as the fat lines between muscle tissues are not representative of cancer formations [54]. Furthermore, they were not suitable to be effectively imaged by our prototyped setup, as our detector resolution is only 55 microns.

Furthermore, it was recognized that the equine tissue sample is better suited for tomography, where a 3D model of the intricate fat ramification can be computed. In contrast, for conventional radiograms, it is easier to image layers of tissue that are uniform along the x-ray propagation direction.



(a) Camera picture.



(b) X-ray projection. $5\mu\text{m}$ resolution.

Figure 4.12: Equine bio-lumps provided by the 3D-imaging center, DTU Physics.

Indeed, given the limited availability of phantom breast options, a custom-made bio-sample was considered as a solution. This custom sample allows for the simulation of a cancerous mass using millimeter-sized grains, which provides

a larger region of interest for statistical purposes, particularly for Contrast to Noise Ratio (CNR) evaluation. It becomes possible to assess the performance of the optical module in detecting and imaging these simulated masses.

4.4.2 PHANTOM BIO-SAMPLE USING SWINE TISSUE

The use of swine meat as a phantom for mammography applications is not a new concept in the literature, although it has primarily been applied in ultrasound techniques [55]. However, there have also been experiments carried out using swine tissues in diffraction x-ray mammography [56]. In our study, the custom bio-sample consists of a portion of swine belly where distinct fat and muscular tissues are clearly connected, providing a homogeneous phantom for simulating adipose breast tissue, Figure 4.13.

The composition of breast calcifications has been the subject of multiple studies. It is well understood that there are two main types of calcifications. Type I, which consists of calcium oxalate (CaC_2O_4), is considered a benign tumor, while Type II involves depositions of calcium phosphate, such as Hydroxyapatite ($\text{Ca}_5(\text{PO}_4)_3\text{OH}$), which is considered a sign of malignancy [57]. The size of calcifications can vary, ranging from micro-calcifications that are only 0.5 mm in diameter to pop-corn calcifications that can reach up to 3 mm in size. These calcifications often appear in clusters within areas that can be several centimeters in diameter [54].

To simulate the presence of cancer in the custom bio-sample, previous studies have used calcium salts (CaCl) or graphite (C) as substitutes for representing the calcifications [56]. In the absence of these specific materials, sodium salt (NaCl) has been employed as an alternative. While sodium salt may not perfectly mimic the exact chemical composition of breast calcifications, it provides a practical and compatible (in dimensions) mean for simulating its presence.

With the help of a surgical scalpel, we successfully cut and separated the various layers of tissue constituting the sample depicted in Figure 4.13. The specific composition of our bio-sample can be broken down as illustrated in Figure 4.14.

Now, using the experimental setup (that will be presented in Paragraph 4.5), and the spectral functionality of the detector, we are able to perform absorption analysis on each individual component in the bio-sample, to determine its Lin-

4.4. SAMPLE PREPARATION

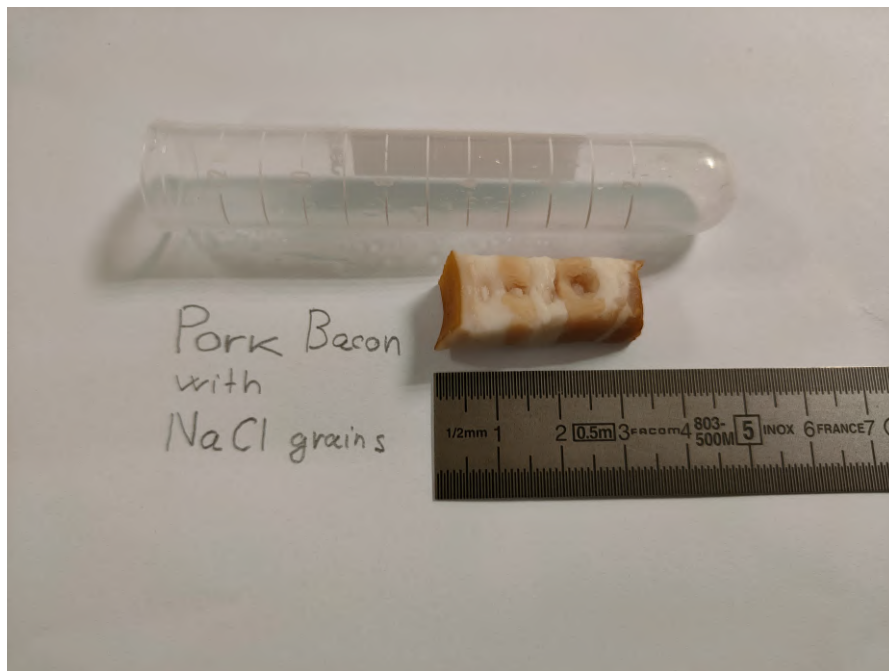


Figure 4.13: Bio-sample: Swine belly with sodium chloride grains.

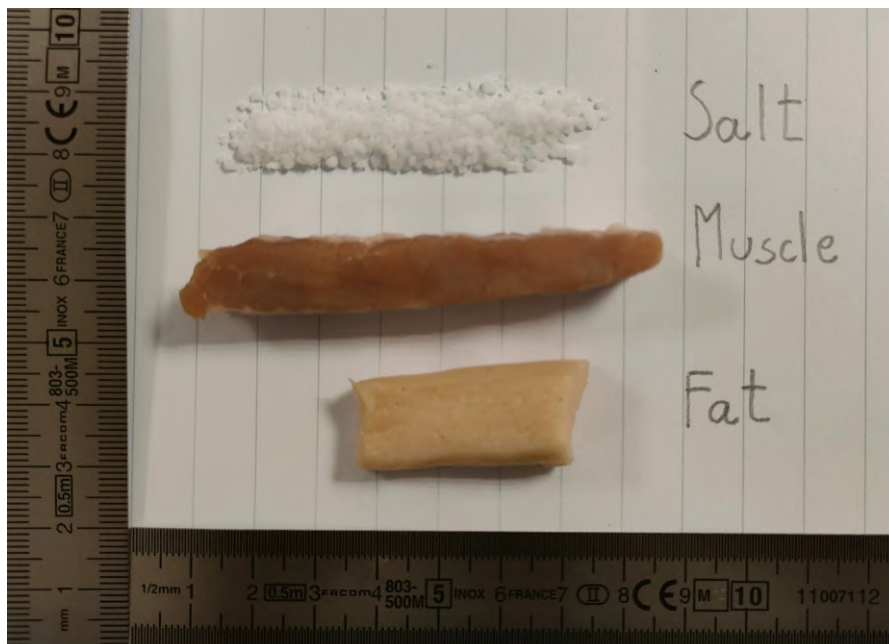


Figure 4.14: Bio-sample composition: swine fat, muscle and NaCl grains to be tested for Linear Absorption Coefficient (LAC) determination.

ear Absorption Coefficient (LAC) at 20 keV. This particular energy is chosen to enable comparison with tabulated values of commonly used materials for tissue mimicking. The results of these comparisons are presented in Table 4.4.

To compute the Linear Absorption Coefficient (LAC), we need two spectrum measurements: one with the examined element present and one without it. Additionally, we require information about the absorption thickness, in a process similar to the one described in Paragraph 2.3.1 for dose calculations. For the experiment, the sample is placed in a test tube and securely held in front of the detector using a 3D-printed support. To ensure consistency in the results, the absorption effect of the plastic tube itself has been carefully subtracted from the final measurements presented in this study.

Modality	Energy (avg)	Patient or Reference Material	LAC	Measured Material	LAC
Textured mammography phantom, non-anatomical representation	20 keV	50% adipose - 50% glandular tissue	0.64	Swine Fat	0.56
				Swine Muscle	1.77
		Sodium chloride NaCl	11.89		
		Calcium oxalate CaC2O4	9.75	NaCl	5.98
		Hydroxyapatite Ca5(PO4)3OH	19.28		

Table 4.4: Tabulated Linear Absorption Coefficient (LAC) cm^{-1} values of studied bio-sample compared to actual breast tissue properties at 20 keV. Adapted from [55].

It is interesting to note that the LAC of swine fat is very similar to that of a breast composed of 50% adipose and 50% glandular tissues. Although we only reported one tabulated value for breast composition, breast tissues with higher percentages of adipose distribution are even closer to our bio-sample.

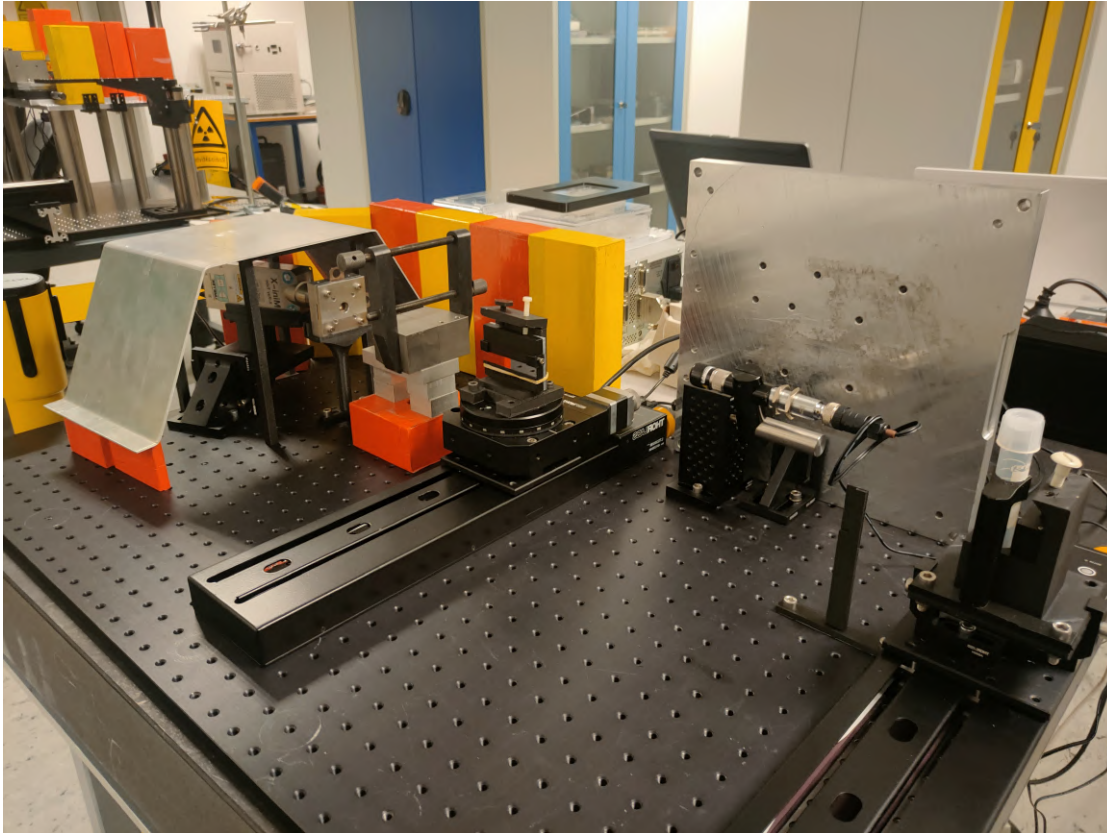
On the other hand, the calcium salt used to simulate cancerous formations has an absorption coefficient closer to benign cancer formations (calcium oxalate) rather than malign ones (calcium phosphate). All these values have been computed using XCOM, introduced in Paragraph 2.1.3. Moreover, the tabulated LAC for sodium chloride is 11.89 cm^{-1} , however, we measured a value of 5.98 cm^{-1} during our experiment. The discrepancy can be explained by the fact that the calcium salt grains are inserted into the test tube, and while they are touching each other, there are also cavities and air spaces between them. These spaces reduce the overall absorption, leading to the lower measured value.

4.5 ASSEMBLY OF THE EXPERIMENTAL SETUP

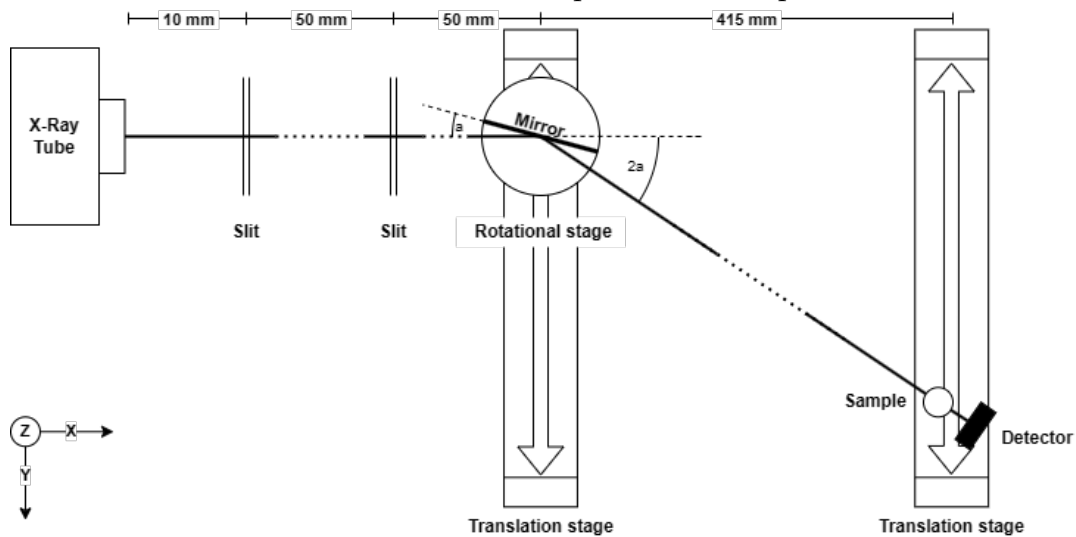
The setup used in this study closely resembles the setup implemented in the FCXR laboratory or presented in similar works [25], [26]. A sketch of the setup is shown in Figure 4.15b, and it consists of the following essential components:

1. **X-ray source:** A Mini-X2 X-Ray Tube from Amptek [58] with a Silver anode, equipped with a 3 mm circular collimator and capable of a maximum power output of 4W. A detailed description is presented in section 4.5.1.
2. **Slit #1:** This component shapes the beam height to 1 cm and the width to 0.2 mm using fixed-sized (and interchangeable) copper slits housed in an aluminum casting. These slits are 1 mm thick, which means they are thick enough to absorb 100% of off-axis radiation at 22 keV. At 40 keV, the absorptance of the slits is 98.72%.
3. **Slit #2:** This component shapes the beam width to 0.2 mm using two wide aluminum blocks separated by 0.2 mm aluminum sheets (spacers) and press together by a metal pincer. The length of the spacers and blocks is 50 mm, thus absorbing 100% of the radiation at 22 keV and 99.99% at 40 keV.
4. **Optical element:** One multi-layer mirror mounted via a special support to a roto-translation stage. The manufacturing of the full-fledged optical module was not possible due to project constraints, instead three multi-layers mirrors of compact size have been manufactured as described in Section 4.2. Each mirror belongs to a different shell and therefore has a specific grazing angle (Figure 4.10). We chose to mount sample ds-0307 in a custom made bracket since it is the mirror with the larger grazing angle, allowing for a better separation on detector plate between the position of the direct beam compared to the reflected one.
5. **Bio-Sample:** The sample used in the experiment is the custom bio-sample made of swine belly with distinct fat and muscular tissues, presented Section 4.4.2. It is held in front of the detector frame using a test-tube and a special arm-like support.
6. **Translational Stage:** The Thorlabs LTS300 is a 300 mm linear translation stage with integrated controller [59]. It is used for precise translational movements of both the optical module and the detector along the Y-axis of the setup, and the stepper motor has an on-axis accuracy of $<\pm 5 \mu\text{m}$.
7. **Rotational Stage:** The Thorlabs HDR50 is a heavy-duty rotation stage with stepper motor which allows rotational adjustments of the mirror [60]. In particular it has an accuracy of $\pm 820 \mu\text{rad}$ ($\pm 0.047 \text{ deg}$).
8. **Detector:** MiniPIX TPX3 from Advacam has a 14 mm x 14 mm Silicon plate with a thickness of 500 μm , the matrix has 256 x 256 pixels so the pixel resolution is 55 μm [61]. This detector enables fully spectral X-ray imaging, as it records the spectrum of measured X-rays in each pixel. The maximum count rate is 2.35 million hit pixels per second. The detector

has a minimum energy threshold of 2.7 keV and maximum of 60 keV. The quantum efficiency of the detector can be found via Equation (2.2).



(a) Camera Picture of the setup build on the optical bench.



(b) Diagram sketch of the setup. Measurements in [mm] are not in scale.

Figure 4.15: The setup consists in: (i) X-ray source, (ii) two slits, (iii) a multi-layer mirror mounted on a rotational stage, (iv) the sample and (v) the detector are mounted on a moving cart rail.

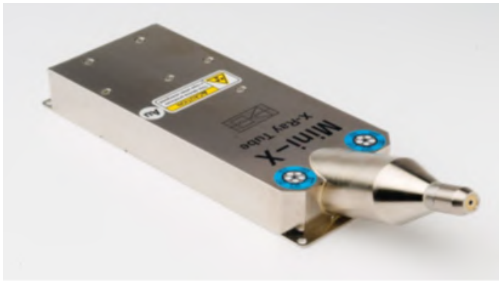
4.5. ASSEMBLY OF THE EXPERIMENTAL SETUP

In addition to the components depicted in the simplified sketch in Figure 4.15b, the final setup (as shown in Figure 4.15a) also includes several other components that were used during the experiments. These additional components include:

- **Laser:** By emitting a beam of green light (520 nm), the laser provides a visible indicator on a graduated paper sheet in order to adjust the height and position of the components thus achieve precise alignment of the different elements in the setup. The use of safety goggles with filters specifically designed for direct laser protection is mandatory.
- **Test-tube holder:** A plastic test tube is securing the sample in place and maintaining its shape during experiments. Additionally, it simplifies the process of cold storage maintenance. It is important to note that plastic exhibits a very low cross section at 22 keV. To ensure accurate calculations of the overall absorbed dose by the bio-sample, the flux absorbed by the plastic has been subtracted and accounted for.
- **Shielding:** Both aluminium (metal sheet 3 cm thick) or lead blocks (yellow and red bricks) are employed as means of providing additional protection to shield the user from radiation escaping the setup. While the beam divergence from the X-ray tube (as stated by the manufacturer) is 30° , and the beam propagation plane is transversal from the observer point, shielding may not be strictly necessary but it is implemented for added safety precautions. Furthermore, a Geiger-Müller counter is employed to continuously measure the radiation flux directed towards the user.
- **Workstations and power supply:** Two workstations are utilized in the setup: one to monitor the X-ray tube while measuring events from the detector, and the another to control the Thorlabs actuators and stages. These workstations are interconnected with the peripherals through USB standards. While the detector is self-powered through USB, all the other electronic components require an external power source. These components often need specific voltage levels therefore, an external Direct Current (DC) power supplier is utilized to provide the appropriate voltage.

4.5.1 MINI-X2 X-RAY TUBE

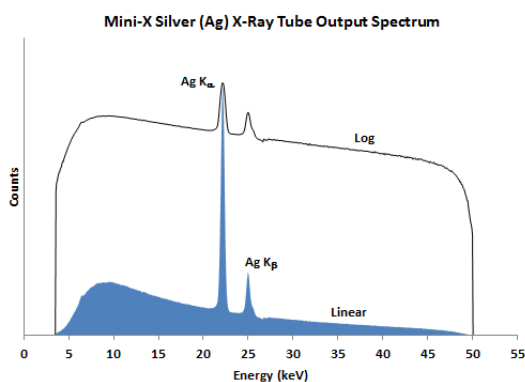
The Amptek *Mini X-ray tube* generates high intensity X-ray radiations up to 4W in tube power emission. The Mini-X2 has both variable current and voltage which can be software controlled via a standard USB connection. It features a maximum of 50 kV/200 μ A power supply, a Silver (Ag) transmission target and other specifications that are summarized in Figure 4.16. Since the anode is made of Silver, the emitted spectrum exhibits strong peaks around Silver K-alpha and K-beta lines, which are at 22.16 and 24.94 keV, respectively. This is clearly visible in the manufacturer available spreadsheet as depicted in Figure



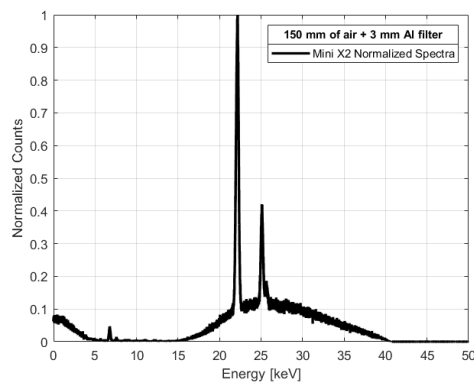
Target	Silver (Ag)
Target thickness	0.75 μm ($\pm 0.1 \mu\text{m}$)
Tube voltage	10 to 50 kV
Tube Current	5 to 200 μA
Approximate flux rates	10^6 counts per second/ mm^2 at a distance of 30 cm on axis, 50 kV and 1 μA
Output Cone Angle	120°

Figure 4.16: Amptek Mini-X2 X-ray tube and a table containing its specifications. Source: [58].

4.17a. Incidentally, we also recorded the spectra through a calibrated real-time digital pulse processing X-Ray Spectrometer. The *nanoXRS* is an x-ray spectrometer, with an integrated thermo-electrically cooled Silicon Drift Detector (SDD), manufactured by labZY².



(a) Voltage 50 kV. Both in linear and log scale. Source: [58].



(b) Voltage 40 kV. Linear scale. Propagation through 150 mm of air and 3 mm of aluminium.

Figure 4.17: Emission spectrum from the Amptek Mini-X2 X-ray tube.

In conventional DM, absorption filters are installed to eliminate soft x-rays. In fact, these are just absorbed by human skin and do not improve imaging, while increasing absorbed dose (Paragraph 2.1). Figure 4.17b displays the experimentally recorded spectra, showing a cut in counts below 15 keV due to the presence of a 3 mm aluminium filter. During the initial stages of development and de-

²The full *nanoXRS* Data Sheet is available at Yantel: <https://www.yantel.com/products/nanoxrs/>.

4.5. ASSEMBLY OF THE EXPERIMENTAL SETUP

sign, this spectrum was measured to evaluate the impact of absorption filters. However, as the main objective of this research is to provide a monochromator as an alternative to conventional absorption filters, the latter will no longer be part of the setup.

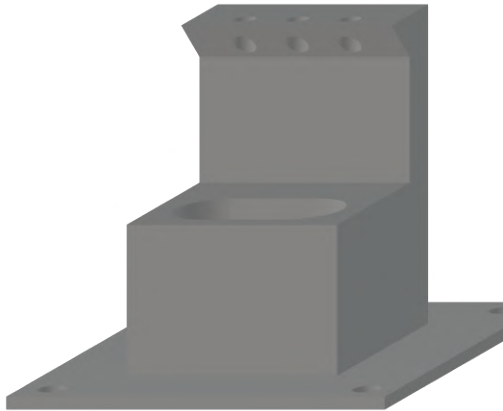
4.5.2 SUPPORTS AND HOLDERS

Several components of the setup have been custom-designed and manufactured to meet specific requirements. SolidWorks has been utilized to tailor and model these components.

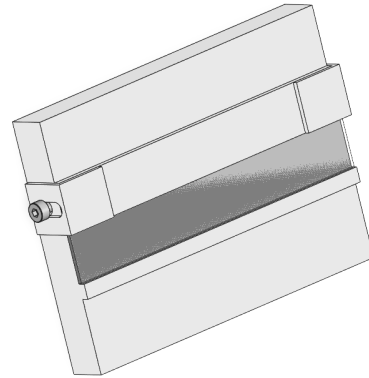
In DTU Skylab 3D Printing Workshop, 3D printers such as Prusa and UltiMaker models were employed, depending on their availability and suitability for the specific components. This allowed for the precise and accurate fabrication of the custom-designed elements via 3D printing. Examples of these models are reported in Figure 4.18.

To achieve vertical alignment and adjust the beam path on a vertical (z) scale, plastic spacers with a thickness of 0.5mm and the same footprint as the base of the supported parts were prepared. These spacers were designed to be easily added or removed as needed, simplifying vertical alignment.

In addition to the 3D-printed elements, solid metal components and brackets produced by Thorlabs were utilized in the setup, together with hexagonal screws, bolts and nuts, thus ensuring stability and precise positioning.



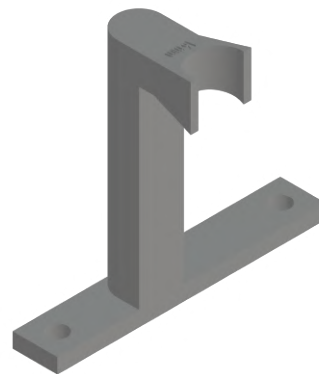
(a) Detector holder specifically designed with a test-tube accommodation cavity.



(b) Mirror installed and securely fixed in its dedicated 3D-printed holder. All parts within the assembly, except for the mirror and bolts, are 3D-printed.



(c) Vertical elevator for slit placement, with an optional slot for an aluminum sheet filter.



(d) Vertical pole with a retention mechanism (clamp) designed to securely hold the sample test-tube. It is intended to be screwed onto the left side of the detector holder.

Figure 4.18: Tailor-made and 3D-printed CAD models designed in SolidWorks.

5

Results and Discussions

In this chapter, we present the outcomes of the experimental phase, focusing on the validation of the proposed prototype for mammography application. The main objective is to assess the performance of the x-ray mirror by measuring its reflectivity and FWHM.

Furthermore, we compare poly-chromatic and mono-chromatic mammograms, evaluating their image quality in terms of Contrast to Noise Ratio and Signal to Noise Ratio. We also analyze the effective dose and simulated Mean Glandular Dose for both spectra to determine the radiation dose reduction achieved by the monochromatic spectrum.

The chapter begins with the alignment and calibration of the validation setup, introduced in the previous chapter.

5.1 EXPERIMENTAL SETUP CALIBRATION

As previously stated a laser guide was used to align all the components of the setup along the Z-axis, given the axis system from Figure 4.15b. The same laser has been used to align main components such as the x-ray tube exit hole with the two slits fissures and the center of the detector pixel matrix along the X- and Y-axes. In the case of the detector, its movement was precisely tuned using the translation stage actuator. On the other hand, for the remaining components

5.1. EXPERIMENTAL SETUP CALIBRATION

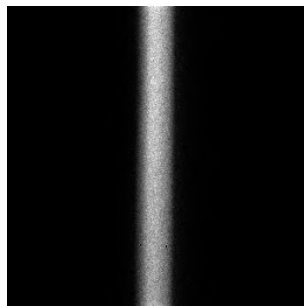
of the setup, manual adjustments were made using screws and bolts, allowing precise and fine adjustments to their position.

5.1.1 CHARACTERIZATION OF BEAM DIVERGENCE

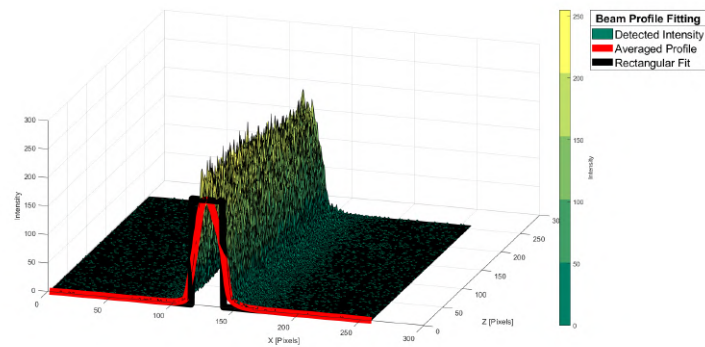
When the optical module (mirror) is retracted and not obstructing the beam-path, the direct beam on the detector is captured as shown in Figure 5.1a. The distance between the detector and the exit of the second slit is 465 mm. Despite both the slits being designed with 0.2 mm fissures in the X-direction, the image reveals the presence of beam divergence.

In terms of beam terminology, and referencing the axis system from Figure 4.15b, the following conventions are utilized:

- **Beam-path:** Refers to the optical path through which the x-ray beam propagates.
- **Beam-width or Beam-waist:** The dimension of the x-ray beam along the transversal Y-axis.
- **Beam-height:** The dimension of the x-ray beam along the vertical Z-axis.
- **Beam-footprint:** The projection of the beam-width on a surface, such as the mirror or detector plate.



(a) Intensity map of a 10s direct beam projection.



(b) Fitting of average intensity profile with a rectangle function.

Figure 5.1: Beam footprint on the probe detector positioned at 465 mm from the exit of the second slit, beam incidence normal to detector surface.

To better estimate the divergence, the averaged beam profile can be extracted and studied, as shown in Figure 5.1b. By utilizing the FWHM criteria to shape the beam-footprint, and considering that the image is composed of 256×256 pixels, with the detector pixel size being $55 \mu\text{m}$, the beam-width on the detector is calculated to be 0.66 mm. This value is more than three times the width of the

beam exiting the last slit. The half-angle divergence can be determined, from the beam-width on detector, using the following formula:

$$\theta_{div} = \tan^{-1} \left(\frac{0.66\text{mm}}{2 \cdot 465\text{mm}} \right) = 0.041^\circ$$

It is important to note that this simple formula for the half-divergence angle provides an overestimate of the actual divergence since it assumes a point source. In reality, the source has a well-defined beam-waist of 0.2 mm, and the Gaussian-beam formula should be employed for a more accurate estimate [62]. However, the overestimation of the angle divergence serves its purpose in providing an upper limit, which is essential for ensuring that the reflected beam remains unaffected by the direct beam divergence. By comparing the three reflection angles from the three manufactured mirrors and confirming that each angle α_i is greater than the calculated half-divergence angle θ_{div} , it is ensured that the reflected beam remains unobstructed and does not overlap with the direct beam divergence.

5.1.2 MIRROR ALIGNMENT PROCEDURE

Based on the direct beam footprint analysis, several considerations can be made regarding the calibration and alignment of the optical module, which is now positioned in the middle of the beam-path.

For instance, considering the distance between the beam slit exit and the center of the mirror (mid-point) to be 50 mm, a perfect alignment would result in a beam-width of 0.235 mm at the mirror mid-point, while its foot-print (projection on the mirror surface) would be 26.14 mm. The perfect alignment is presented in Figure 5.2, where the incidence angle is 0.516° , satisfying the condition for the First Bragg peak in the mirror with ID: *ds0307* (as shown in Figure 4.10 left).

Two critical conditions must be met to prevent the escape of the direct beam or flux losses when dealing with reflection from the mirrors:

1. The total length of the mirror (70 mm) must be greater than the beam footprint (26.14 mm) on the mirror's surface.
2. The grazing angle of incidence, which is specific for each mirror design and ranges from 0.246° to 0.516° , must be greater than the overshooting angle (0.19°).

5.1. EXPERIMENTAL SETUP CALIBRATION

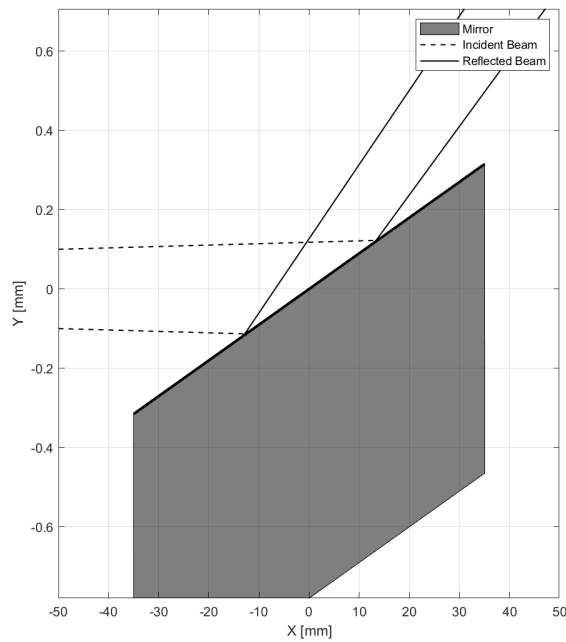


Figure 5.2: Graphical representation of the beam reflected by the mirror. The beam footprint on the mirror is shifted because of mis-alignment, and beam divergence is present. The grazing angle is 0.516° .

To understand the concept of the overshooting angle, Figure 5.3 is examined. This figure represents the zero position where the grazing angle is zero, and

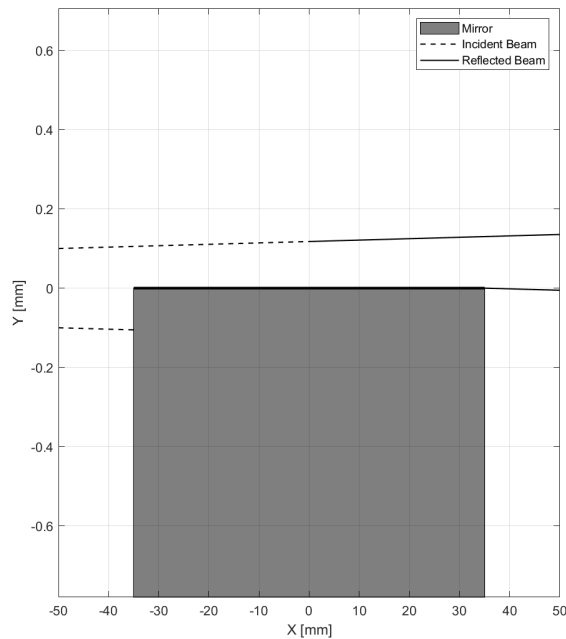


Figure 5.3: Graphical representation of the alignment process whereas half of the beam is stopped by the Mirror.

the mirror is perfectly aligned in the center of the beam-width. As the mirror is rotated around the vertical axis, it progressively covers more of the beam path. When the overshooting angle is reached, the beam footprint on the mirror's surface becomes equal to the length of the mirror itself. For grazing angles larger than the overshooting angle, the beam footprint on the mirror's surface shrinks until it becomes precisely equal to the beam-width for an incidence angle of 90° . The overshooting angle can be calculated as:

$$\theta_{over} = \sin^{-1} \left(\frac{0.235 \text{ mm}}{70 \text{ mm}} \right) = 0.19^\circ$$

To achieve the alignment depicted in Figures 5.2 and 5.3, precise adjustments of the mirror mid-point position on the Y-axis and its angular orientation (around the Z-axis) are necessary. The alignment process involves using the Thorlabs actuators, both the translation and the rotational stages.

With the x-ray source turned on, the rotational stage is set to the zero position (45° due to how the stage has been mounted), and the detector is aligned using the direct beam. Photons flux is then recorded while the mirror is moved from a retracted position forward into the beam-path. This calibration process is visualized in Figure 5.4a, where the horizontal axis represents the position along the Y-axis from the actuator minimum (0 mm, left-end of the rail) to the maximum extension (300 mm, right-end of the rail).

Initially, the photon flux remains unperturbed, as the mirror is not intercepting the beam. However, at a certain distance, the mirror side starts to absorb the beam, creating a shadow on the detector and causing a decrease in flux. As the mirror is further moved, it eventually completely intercepts the beam, leading to a flux reduction to zero. The resulting curve is expected to resemble a complementary error function (*erfc*), translated with its maximum at the beginning, minimum at zero, and centered around the mirror mid-point. This behavior can be effectively described using an equation of the form:

$$\Phi(y) = a \cdot \text{erfc}(y - b) + c$$

Where y represents the position along the Y-axis in [mm], and a , b , and c are fitting parameters. To ensure that the mirror is precisely at the center of the direct beam, the target is to register half the maximum flux during the calibration

5.1. EXPERIMENTAL SETUP CALIBRATION

along the Y-axis. This is done by fitting the data with this complementary error function, as shown in Figure 5.4a.

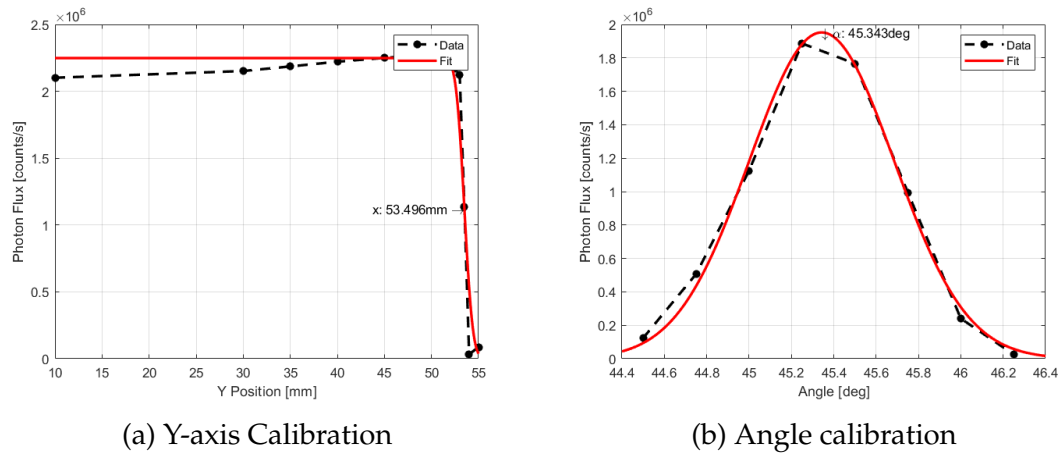


Figure 5.4: The setup calibration curves for mirror alignment.

After completing the Y-axis calibration, the next step is to record the Rocking curve, which represents the flux as a function of the angular position (angle of incidence) in a close interval around the zero position. The stage logical controller only provides positive values from 0 to 360 degrees with a precision of 0.001 degree. Due to the way the stage has been mounted, the zero position, where the mirror is parallel to the beam-path, corresponds to a 45-degree angle on the controller.

During the Rocking curve measurement, the flux curve should exhibit a triangular profile. Initially, a part of the beam is covered by one of the mirror edges, leading to a reduction in flux. As the mirror is gradually rotated, more flux is allowed until the opposite mirror edge starts to shadow the beam.

Deviation from the ideal triangular profile can provide valuable information about the alignment. If a plateau is present at the top of the Rocking curve, it indicates that the mirror mid-point is not precisely at the center of the beam, allowing more than half of the beam to pass through. This effect is analogous to a “backlash effect” in mechanical engineering, leading to a plateau on the recorded curve. Conversely, when after the Y-axis calibration, the mirror blocks more than half the flux, the apex of the triangular curve becomes sharper, but the height of the triangle (difference between peak and zero level) is not as wide as it should be.

For fitting of the Rocking curve, a Gaussian distribution is preferred over a triangle function for several reasons. Firstly, the instrumental broadening, represented by the apparatus function, includes contributions from all optical elements affecting the beam before it impinges on the sample. Secondly, the broadening resulting from coating defects also influences the curve's shape [63]. The result of the Rocking curve analysis is shown in Figure 5.4b, providing the precise angle for orientation alignment of the optical module.

The calibration and alignment process is iterative. The information obtained from fitting each individual parameter's curve during the process is used to identify its optimal point. Once determined, the setup is fixed at that position, and further adjustments were made to align the other parameter accordingly. For example, the process begins with the Y-axis calibration, followed by the angle calibration, where the presence of a plateau in the Rocking curve is noted.

This indicates that the mirror mid-point is not perfectly at the center of the beam. To address the plateau issue, the calibration process returns to the Y-axis calibration to fine-tune the mirror's position along the Y-axis. Once adjustments are made, the angle calibration is performed again. This iterative loop can be repeated multiple times until no significant changes in the registered flux are observed. In this study, two iterations were sufficient to achieve satisfactory results, as evidenced by the recorded curves in Figure 5.4. These final curves represent the end point of the calibration process and demonstrate that the alignment is now stable and accurate. The setup was adjusted to match the values obtained from data fitting, specifically 53.496 mm and 45.343° , which resulted in approximately half the flux being achieved.

5.1.3 REFLECTIVITY CURVE FROM MIRROR

In Figure 5.5a, multiple spectra were recorded by varying the grazing angle during the calibration process. By integrating the photon counts in the 19.09-22.01 keV energy range for each spectrum and dividing these values by the integration performed on the direct beam spectrum, the reflectance at 22 keV from the mirror can be calculated, enabling XRR analysis.

The obtained reflectivity curve is then compared in Figure 5.5b with the theoretical one obtained from the simulation (black curve in Figure 4.10 on the left). The calibration process should ideally start close to 50%, indicating that only

5.1. EXPERIMENTAL SETUP CALIBRATION

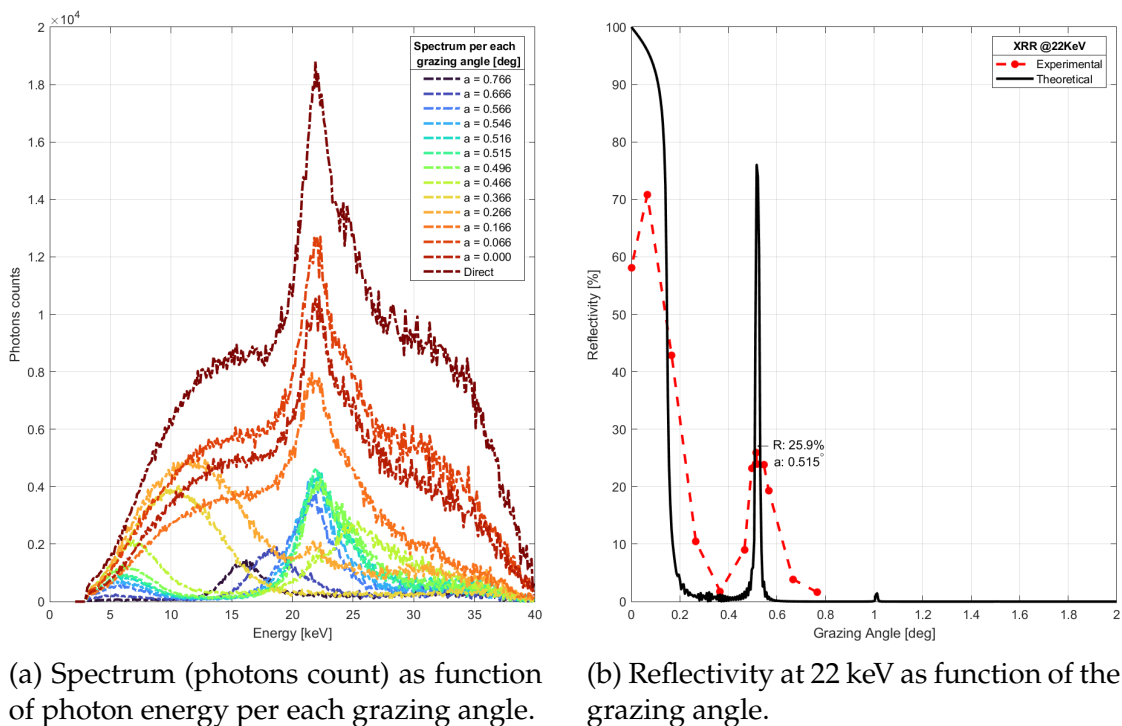


Figure 5.5: Precise calibration of mirror *ds0307* via comparison of the experimental XRR measurements with the theoretical one from Figure 4.10

half of the beam is transmitted at a zero grazing angle. However, the recorded value was 58%, slightly higher than the expected value. The reason for this discrepancy is that during calibration, all photons above 15 keV up to 40 keV were included in the integration. This broad energy range allowed some very energetic photons to be transmitted through the mirror, especially at large grazing angles where the beam-path encounters only one edge of the mirror or when the total thickness of the absorbing material (3 mm of PLA and 0.78 mm of Silicon substrate) allows for some high-energy photons to pass through. This can lead to a disguised reflectivity value, as it does not accurately represent the statistics of the flux at 22 keV alone.

In summary, the calibration process was precise as the Bragg peak position closely matched its expected grazing angle of 0.515° , very close to the theoretical value of 0.516° . However, the inclusion of high-energy photons during calibration had a negative impact on the process, leading to a recorded reflectivity value at the first Bragg peak of only 25.9%, significantly lower than the theoretical simulation value of 78%.

To obtain more accurate results, it is crucial to focus solely on the specific energy

range of interest (in this case, 22 keV) and carefully exclude high-energy photons from the calibration procedure.

For further insights and detailed explanations, refer to Paragraph 5.2.

5.2 MONOCHROMATOR PERFORMANCES

In addition to the medical application, a significant result of this work is the successful construction of a monochromator, the performance of which has not been previously discussed.

Figure 5.6 displays the overlapped spectra from a 10-second exposure of the detector to both the direct beam and the monochromatic beam. The second spectrum also includes the FWHM. The measurements were conducted without the bio-sample or the test tube to focus exclusively on the mirror performances.

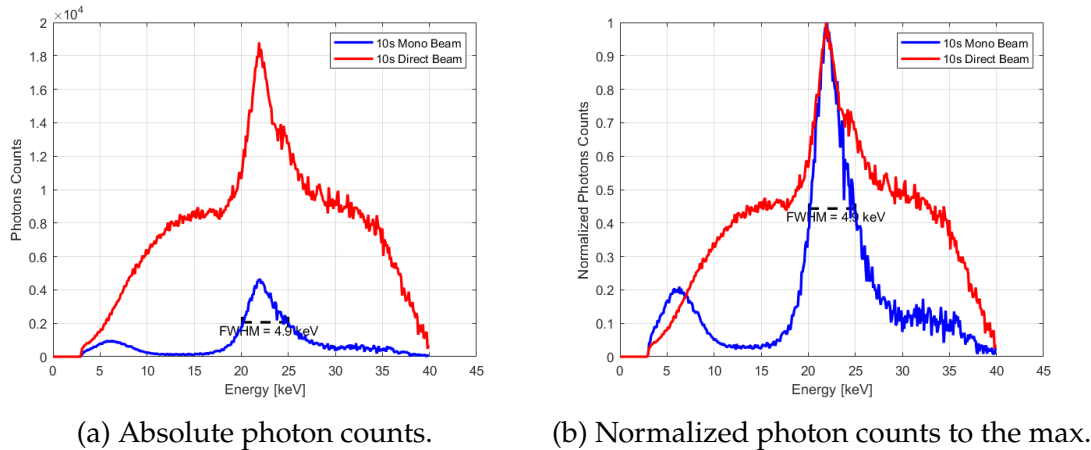


Figure 5.6: Comparison between 10 seconds exposure of direct and monochromated beam spectra with FWHM of the last shown.

The two spectra belong to two distinct beams that we categorize as follows:

- **Direct beam:** This refers to the X-ray beam that travels without any interaction with the optical module. In this case, the optical module is removed from the path, and the X-rays travel directly from the second slit to the detector surface.
- **Monochromatic beam:** This is the beam reflected at a specific angle (0.516°) after alignment of the optical module. This process enhances the reflectivity of the 22 keV emission line, resulting in a monochromatic X-ray beam.

5.2. MONOCHROMATOR PERFORMANCES

Both spectra are presented in two ways: first, in terms of absolute photon counts, and second, normalized by the maximum value. This allows for a closer comparison between the two.

By integrating the spectrum in the range of 21 to 23 keV, the calculated reflectivity is found to be 24.16% and the FWHM 4.9 keV. This suggests that, under the assumption of linearity, with sufficient integration time (40.1 seconds), the monochromatic spectrum will closely approach the number of photon counts (flux) of the direct beam, as shown in Figure 5.7.

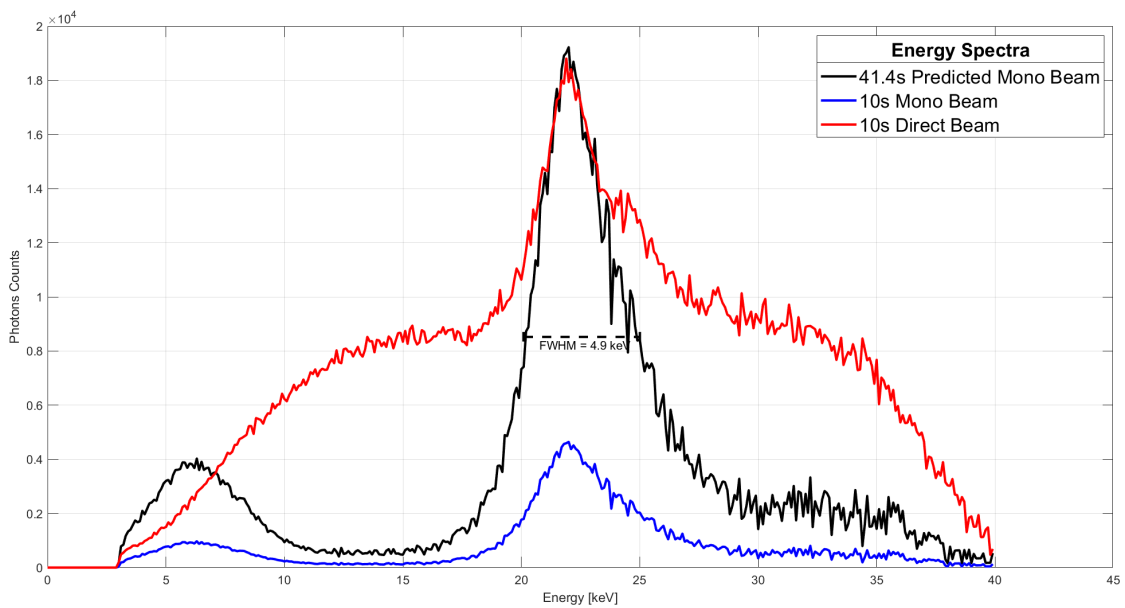


Figure 5.7: Predicted spectrum of the monochromatic beam in the integration time is 40.1 second over-plotted the measured spectra.

Incidentally, linear proportionality is an assumption as it can be achieved only if the flux is constant and the detector physical limit are respected, i.e. pixel dead-time after an event and saturation. Even if true linearity cannot be realistically achieved, we can reasonably assume so, as demonstrated by Figure 5.8.

In the Figure, the direct spectra recorded for three different integration intervals are shown. The main point is to showcase the linearity. For instance, at 22 keV, the 10-second integration yields 180,000 counts, the 5-second integration provides around 80,000 counts (close to the expected half, approximately 90,000 counts), and the 1-second spectrum results in 19,000 counts (close to the expected one-tenth, around 18,000 counts).

On the right-hand side of the graph, the normalization of the three spectra demonstrates that regardless of the integration time, the recorded spectrum remains consistent. However, the 1-second integration shows more apparent "ripples" due to lower absolute photon counts, affecting the overall statistics.

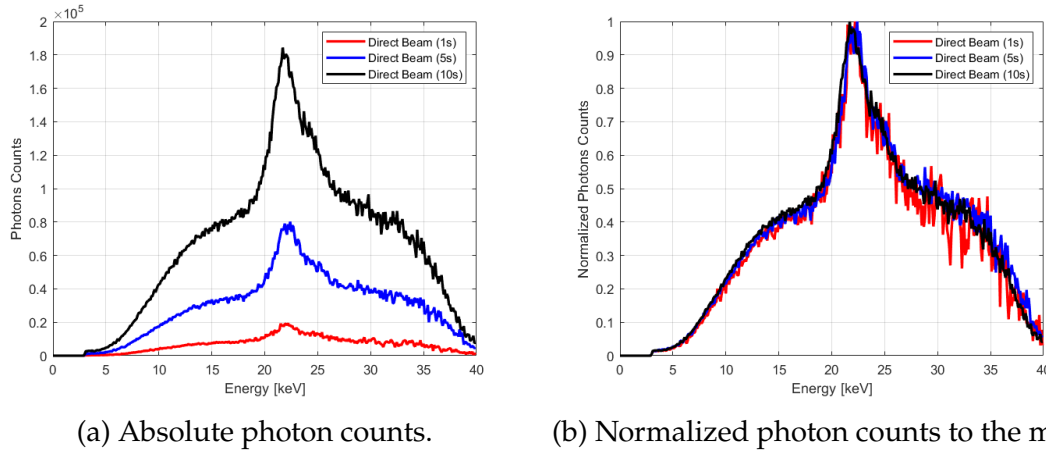


Figure 5.8: Comparison between direct beam spectra to show proportionality between integration time and photon counts.

5.2.1 INTERPRETATION OF RESULTS

It is essential to investigate why the maximum reflectance is only 25.9% at 22 keV, significantly lower than the theoretical maximum of 78%. To gain insights, we carefully analyze the footprints related to the spectra obtained from both the direct and reflected (monochromatic) beams, which are reported Figure 5.9. Obtaining the direct spectrum is straightforward, but the monochromatic one requires precise calibration along the Y-axis and accurate alignment of the mirror to achieve the correct angle.

Both the right and central images represent the monochromatic beam, with the monochromatic spectrum derived from the rightmost image. In the central image, it is evident that a portion of the direct beam is escaping, particularly in the Z-direction. Despite the mirror height being only 10 mm, the footprint appears taller, covering the entire 14 mm detector height. The vertical alignment of the mirror is not perfect. The Z-calibration process relied solely on the use of a laser and the manual addition of 0.5 mm spacers. As a result, the mirror is positioned approximately 1 mm below the ideal alignment.

5.2. MONOCHROMATOR PERFORMANCES

The beam width was rigidly constrained, using a 0.2 mm slit size to ensure the foot-beam remains on target (0.63 mm at 0.516°) even in cases of non-precise alignment and to mitigate the overshadowing of the radiogram by angular divergence in the Y-axis. In contrast, the constraints on the beam height were more relaxed, and both slits have a 10 mm vertical aperture. Due to the taller footprint of the direct beam compared to the reflected beam, the reflectance is decreased.

Additionally, it is noticeable that the mirror is not perfectly flat on the support holder, causing the reflected beam to be slightly tilted (approximately $\approx 2.24^\circ$). Although this tilting does not affect the working principle of reflectance through constructive interference by Bragg peaks, part of the reflected beam is deflected upward, and its exact quantification is not possible.

In conclusion, these factors, combined with other considerations mentioned earlier, such as imperfections in the alignment process, offer an explanation for the observed discrepancy in the measured reflectivity.

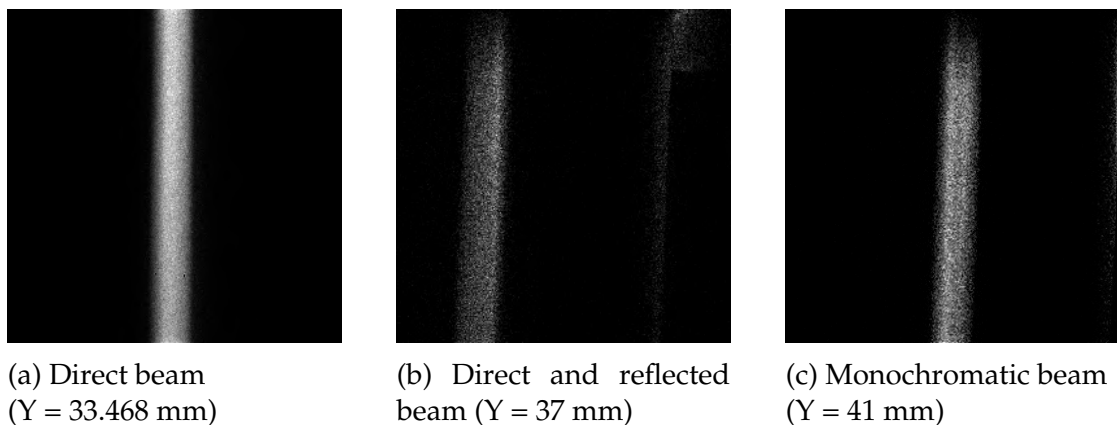


Figure 5.9: 10 second exposure radiograms of the beam with the detector moving in different positions along the Y-axis.

5.3 MAMMOGRAMS

Following the characterization of the monochromator's performance, we proceeded to introduce the bio-sample as described in Paragraph 4.4.2 and obtained radiograms (mammograms) of it. In this section, we present the final mammograms, which have been corrected using the FFC technique, obtained with a 10-second exposure to both the direct beam (Figure 5.10a) and the reflected monochromatic beam (Figure 5.10b).

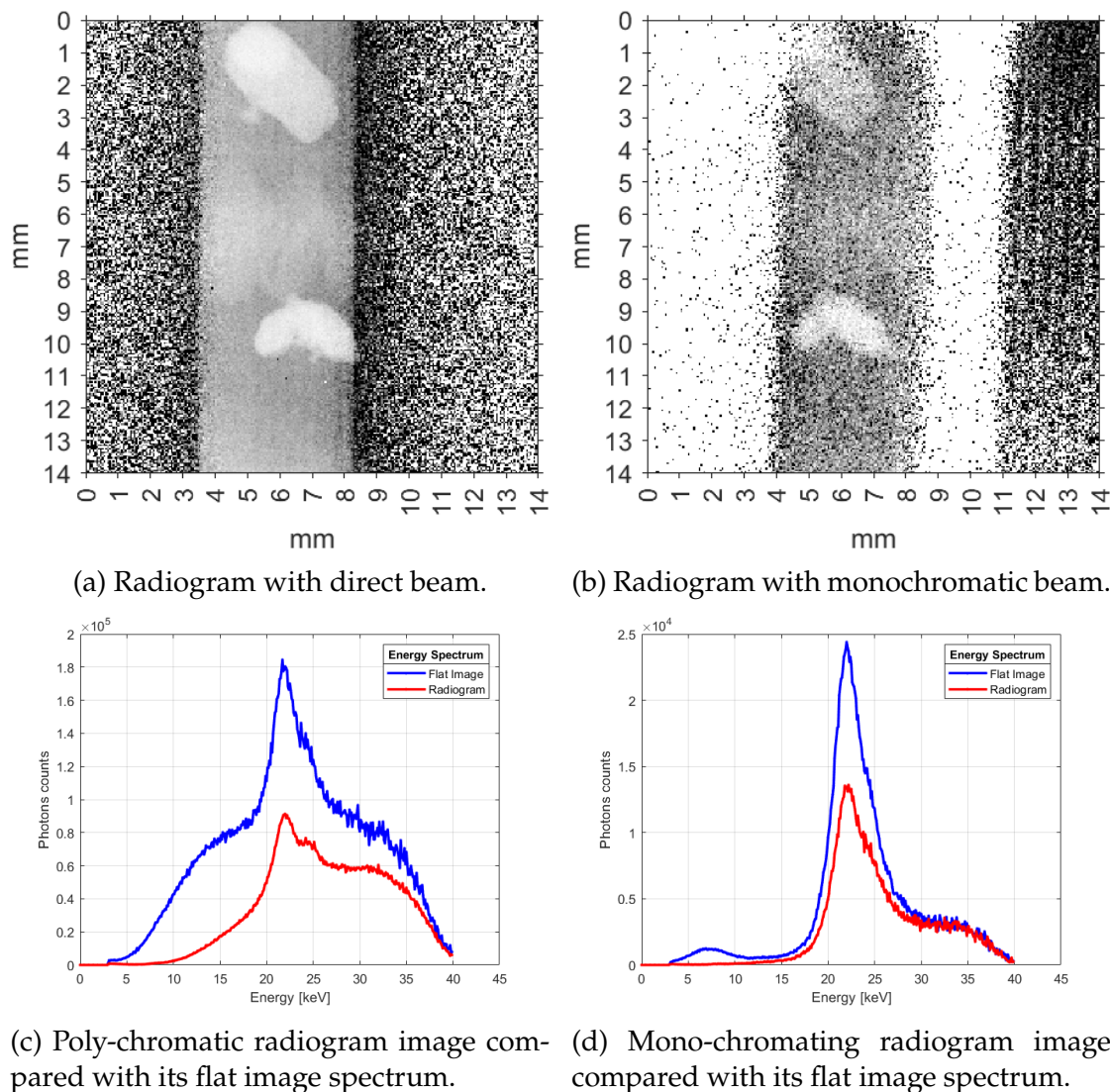


Figure 5.10: Comparison of the acquired radiogram mosaicking the 10 seconds projections of the bio-sample.

Incidentally, on the right side of Figure 5.10b, a very low flux direct beam is

5.3. MAMMOGRAMS

visible. Its origin was explained in the previous paragraph. Regardless, it was removed during the spectral analysis.

In Paragraph 2.1.3, we introduced the concept of projection, flat, and dark images. When applying FFC, the collected mammogram becomes a negative image, with brighter parts representing higher absorption.

The view of an inverted image (black on white), has proven to enhance human contrast perception, which in turn can increase the diagnostic accuracy of radiography imaging. Therefore, in Figure 5.10, we decided to present the negative of the collected absorption image, which will be shown in Figure 5.12.

The presence of noisy background in Figure 5.10 is not caused by fluctuations or readout noise in the detector (as dark images have been subtracted). Instead, it results from statistical noise caused by scattered photons. Since FFC relies on pixel-by-pixel division, an absolute white value ($+\infty$) is obtained when the flat image has no detection (division by zero). Even a division by 1 (one photon count) results in the pixel being closer to black rather than white.

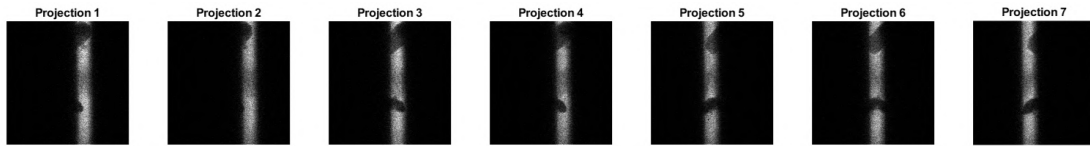
As predicted in Section 2.1.2, the spectral analysis confirm our expectations. Figure 5.10c clearly shows that below 10 keV, the photons are entirely absorbed and do not contribute to the image. Conversely, above 30 keV, absorption is minimal, leading to a deterioration of image contrast. At 22 keV, approximately half of the flux is absorbed.

5.3.1 PROJECTIONS

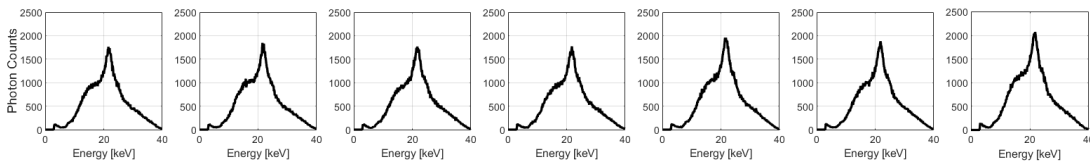
As determined from Figure 5.1a, the beam footprint on the detector measures 0.66 mm. Consequently, in order to capture an image of a few millimeters wide sample, consecutive projections are required. To ensure full imaging coverage without any blind (dark) spot, the projections must be at most 0.66 mm apart. However, to ensure image consistency and a reliable reconstruction, an interval of 0.5 mm was chosen.

To fully image the sample with an approximate width of 3.5 mm, a total of seven projections are required. These projections are obtained by keeping the beam fixed and moving the detector to different positions along the Y-axis. The direct mammogram projections, representing absorption, are shown in Figure 5.11. In these projections, brighter areas correspond to higher flux recorded. Addition-

ally, the corresponding absorption spectra (Q.E. not applied) for each projection are also presented.



(a) Seven projection 0.5 mm apart from each other.



(b) Energy spectrum of each projection.

Figure 5.11: Projection from the 10 seconds direct beam imaging of the bio-sample.

To generate the final mammograms depicted in Figure 5.10, it is essential to mosaic together the individual projections. However, during the process of adding the projections, brighter zones may appear due to the partial overlapping of two consecutive beam footprints. To address this issue and restore uniformity, a flat field correction is applied using Equation (2.3), resulting in the uniform image shown in Figure 5.12.

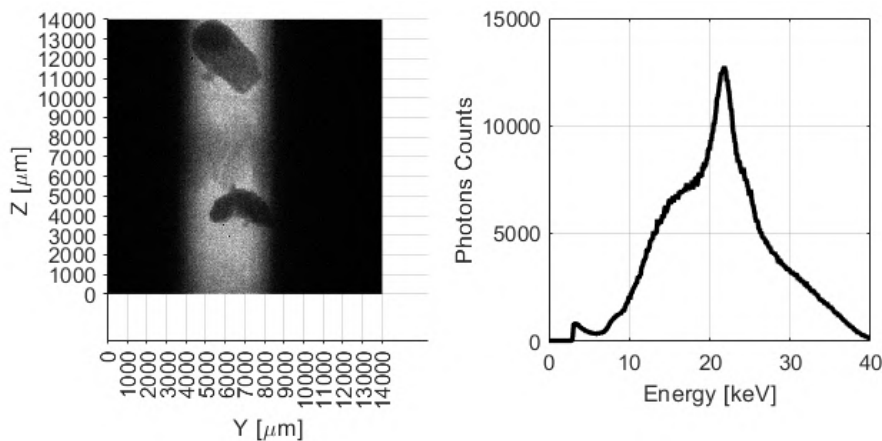


Figure 5.12: Mosaic of all the projections from Figure 5.11. Left: raw absorption radiogram of 10 second direct beam exposure. Right: related absorption spectra without quantum efficiency applied.

5.3.2 REGIONS OF INTEREST

As mentioned in Paragraph 2.3.3, in order to calculate image quality metrics, Regions of Interest (ROIs) are required. In Figure 5.13, the signal and background ROIs are depicted for both mammograms.

The ROIs are rectangular in shape and vary in size. This flexibility allows for selecting a smaller ROI to focus on the signal (calcifications) and a larger one for the background, ensuring a significant number of pixels to calculate the mean and standard deviations. Care was taken to draw the ROIs away from the edges to avoid contamination from surrounding areas. From the ROIs, using Equation (2.9), the CNR and SNR are computed.

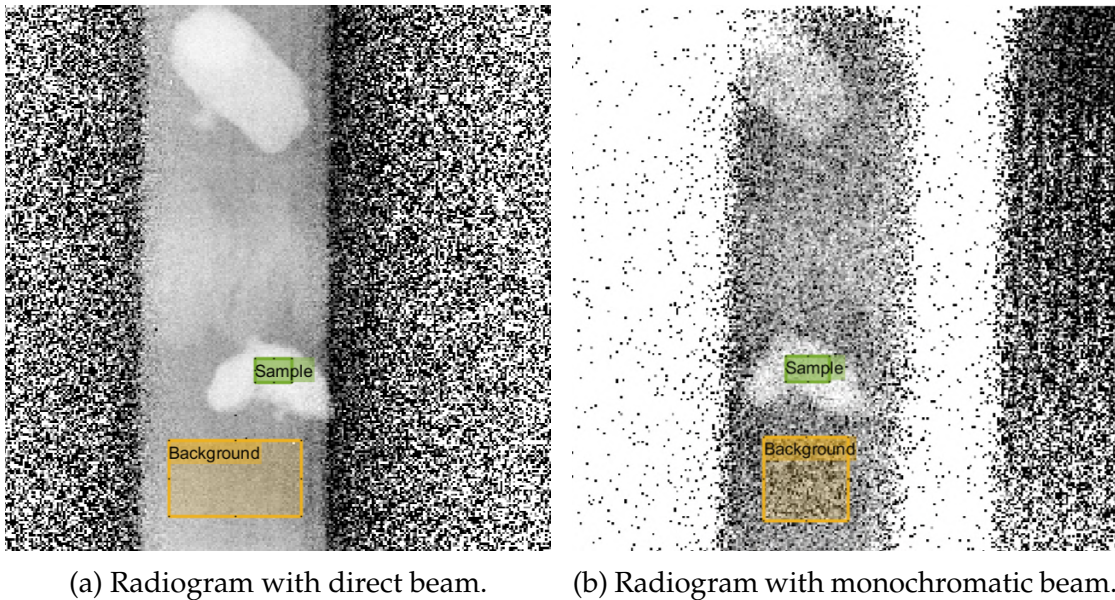


Figure 5.13: Region of interest on the acquired radiogram mosaicking for data analysis.

In order to evaluate the effective dose, we refer to Eq. (2.6). Since our study involves only one type of radiation (photons) and one type of tissue (breast), the summation in the equation is over a single term, and the product $w_R \cdot w_T$ is replaced with 0.12.

Next, we proceed to calculate the absorbed dose D , as defined by Equation (2.5). To determine the number of absorbed photons and their specific energy, we subtract the radiogram spectrum from its corresponding flat spectrum, allowing us to compute the mean energy imparted, denoted by dE .

The mass of the bio-sample was measured to be $m_0 = 3$ grams, but it is important to note that the irradiated volume dV is significantly smaller than the entire sample volume V_0 . The irradiated volume is the product of the sample thickness and the beam size, shown in Figure 5.10a i.e. 4.5 mm \times 14 mm. Meanwhile, we determined the total sample dimensions from Figure 4.13 to be: 6 mm \times 6 mm \times 30 mm.

Assuming for simplicity homogeneity in the sample tissue, the irradiated mass is:

$$dm = m_0 \cdot dV/V_0$$

Finally, we determine the effective dose by utilizing the left-hand side of Equation (2.5). Given the emission (flat) spectrum, we can also evaluate the Mean Glandular Dose via Equation (2.7). The FOM is a straightforward ratio between these two key aspects: image quality and dosimetry.

5.3.3 POLY-CHROMATIC TO MONO-CHROMATIC COMPARISON

Figure 5.14 presents a comprehensive summary of the results obtained from the two images mentioned earlier. The histogram displays various key metrics, including the Contrast to Noise Ratio (CNR) introduced in Equation (2.9), the Signal to Noise Ratio (SNR) from Equation (2.8), the Mean Glandular Dose (MGD) based on Equation (2.7), the effective dose derived from Equation (2.6), and the Figure of Merit (FOM) calculated using Equation (2.10).

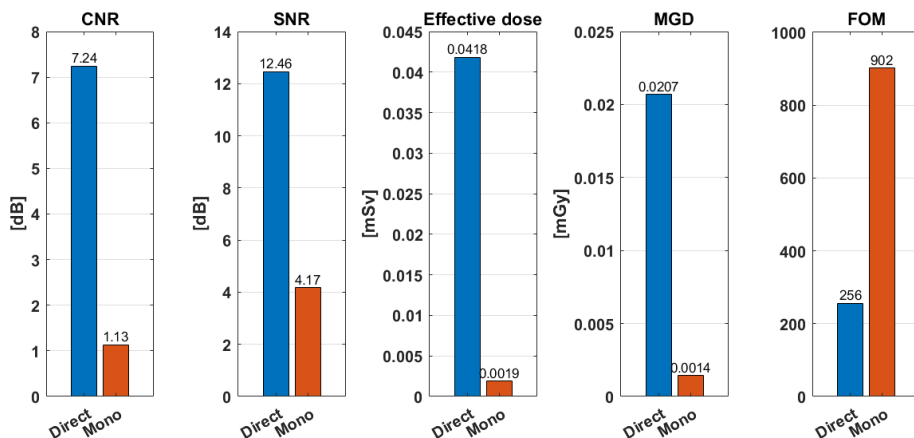


Figure 5.14: Comparison in terms of CNR, SNR, effective dose, MGD and FOM between two different radiograms. With a 10 second exposure of poly-chromatic (direct) or mono-chromatic (reflected) x-ray beams.

5.3. MAMMOGRAMS

Both mammograms are obtained by combining 7 projections, each captured with a 10-second exposure to the x-ray source. The "direct" radiogram is acquired with the optical module retracted, exposing the sample to the direct polychromatic beam. On the other hand, the "mono" radiogram is derived from the monochromatic beam after it has been reflected by the x-ray mirror.

Contrary to the expectations, the monochromatic spectrum does not improve image quality, rather the monochromatic image exhibits lower CNR and SNR, likely due to the lower flux. However, it also shows reduction in effective dose and MGD when simulated on a 50% glandular and 50% adipose 5 cm thick breast.

Upon calculating the FOM to compare the two, the monochromatic beam clearly provides better results. Ultimately, for an equal exposure time, the monochromatic beam does not improve image quality but significantly reduces the absorbed dose.

Despite the reduced contrast in the mammogram shown in Figure 5.10b, calcifications remain distinguishable by visual inspection. This confirms the substantial benefits that a monochromatic beam could bring to mammography applications.

In future studies, it would be interesting to investigate how varying the exposure time for both poly- and monochromatic spectra may enhance or reduce the FOM. It would be particularly valuable to compare the two when they exhibit the same flux at 22 keV rather than the same exposure time.

In conclusion, for the same exposure time, the monochromatic spectrum outperforms the polychromatic spectrum in terms of radiation dose reduction without a significant loss in image quality.



Conclusions

In this thesis, focusing on breast cancer screening using Digital Mammography (DM) techniques, we obtained mammograms from a custom-made bio-sample, thanks to an experimental imaging setup. The main goal was to explore the potential of reducing ionizing radiation exposure while improving image quality in x-ray medical screening procedures by implementing an optical module capable of collimating and mono-chromating x-ray spectra generated by an x-ray tube. The optical module was design using space technology transfer, in particular the Wolter type I mirrors' geometry and coating combinations found in past and operational space telescopes.

Throughout the project's development, several laboratories collaborated due to the complexity of creating a physical prototype involving manufacturing and assembly challenges.

Previous research indicated that monochromatic X-ray breast imaging could offer advantages such as lower dose and better image quality compared to conventional methods. This is due to the beam hardening effect, where low-energy X-rays are fully absorbed without contributing to the mammogram, while high-energy X-rays pass through the tissue with reduced image contrast. Therefore, an energy of 22 keV was chosen as the ideal monochromatic radiation, matching the optimal energy for breast imaging and the K-alpha emission line of Silver, which was the anode material of the selected x-ray tube model.

The final proposed optical module has a focal length of 270 cm. It comprises 58 concentric rings each constituted by a primary (hyperbolic) and secondary (parabolic) x-ray mirrors of 16 cm length. The outer ring has a mean radius of 15 cm while the inner one of 2.5 cm thus covering the entire average breast in one image. X-ray propagating close to the optical center can be blocked using an absorption filter. The rings are separated by a variable space between 1.4 and 3.5 mm in order to avoid shadowing. This optical module is no longer compatible for integration in conventional machines, where the source-to-detector distance is typically only 65 cm. Therefore we proposed to transition the mammography setup from a vertical orientation to a horizontal one.

The coating on each ring was a tailor-designed multi-layer engineered to improve reflectivity for the specific grazing angle of that shell. The multi-layer comprised 50 identical bi-layers made of Silicon and Tungsten, with Γ ratios ranging between 0.4 to 0.6 and thicknesses from 30 to 150 Å. The total projected area is 412.47 cm²; i.e. 60.02% of the geometric area. At 22 keV, the effective area peaks at 144.015 cm², which corresponds to 34.92% of the projected area. During the design, a roughness of 2.5 Å has been hypothesized. Prior to coating, using the Atomic Force Microscopy (AFM) technique, the actual surface topography and roughness has been determined to be ≈ 3.3 Å. Incidentally, we tried to clean the substrate with a specific process, however it didn't improve the surface roughness.

Rather than manufacturing the entire optical module, we opted to prototype three shells: one in the outer group, one in the middle, and one in the inner group. These prototypes consist of smaller, flat substrates coated with the specific ring recipe, and they were subsequently tested in a custom-built setup for imaging a phantom bio-sample. The coating of the substrates was achieved using the magnetron sputtering technique. After coating, we performed X-ray Reflectivity (XRR) to characterize the structure of the deposited coating. During the coating process, we encountered some challenges and drawbacks. Nonetheless, the XRR analysis via a more complex structure model indicated that the coating was still reasonably close to the desired outcome.

To validate the use of mono-chromating radiation for mammography applications, a bench system was developed at DTU Space. The experimental setup consisted of a Mini-X2 x-ray tube operated at 40 keV and 100 μ A, generating a Bremsstrahlung spectrum with an emission peak at 22 keV due to the Silver an-

ode. The setup included beam-shaping slits, high-resolution roto-translation stages with remote-controlled actuators, and 3D-printed mechanical supports. The bio-sample used in this study mimics the x-ray properties of real breast tissue in terms of Linear Absorption Coefficient (LAC). To simulate cancer calcifications, sodium chloride grains of compatible dimensions were added to the bio-sample. The detector, MiniPIX-TPX3, was an energy-sensitive Silicon detector with a spatial resolution of 55 microns and a quantum efficiency of approximately 20% at 22 keV. It was used to collect multiple projections of the bio-sample to compose the final mammograms using Flat Field Correction (FFC) techniques.

In the setup only the shell prototype having the largest grazing angle was tested. While the designed grazing angle was 0.531° , the as-coated mirror had it at 0.516° due to a non-perfect coating. The angular Full Width at Half Maximum (FWHM) of the peak was measured to be 0.1° against the simulated 0.02° . The experimentally measured reflectivity at 22 keV was only 25.9%, much lower than the simulated 76.03%. Potential alignment issues during the setup might explain these discrepancies. The monochromatic performances exhibited a FWHM of 4.9 keV.

Comparing the results, we found that under equal exposure times of 10 seconds, the monochromatic image had lower image quality in terms of Contrast to Noise Ratio (CNR) and Signal to Noise Ratio (SNR). Specifically, the CNR decreases from 7.24 dB to 1.13 dB. However, the effective dose and simulated Mean Glandular Dose (MGD) were significantly lower in the monochromatic image, by an order of magnitude. For instance, the effective dose decreases from 0.0418 mSv to 0.002 mSv. When considering the ratio between these two parameters, the monochromatic spectrum showed superior results.

Future studies may investigate varying the exposure time for both poly- and monochromatic spectra to enhance or reduce the Figure of Merit (FOM). Comparisons under the same flux at 22 keV, rather than the same exposure time, could be valuable. Additionally, a significant goal would be to fully manufacture the optical module. This poses certain challenges, particularly concerning the grazing angle for the Bragg peak of the as-coated substrate, which slightly deviates from the intended design angle. While this was not a concern during the validation phase, where the mirror could be freely rotated, in the final configuration, each component will be fixed.

This study introduced a space technology transfer for mammography application, specifically focusing on the design of an optical module for mono-chromating and collimating X-rays. In conclusion, the use of monochromatic spectrum proved to be superior to polychromatic spectrum in terms of reducing radiation dose without compromising image quality, especially for the same exposure time.

References

- [1] Hyuna Sung et al. “Global Cancer Statistics 2020: GLOBOCAN Estimates of Incidence and Mortality Worldwide for 36 Cancers in 185 Countries”. In: *CA: A Cancer Journal for Clinicians* 71.3 (2021), pp. 209–249. DOI: <https://doi.org/10.3322/caac.21660>. eprint: <https://acsjournals.onlinelibrary.wiley.com/doi/pdf/10.3322/caac.21660>. URL: <https://acsjournals.onlinelibrary.wiley.com/doi/abs/10.3322/caac.21660>.
- [2] Melina Arnold et al. “Current and future burden of breast cancer: Global statistics for 2020 and 2040”. In: *The Breast* 66 (2022), pp. 15–23.
- [3] Adrienne G. Waks and Eric P. Winer. “Breast Cancer Treatment: A Review”. In: *JAMA* 321.3 (Jan. 2019), pp. 288–300. ISSN: 0098-7484. DOI: [10.1001/jama.2018.19323](https://doi.org/10.1001/jama.2018.19323). eprint: https://jamanetwork.com/journals/jama/articlepdf/2721183/jama_waks_2019_rv_180011.pdf. URL: <https://doi.org/10.1001/jama.2018.19323>.
- [4] Mark A Helvie. “Digital mammography imaging: breast tomosynthesis and advanced applications”. In: *Radiologic Clinics* 48.5 (2010), pp. 917–929.
- [5] Ritse M. Mann, Nariya Cho, and Linda Moy. “Breast MRI: State of the Art”. In: *Radiology* 292.3 (2019). PMID: 31361209, pp. 520–536. DOI: [10.1148/radiol.2019182947](https://doi.org/10.1148/radiol.2019182947). eprint: <https://doi.org/10.1148/radiol.2019182947>. URL: <https://doi.org/10.1148/radiol.2019182947>.
- [6] Therese B Bevers et al. “Breast cancer screening and diagnosis”. In: *Journal of the National Comprehensive Cancer Network* 7.10 (2009), pp. 1060–1096.
- [7] Barcons X.; Barret Didier; Decourchelle A. *Athena (Advanced Telescope for High ENergy Astrophysics) Assessment Study Report for ESA Cosmic Vision*

REFERENCES

- 2015-2025. <https://www.cosmos.esa.int/documents/400752/400864/Athena+Mission+Proposal/18b4a058-5d43-4065-b135-7fe651307c46>.
- [8] *PIXet PRO*. URL: <https://www.advacam.com/products-software/software/pixet-pro/>. Advacam.
- [9] *Interactive Data Language (IDL)*. <https://www.harrisgeospatial.com/Software-Technology/IDL>. Accessed: June 3, 2023.
- [10] David L. Windt. “IMD—Software for modeling the optical properties of multilayer films”. In: *Computers in Physics* 12.4 (1998), pp. 360–370. DOI: [10.1063/1.168689](https://doi.org/10.1063/1.168689). eprint: <https://aip.scitation.org/doi/pdf/10.1063/1.168689>. URL: <https://aip.scitation.org/doi/abs/10.1063/1.168689>.
- [11] David Nečas and Petr Klapetek. In: *Open Physics* 10.1 (2012), pp. 181–188. DOI: [doi:10.2478/s11534-011-0096-2](https://doi.org/10.2478/s11534-011-0096-2). URL: <https://doi.org/10.2478/s11534-011-0096-2>.
- [12] Marie Planchard. *Engineering Design with SolidWorks 2017*. SDC Publications, 2017.
- [13] *Kinesis Software*. URL: https://www.thorlabs.com/navigation.cfm?guide_id=2319. Thorlabs.
- [14] Peter L. Henriksen et al. “Design, performance, and utilization of the Low-Energy X-ray Reflectometer at DTU space”. In: *Journal of Astronomical Telescopes, Instruments, and Systems* 7.4 (2021), p. 048004. DOI: [10.1117/1.JATIS.7.4.048004](https://doi.org/10.1117/1.JATIS.7.4.048004). URL: <https://doi.org/10.1117/1.JATIS.7.4.048004>.
- [15] Aline Cora Amanda Lier Møller. *FCXR (8.048 keV) X-ray laboratory*. Nov. 2021. URL: <https://www.space.dtu.dk/english/research/research-divisions/astrophysics-and-atmospheric-physics/high-energy-instrumentation/8-kev-laboratory>.
- [16] Douglas M. Tucker, Gary T. Barnes, and Xizeng Wu. “Molybdenum target x-ray spectra: A semiempirical model”. In: *Medical Physics* 18.3 (1991), pp. 402–407. DOI: <https://doi.org/10.1118/1.596686>. eprint: <https://aapm.onlinelibrary.wiley.com/doi/pdf/10.1118/1.596686>. URL: <https://aapm.onlinelibrary.wiley.com/doi/abs/10.1118/1.596686>.

- [17] Lee Rena Kim Gyehong. “Effect of Target Angle and Thickness on the Heel Effect and X-ray Intensity Characteristics for 70 kV X-ray Tube Target”. In: *pmp* 27.4 (2016), pp. 272–276. DOI: [10.14316/pmp.2016.27.4.272](https://doi.org/10.14316/pmp.2016.27.4.272). eprint: <http://www.e-sciencecentral.org/articles/?scid=1098563>. URL: <http://www.e-sciencecentral.org/articles/?scid=1098563>.
- [18] Madhava Bhat et al. “Diagnostic x-ray spectra: A comparison of spectra generated by different computational methods with a measured spectrum”. In: *Medical physics* 25 (Feb. 1998), pp. 114–20. DOI: [10.1118/1.598170](https://doi.org/10.1118/1.598170).
- [19] Ingvar Fife. “The physical dimensions of the compressed breast”. In: *The British journal of radiology* 64 (Feb. 1991), pp. 73–4. DOI: [10.1259/0007-1285-64-757-73](https://doi.org/10.1259/0007-1285-64-757-73).
- [20] S A Beaman and S C Lillicrap. “Optimum X-ray spectra for mammography”. In: *Physics in Medicine And Biology* 27.10 (Oct. 1982), p. 1209. DOI: [10.1088/0031-9155/27/10/001](https://doi.org/10.1088/0031-9155/27/10/001). URL: <https://dx.doi.org/10.1088/0031-9155/27/10/001>.
- [21] A. Gianoncelli et al. *Soft X-ray microscopy radiation damage on fixed cells investigated with Synchrotron Radiation Ftir Microscopy*. May 2015. URL: <https://www.nature.com/articles/srep10250>.
- [22] Ioannis Sechopoulos. “A review of breast tomosynthesis. Part I. The image acquisition process”. In: *Medical Physics* 40.1 (2013), p. 014301. DOI: <https://doi.org/10.1118/1.4770279>. eprint: <https://aapm.onlinelibrary.wiley.com/doi/pdf/10.1118/1.4770279>. URL: <https://aapm.onlinelibrary.wiley.com/doi/abs/10.1118/1.4770279>.
- [23] Pasquale Delogu et al. “Optimization of the energy for breast monochromatic absorption X-ray Computed Tomography”. In: *Scientific reports* 9.1 (2019), pp. 1–10.
- [24] Johannes G Korporaal et al. “Titanium contrast-enhanced mammography (TiCEM)”. In: *White paper. Erlangen: Siemens Healthineers* (2018).
- [25] David L. Windt. “Monochromatic mammography using scanning multi-layer X-ray mirrors”. In: *Review of Scientific Instruments* 89.8 (2018), p. 083702. DOI: [10.1063/1.5041799](https://doi.org/10.1063/1.5041799). eprint: <https://doi.org/10.1063/1.5041799>. URL: <https://doi.org/10.1063/1.5041799>.

REFERENCES

- [26] Kwon-Ha Yoon et al. "Monochromatic x-rays for low-dose digital mammography: preliminary results". In: *Investigative radiology* 47.12 (Dec. 2012), pp. 683–687. ISSN: 0020-9996. DOI: [10.1097/rli.0b013e31826badfb](https://doi.org/10.1097/rli.0b013e31826badfb). URL: <https://doi.org/10.1097/RLI.0b013e31826badfb>.
- [27] M J Berger and J H Hubbell. "XCOM: Photon cross sections on a personal computer". In: (July 1987). DOI: [10.2172/6016002](https://www.osti.gov/biblio/6016002). URL: <https://www.osti.gov/biblio/6016002>.
- [28] Vincent Van Nieuwenhove et al. "Dynamic intensity normalization using eigen flat fields in X-ray imaging". In: *Optics express* 23.21 (2015), pp. 27975–27989.
- [29] S. Massahi and D. Ferreira. In: *Proc. SPIE, Vol. 11822* (2021).
- [30] Finn Christensen et al. "Coatings for the NuSTAR mission". In: vol. 8147. Sept. 2011. DOI: [10.1117/12.894615](https://doi.org/10.1117/12.894615).
- [31] T. T. Järvi et al. "Enhanced sputtering from nanoparticles and thin films: Size effects". In: *Europhysics Letters* 82.2 (Mar. 2008), p. 26002. DOI: [10.1209/0295-5075/82/26002](https://dx.doi.org/10.1209/0295-5075/82/26002). URL: <https://dx.doi.org/10.1209/0295-5075/82/26002>.
- [32] Jack Valentin et al. *The 2007 recommendations of the international commission on radiological protection*. Vol. 37. 2-4. Elsevier Oxford, 2007.
- [33] Moayyad E Suleiman, Patrick C Brennan, and Mark F McEntee. "Mean glandular dose in digital mammography: a dose calculation method comparison". In: *Journal of Medical Imaging* 4.1 (2017), pp. 013502–013502.
- [34] John M Boone. "Normalized glandular dose (DgN) coefficients for arbitrary x-ray spectra in mammography: Computer-fit values of Monte Carlo derived data". In: *Medical physics* 29.5 (2002), pp. 869–875.
- [35] Elena Eggl et al. "Dose-compatible grating-based phase-contrast mammography on mastectomy specimens using a compact synchrotron source". In: *Scientific reports* 8.1 (2018), p. 15700.
- [36] H Buhr et al. "Measurement of the mass energy-absorption coefficient of air for x-rays in the range from 3 to 60 keV". In: *Physics in Medicine & Biology* 57.24 (2012), p. 8231.

- [37] Matts Björck. “Fitting with differential evolution: An introduction and evaluation”. In: *Journal of Applied Crystallography* 44 (Dec. 2011). DOI: [10.1107/S0021889811041446](https://doi.org/10.1107/S0021889811041446).
- [38] Craig B Markwardt. “Non-linear least squares fitting in IDL with MPFIT”. In: *arXiv preprint arXiv:0902.2850* (2009).
- [39] Jorge J Moré, Burton S Garbow, and Kenneth E Hillstrom. *User guide for MINPACK-1*. Tech. rep. CM-P00068642, 1980.
- [40] Desiree Della Monica Ferreira et al. “Design, development, and performance of x-ray mirror coatings for the ATHENA mission”. In: *Optics for EUV, X-Ray, and Gamma-Ray Astronomy VIII*. Ed. by Stephen L. O’Dell and Giovanni Pareschi. Vol. 10399. International Society for Optics and Photonics. SPIE, 2017, pp. 266–275. DOI: [10.1117/12.2273603](https://doi.org/10.1117/12.2273603). URL: <https://doi.org/10.1117/12.2273603>.
- [41] Hans Wolter. “Spiegelsysteme streifenden Einfalls als abbildende Optiken für Röntgenstrahlen”. In: *Annalen der Physik* 445.1-2 (1952), pp. 94–114. DOI: <https://doi.org/10.1002/andp.19524450108>. eprint: <https://onlinelibrary.wiley.com/doi/pdf/10.1002/andp.19524450108>. URL: <https://onlinelibrary.wiley.com/doi/abs/10.1002/andp.19524450108>.
- [42] Giovanni Pareschi, Daniele Spiga, and Carlo Pellicciari. “X-ray Telescopes Based on Wolter-I Optics”. In: *The WSPC Handbook of Astronomical Instrumentation*. Chap. Chapter 1, pp. 3–31. DOI: [10.1142/9789811203800_0001](https://doi.org/10.1142/9789811203800_0001). eprint: https://www.worldscientific.com/doi/pdf/10.1142/9789811203800_0001. URL: https://www.worldscientific.com/doi/abs/10.1142/9789811203800_0001.
- [43] Desiree Della Monica Ferreira. “Notes from the course 30787 offered at DTU space”. In: (Feb. 2022).
- [44] Jason Koglin et al. “NuSTAR hard x-ray optics design and performance”. In: vol. 7437. Aug. 2009. DOI: [10.1117/12.826724](https://doi.org/10.1117/12.826724).
- [45] UG Briel et al. “The ROSAT Users’ Handbook”. In: *MPE: Garching* (1994).
- [46] F. Jansen et al. “XMM-Newton observatory. I. The spacecraft and operations”. In: *AAP* 365 (Jan. 2001). DOI: [10.1051/0004-6361:20000036](https://doi.org/10.1051/0004-6361:20000036).

REFERENCES

- [47] Peter J. Serlemitsos et al. “The X-Ray Telescope onboard Suzaku”. In: *Publications of the Astronomical Society of Japan* 59.sp1 (Jan. 2007), S9–S21. ISSN: 0004-6264. DOI: [10.1093/pasj/59.sp1.S9](https://doi.org/10.1093/pasj/59.sp1.S9). eprint: <https://academic.oup.com/pasj/article-pdf/59/sp1/S9/17451519/pasj59-00S9.pdf>. URL: <https://doi.org/10.1093/pasj/59.sp1.S9>.
- [48] A. Merloni et al. “eROSITA Science Book: Mapping the Structure of the Energetic Universe”. In: (Sept. 2012).
- [49] XRISM Science Team. *XRISM Quick Reference*. 2022. DOI: [10.48550/ARXIV.2202.05399](https://doi.org/10.48550/ARXIV.2202.05399). URL: <https://arxiv.org/abs/2202.05399>.
- [50] *MRI of the Thorax | Radiology Key*. <https://radiologykey.com/mri-of-the-thorax/>. (Accessed on 07/29/2023).
- [51] Andrew J. Detor et al. “Stress and microstructure evolution in thick sputtered films”. In: *Acta Materialia* 57.7 (2009), pp. 2055–2065. ISSN: 1359-6454. DOI: <https://doi.org/10.1016/j.actamat.2008.12.042>. URL: <https://www.sciencedirect.com/science/article/pii/S135964540900010X>.
- [52] Finn Erland Christensen et al. “Coatings for the NuSTAR mission”. English. In: vol. 8147. 1. Optics for EUV, X-Ray, and Gamma-Ray Astronomy V ; Conference date: 23-08-2011 Through 25-08-2011. Society of Photo-Optical Instrumentation Engineers, 2011, 81470U–19. DOI: [10.1117/12.894615](https://doi.org/10.1117/12.894615). URL: http://spie.org/app/program/index.cfm?fuseaction=conferencedetail&conference_id=947528&event_id=894266.
- [53] *015-DS-120418.pdf*. <http://www.cirsinc.com/wp-content/uploads/2019/04/015-DS-120418.pdf>. (Accessed on 07/06/2023).
- [54] PL Arancibia Hernández et al. “Breast calcifications: description and classification according to bi-rads 5th edition”. In: *Rev. Chil. Radiol* 22 (2016), pp. 80–91.
- [55] Conor K McGarry et al. “Tissue mimicking materials for imaging and therapy phantoms: a review”. In: *Physics in Medicine & Biology* 65.23 (2020), 23TR01.
- [56] W Zhou and C MacDonald. “WE-E-L100J-04: Coherent Scatter Imaging for Mammography”. In: *Medical Physics* 34.6Part21 (June 2007), pp. 2606–2606. DOI: [10.1118/1.2761579](https://doi.org/10.1118/1.2761579). URL: <https://doi.org/10.1118%2F1.2761579>.

- [57] Robert Scott et al. "Elemental vs. phase composition of breast calcifications". In: *Scientific reports* 7.1 (2017), p. 136.
- [58] *Mini-X2 X-Ray Tube System for XRF – Amptek – X-Ray Detectors and Electronics*. <https://www.amptek.com/products/mini-x2-x-ray-tube>. (Accessed on 07/29/2023).
- [59] *300 mm Linear Translation Stage with Integrated Controller, Stepper Motor*. https://www.thorlabs.com/newgrouppage9.cfm?objectgroup_id=7652. (Accessed on 07/29/2023).
- [60] *Heavy-Duty Rotation Stage with Stepper Motor*. https://www.thorlabs.com/newgrouppage9.cfm?objectgroup_id=1064. (Accessed on 07/29/2023).
- [61] *ADVACAM MiniPIX TPX3 X-ray diffraction for Non-Destructive-Testing*. <https://advacam.com/camera/minipix-tpx3>. (Accessed on 07/29/2023).
- [62] Bahaa EA Saleh and Malvin Carl Teich. *Fundamentals of photonics*. John Wiley & sons, 2019.
- [63] Jun Ho Jang et al. "Structural characterization of strained silicon grown on a SiGe buffer layer". In: *Semiconductor Science and Technology* 23 (Feb. 2008), p. 035012. doi: [10.1088/0268-1242/23/3/035012](https://doi.org/10.1088/0268-1242/23/3/035012).

Acknowledgments

Maria Elena Valcher, Professor, University of Padova
Thesis Supervisor

Desiree Della Monica Ferreira, Senior Researcher, DTU Space
Thesis Supervisor

Irfan Kuvvetli, Senior Researcher, DTU Space
Thesis Supervisor

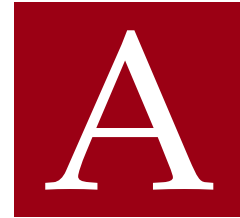
Sonny Massahi, Postdoc, DTU Space
Magnetron Sputtering Supervisor

Diego Paredes Sanz, PhD, DTU Space
Thesis Adviser

Jesper Hanberg, Head of Fabrication Support, DTU Nanolab
Authorizing Nanolab access

Berit Herstrøm, Process Specialist, DTU Nanolab
Atomic Force Microscopy Supervisor

Rajmund Mokso, Senior Researcher, DTU Physics
Providing support with the biological samples



Appendix

A.1 MATLAB

Different Matlab scripts are attached to this report:

- **VariableSpacingLength_v3.m** performs the geometry optimization, given some key input parameters such as SID (300cm), ODD (270cm), length of plate to be coated (16cm), inner and outer shell radiuses (2.5 and 15cm), structure spacing (0.1cm); it finds the optimal number of shells, their position (mean radius), it calculates different useful parameters such as projected area and grazing angles and save them in an external *.txt* file. Finally it plots a side-view and top-view of the design.
- **effective_area.m** reads the output files from IDL containing the effective area curves and prepares the beautiful graphs included in the report.
- **rate.m** given a material and the desired layer thickness, it computes the required ring speed to achieve it.
- **logbook_for_coatings_at_DTU.m** modified version of the code written by Dr. Sonny Massahi to visualize the sputtering chamber logbooks.
- **CNR_dose_v5.m** computes comparison metrics. It needs flat, projection, dark images and their spectra. It allows the user to draw ROIs.
- **qe.m** sub-routine to compute quantum efficiency given the silicon cross section and material thickness.
- **Spectra.m** visualizes for comparison different spectra on the graph.
- **processSpectra.m** sub-routine to compute FWHM given a spectrum.
- **allSpectra.m** generates an XRR curve given multiple spectra as input and compares it with simulated one.
- **collage.m** merges together different projections and their spectra.
- **divergence.m** computes beam divergence given the direct beam footprint image.
- **plot_fitting.m** plots the reflectivity curves from XRR analysis of the three

A.2. IDL

- coated substrates.
- **plot_reflectivity.m** plots the designed reflectivity at 22 keV and compares it with the simulated one from the as-coated substrate model.
- **alignment.m** visualizes and fits rocking curves for setup alignment.

A.2 IDL

Different IDL scripts are attached to this report:

- **V6.pro** optimizes thickness and Gamma of a bi-layer, shell by shell, given number of repetitions and saves them in external files.
- **V6PLOT.pro** plots the total effective area given the best d and best Γ and the number of repetitions from V6.pro output files.
- **MAT.pro** is a function to load the reflective indexes as functions of materials and energies from the IMD database.
- **BIO.pro** is a function to reshape and assign the correct refractive index to each layer of the coating to be used in a IMD simulation to calculate reflectivity.